
Università degli Studi di Ferrara

DOCTORAL COURSE IN PHYSICS

CYCLE XXXVII

COORDINATOR Prof. Paolo Lenisa

# Searching for the Anomalous Internal Pair Creation in $^{8}$Be

Scientific Disciplinary Sector (SDS) FIS/04

**Candidate**

Benito Góngora Servín

**Supervisors**

Prof. Diego Bettoni

Dr. Tommaso Marchi

Dr. Jose Javier Valiente Dobón

Years
2021/2024

*A todos los que han dado su vida*
*para darme el derecho a estudiar, gracias...*

**Abstract**

At the Laboratori Nazionali di Legnaro (LNL-INFN, Italy), a new $e^+e^-$ pair spectrometer has been designed and constructed. The project aims to study the Internal Pair Creation (IPC) process in $^8$Be since anomalies in the isovector ($1^+_1 \rightarrow 0^+_1$) and isoscalar ($1^+_2 \rightarrow 0^+_1$) magnetic dipole transitions have been reported for the angular correlation distribution. The present thesis describes the design, construction, and characterization of the new $e^+e^-$ pair spectrometer and the first series of experiments carried out at the AN2000 accelerator. The characterization of the prototype detectors of the spectrometer was performed using cosmic muons, $^{241}$Am, and $^{90}$S/$^{90}$Y radiation sources, where the performances for the energy and the interaction position measurement were tested. The $e^+e^-$ pair spectrometer can measure lepton energies from 1 to ~20 MeV and has an angular resolution of about 2.5° at a 12.5 cm target-detector distance.

The experimental campaign focused on studying the $^7$Li($p$,$e^+e^-$)$^8$Be nuclear reaction at the resonance energies of 441 keV and 1.03 MeV. LiF targets between 34 and 935 $\mu$g/cm$^2$ thickness with C/Cu backing from 10-60 $\mu$g/cm$^2$ were irradiated with proton beams with intensities of up to 800 nA. Given the presence of $^{19}$F in the target, the $^{19}$F($p$,$\alpha e^+e^-$)$^{16}$O nuclear reaction also occurs and populates the $0^+_2$ in $^{16}$O that decays to the ground state via IPC. This transition has been used as a reference to verify the quality of the data collected and the analysis process.

The experimental campaign was divided into three stages, involving different setup configurations: the first one was the in-beam commissioning of the detector array using a small-scale setup, while the second and third ones were dedicated to the measurement of $e^+e^-$ pairs emitted in the decay of $^{16}$O$^*$ and $^8$Be$^*$ using a larger amount of detectors covering different angular regions. The $1^+_1 \rightarrow 0^+_1$ and $1^+_2 \rightarrow 0^+_1$ transitions in $^8$Be and the $0^+_2 \rightarrow 0^+_1$ transition in $^{16}$O were clearly observed and separated, showing the detection capabilities of the spectrometer for such electromagnetic transitions. Eventually, the measured angular correlations for $^{16}$O were corrected by the efficiency of the detector array. In this test case, the model of Rose is consistent with the experiential results, with average discrepancies of less than 6%.

# Contents

# List of Figures

# List of Tables

# Introduction

In 1996, a series of anomalies in the angular correlation distribution of the Internal Pair Creation (IPC) process for the isovector magnetic dipole transition ($1^+_1 \rightarrow 0^+_1$) in $^8$Be were reported by F. W. N. de Boer [1]. These experimental results differed from the theoretical model of Rose [2, 3]. Twenty years later, at the Atomki Laboratories, A. Krasznahorkay and collaborators reported similar results for the specific case of the isoscalar magnetic dipole transition ($1^+_2 \rightarrow 0^+_1$) in $^8$Be. The theoretical explanation given by the group involves the creation and subsequent decay of a neutral boson named $X17$. This publication triggered worldwide efforts to reinvestigate this phenomenon. New experimental setups are under construction, and existing data are being analyzed to find indications of the claimed signal. For example, the MEG II collaboration recently announced the first results on this subject (see Chapter 1).

At the Laboratori Nazionali di Legnaro (LNL), a new $e^+e^-$ spectrometer was designed and constructed. Moreover, the first experimental campaign was performed in 2023 and 2024. The main advantages of this apparatus lie in the fact that it is vacuum compatible, has a high angular resolution, and a good $\gamma$-ray vs lepton suppression factor (~4 orders of magnitude).

This work describes the construction, characterization, and use of the new setup, as well as the first results from in-beam experiments. The thesis is divided into five chapters:

- **Chapter 1.** *Internal Pair Creation Process in $^8$Be.* Introduces the theoretical framework for the IPC process, focusing on the model of Rose. Furthermore, a historical review of the most important experiments performed in the study of the IPC in $^8$Be is presented.
- **Chapter 2.** *Design of the $e^+e^-$ pair spectrometer.* Contains the design and a detailed description of the Geant4 simulation of $e^+e^-$ pair spectrometer.
- **Chapter 3.** *Characterization of the $e^+e^-$ pair spectrometer.* Describes the first experiments devoted to characterize the $e^+e^-$ pair spectrometer.

- **Chapter 4.** *Experimental Campaign.* Describes the three experiments performed with different configurations. The in-beam capabilities of the $e^+e^-$ spectrometers are evaluated.
- **Chapter 5.** *Data Analysis and Results.* Describes the analysis method used to reconstruct the transition energy of the nuclei studied and the method to determine the angular distribution for the electric monopole transition in $^{16}$O.

# 1

# Internal Pair Creation Process in $^{8}$Be

*The present Chapter synthesizes the most relevant historical events in the study of the Internal Pair Creation (IPC) process in $^{8}$Be, starting from a description of the process and the theoretical model of Rose to the experiments carried out from 1953 to 2024. The arrays used to measure the angular distributions of the correlation angle of the $e^{+}e^{-}$ pair are discussed. The Chapter concludes with the motivation for new experiments to further study IPC in $^{8}$Be.*

## 1.1 Electromagnetic Transitions

In nature, physical systems look for configurations with the lowest energies. The atomic nucleus is not an exception, and several mechanisms have been discovered to reach this configuration: alpha decay, spontaneous fission, beta decay, $\gamma$-ray emission, Internal Conversion (IC), and Internal Pair Creation (IPC). The last three phenomena involve energy emission from a nucleus in an excited state ($^{A}X^{*i}$, $^{A}X$ nucleus in the $i$-est excited state) and leaving it in a lower energy state ($^{A}X^{*j}$, $^{A}X$ nucleus in the $j$-est excited state). These phenomena are called *electromagnetic transitions* since they are ruled by electromagnetic interaction.

In the $\gamma$-ray emission (see Figure 1.1 a)), the nucleus in an excited state emits a photon (called $\gamma$-ray) with energy of $E_\gamma$ equal to the difference energy of the $i$-est $E_i$ and the $j$-est $E_j$ states:

$$E_\gamma = E_i - E_j \tag{1.1}$$

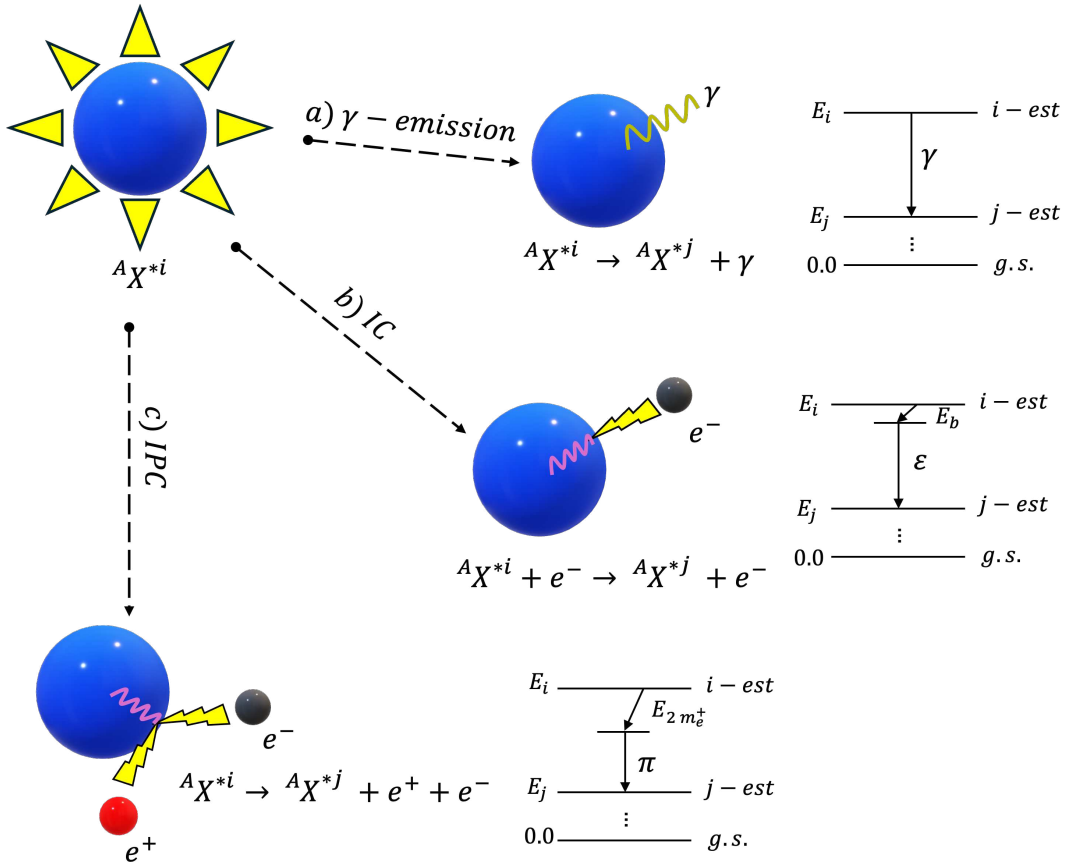


Figure 1.1: Types of electromagnetic transitions in a nucleus $^{A}X$: a) $\gamma$-emission ($\gamma$), b) Internal Conversion (IC, $\varepsilon$), and c) Internal Pair Creation (IPC, $\pi$). The purple waves indicate virtual photons.

In the Internal Conversion (see Figure 1.1 b)), an $e^-$ from an atomic orbital is ejected with an energy of $E_i$-$E_j$ minus the binding energy $E_b$ of the $e^-$ to the atom:

$$E_{IC} = E_\gamma - E_b \tag{1.2}$$

In the Internal Pair Creation (see Figure 1.1 c), a $e^+$ and an $e^-$ are created from the electromagnetic field of the nucleus and emitted. The energy is shared between them, and every lepton of the pair has a mass equivalent to the one of the electron ($m_{e^-}$). Thus, the threshold energy for this process is $2m_{e^+}$. The sum of the energy of the $e^+e^-$ pair is equal to the difference energy of the transition $i$-est and $j$-est minus the energy spent on the pair creation:

$$E_{e^+} + E_{e^-} = E_\gamma - 2m_{e-} \tag{1.3}$$

where $E_{e^+}$ is the energy of the $e^+$ and $E_{e^-}$ is the energy of the $e^-$.

The processes discussed above to deexcite a nucleus compete with each other. Two coefficients are defined to quantify this competition: the Internal Conversion Coefficient (ICC)

$$\Gamma_{ICC} = \frac{P_{IC}}{P_\gamma} \tag{1.4}$$

and the Internal Pair Creation Coefficient (IPCC)

$$\Gamma_{IPCC} = \frac{P_{IPC}}{P_\gamma} \tag{1.5}$$

where $P_{IPC}$ is the probability of IPC process and $P_{IC}$ is the probability of the IC.

Among the mechanisms shown in Figure 1.1, the most common one is the $\gamma$-ray emission, which is more probable by ~3-5 orders of magnitude than the other two. This value can drastically decrease under certain circumstances, in case of a $0_2^+ \rightarrow 0_1^+$ transition. In this transition, the $\gamma$-ray emission is forbidden, and the IC and IPC are the mechanisms the nucleus chooses for de-excitation. Between the IPC and IC, the IPC rate is the largest, whereas the IC is the smallest. The $E_\gamma$ also affects these probabilities. While the IPCC increases with the energy, the ICC decreases.

Regarding the dependency on the atomic number of the nucleus $Z$, the ICC increases with it, and the IPCC is almost independent (decreases slightly with $Z$). Thus, the region of low $Z$ and large $k$ (ratio of $E_\gamma$ and $m_e c^2$) makes the performance of experiments to study the IPC process more feasible. As a reference, for $Z = 40$ and $k = 5.0$ (~ 2.5 MeV), the IPC and IC are roughly equally probable [2].

## 1.2 Theoretical Description of the IPC

In 1949, Rose provided the foundation for an *IPC model* [2] where the most important feature is the evaluation of the role of the multipolarity of the electromagnetic transition. The model is based on the Born approximation, implying that the predictions are more accurate if integrated over the whole energy spectrum. The total energy (including the mass of the $e^+e^-$ pair) and momentum are represented by $W_\pm$ and $\boldsymbol{p}_\pm$ (where + is related to $e^+$ and − to $e^-$), respectively.

As a note, the equations are expressed in natural units ($\hbar$=$c$=$m_{e^-}$= 1). The first step is the expression of the radiation field in terms of a vectorial $\boldsymbol{A}$ and scalar $V$ vectors. For the electric $2^l$ multipole field, the potentials are of the following form:

$$\boldsymbol{A_{lm}} = (2/\pi l(l+1))^{1/2}\chi_{l-1}(kr)(r\nabla + l\boldsymbol{r}/r)\boldsymbol{Y}_l^m \tag{1.6}$$

$$V = i(2l/\pi(l+1))^{1/2}\chi_l(kr)\boldsymbol{Y}_l^m \tag{1.7}$$

where $\boldsymbol{r}$ the position vector, $\boldsymbol{Y}_l^m$ the normalized sphrical harmonic, and $\chi_l$ the Hankel function of the first kind.

$$\chi_l(x) = (\pi/2x)^{1/2}\boldsymbol{H}^{(1)}_{l+1/2}(x) \tag{1.8}$$

On the other hand, for the magnetic $2^l$ multipole field:

$$\boldsymbol{A_{lm}} = -(2/\pi l(l+1))^{1/2}\chi_{l-1}(kr)\times\nabla\boldsymbol{Y}_l^m \tag{1.9}$$

$$V = 0 \tag{1.10}$$

where the normalization factor is

$$N_q = \frac{1}{\pi^2 k} \tag{1.11}$$

With those elements, the calculation of the ratio of the number of $e^+e^-$ pairs per second in the solid angles $d\Omega_+$ and $d\Omega_-$ and the energy of the $e^+$ in the range $W_+$ and $W_+ + dW_+$ to the number of quanta per second is

$$\begin{aligned} d\gamma_l(W_+;\theta_+,\varphi_+;\theta_-,\varphi_-) &= \tfrac{\alpha k}{32\pi^3}p_+p_-W_+W_- \\ &\quad\times\textstyle\sum_{s_+s_-}|\langle\boldsymbol{\psi_-}|V+\boldsymbol{\alpha}\cdot\boldsymbol{A}|\boldsymbol{\psi_+}\rangle|^2 d\Omega_+d\Omega_-dW_+ \end{aligned} \tag{1.12}$$

where $\theta_\pm$ are the polar angles, $\varphi_\pm$ are the azimuthal angles, $\alpha$ is the fine structure constant, $\boldsymbol{\alpha}$ the Dirac matrix vector. The wave functions are considered as plane waves:

$$\boldsymbol{\psi}_\pm = u_\pm(\boldsymbol{p}_\pm)exp(\pm i\boldsymbol{p}_\pm\cdot\boldsymbol{r}) \tag{1.13}$$

where $u_{\pm}(\boldsymbol{p}_{\pm})$ are the amplitudes of the waves. The summation is performed over the spins of the $e^+$ and $e^-$, and adding an operator $G_{\pm}$

$$G_{\pm}u_{\pm} = \begin{cases} u_{\pm} & W_{\pm} > 0 \\ 0 & \text{otherwise} \end{cases} \tag{1.14}$$

Applying the sum over the four spin states:

$$G_{\pm} = (-\boldsymbol{\alpha} \cdot \boldsymbol{p}_{\pm} \mp \beta + W_{\pm})/2W_{\pm} \tag{1.15}$$

where $\beta$ is the fourth Dirac matrix. Performing the sum:

$$\sum_{S_+S_-} |\langle \boldsymbol{\psi_-}|V + \boldsymbol{\alpha} \cdot \boldsymbol{A}|\boldsymbol{\psi_+}\rangle|^2 = Spur(\Lambda G_+ \Lambda^+ G_-) \tag{1.16}$$

with

$$\Lambda = \boldsymbol{\alpha} \cdot \int e^{i\boldsymbol{q}\cdot\boldsymbol{r}} \boldsymbol{A} d\tau + \int e^{i\boldsymbol{q}\cdot\boldsymbol{r}} V d\tau \tag{1.17}$$

where $\boldsymbol{q} = \boldsymbol{p_+} + \boldsymbol{p_-}$, and $d\tau$ is the volument element. To carry out the integral of the Equation 1.12, a geometrical consideration makes the calculation easier. This integral can be simplified by using the angle ($\delta$) between the plane formed by the vector $\boldsymbol{q}$ and the unitary vector of the quantization $\boldsymbol{z}$, and the plane formed by the $\boldsymbol{p_+}$ and $\boldsymbol{q}$ plane. Also, the sine and cosine identities are useful:

$$sin\theta_+ e^{i\varphi_+} = e^{\pm i\phi}(cos\omega_+ sin\theta - sin\omega_+ cos\theta cos\delta \mp i sin\omega_+ sin\delta)$$

$$cos\theta = cos\omega_+ cos\theta + sin\omega_+ sin\delta$$

with $\omega_+$ the $\measuredangle \boldsymbol{p_+ q}$ (angle between the $\boldsymbol{p_+}$ and $\boldsymbol{q}$ vector). The no-indexed angles $\theta$ and $\phi$ correspond to the polar and azimuthal angles of the $\boldsymbol{q}$ vector, respectively. Then, two integrals are performed, the first over the $\delta$ angle and the second over the direction of the $\boldsymbol{q}$ ($d\Omega_+ d\Omega_- = sin\theta d\theta d\phi d\delta sin\Theta d\Theta$). In such a way, the number of $e^+e^-$ pairs is calculated per unit energy interval, per $|dcos\Theta|$, per quantum energy, and $W_+\pm$ being fixed:

$$\gamma_l(\Theta) = \int (d\gamma_l / d\Omega_+ \Omega_- dW_+)\, sin\theta d\theta d\phi d\delta \tag{1.18}$$

For electric multipoles, the angular distribution is described by the integra-

tion of the Equation 1.18 and the potentials of the Equations 1.6 and 1.7:

$$\gamma_l(\Theta) = (2\alpha/\pi(l+1))\left(p_+p_-/q\right)\frac{(q/k)^{2l-1}}{(k^2-q^2)^2} \times \{(2l+1)(W_+W_- + 1 - \frac{1}{3})p_+p_-cos\Theta) + l[(q^2/k^2) - 2](p_- + p_+cos\Theta) \times (p_+ + p_-cos\Theta) - cos\Theta]\} \quad (1.19)$$

and for magnetic multipoles (using the potentials of the Equations 1.9 and 1.10):

$$\gamma_l(\Theta) = (2\alpha/\pi)\left(p_+p_-/q\right)\frac{(q/k)^{2l+1}}{(k^2-q^2)^2}\{1 + W_+W_- - \frac{p_+p_-}{q^2}\left(p_- + p_+cos\Theta\right)\left(p_+ + p_-cos\Theta\right))\} \quad (1.20)$$

Figure 1.2 shows the $e^+e^-$ angular distributions for $E0$, $E1$, $E2$, $M1$, and $M2$ transition at 17 MeV electromagnetic transitions calculated by the Equations 1.19 and 1.20 have the maximum at forward angles ($\Theta \approx 0°$).

The total IPC per quantum can be calculated by performing the integral over the correlation angle $\Theta$ of Equations 1.19 and 1.20.

$$\Gamma(W_+) = \int_0^\pi \gamma_l(\Theta)sin(\Theta)d\Theta \quad (1.21)$$

Obtaining the expressions for electric multipoles

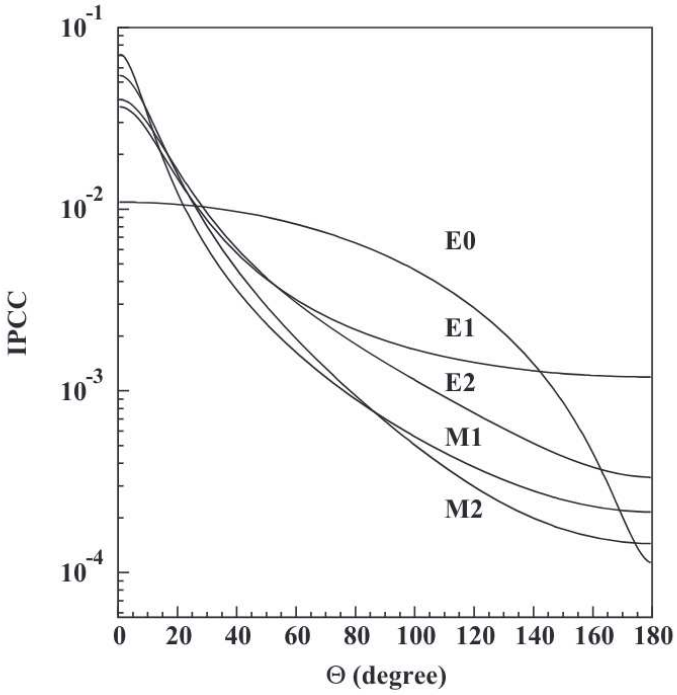


Figure 1.2: Angular distributions for $E0$, $E1$, $E2$, $M1$, and $M2$ transition at 17 MeV electromagnetic transitions calculated by the Equations 1.20 and 1.19 [4].

$$\begin{aligned}\Gamma_l(W_+) = \left(\alpha/\pi(l+1)k^3\right)\,&(l/2)k^2 J_{l+1} \\ &+ [2lW_+W_- - \frac{1}{4}(7l+1)k^2]J_l \\ &+ l[\frac{3}{2}(W_+^2 + W_-^2 + 1] + W_+W-]J_{l-1} \\ &- \frac{1}{4}(l-1)(W_+ - W_-)^2 J_{l-2}\}\end{aligned} \tag{1.22}$$

and for magnetic multipoles

$$\Gamma_l(W_+) = \alpha/\pi k^3\{1 + W_+W_-\}J_l \\ -(k^2/4)(J_{l+1} - x_1x_2J_{l-1}\}) \tag{1.23}$$

where the $J_l$ is defined as

$$J_l = \int_{x_1}^{x_2} x^l(1-x)^{-2}dx \tag{1.24}$$

and $x_1$ and $x_2$ as

$$x_1 = (p_+ - p_-)^2/k^2,\ x_2 = (p_+ + p_-)^2/k^2 \tag{1.25}$$

Finally, the total number of $e^+e^-$ pairs per quantum is the value of the integral of Equations 1.22 and 1.23 over the energy:

$$\Gamma_l = \int_l^{k-1} dW_+\Gamma_l(W_+) \tag{1.26}$$

The values of the integral 1.26 as a function of the energy $k$ are calculated for electric (see Figure 1.3 a)) and magnetic (see Figure 1.3 b)) transitions and for different multiples and decreases with the multipole order. As expected, the number of $e^+e^-$ pairs created increases with the energy $k$. In the next chapter, the implications of the model of Rose will be discussed in terms of the angular correlation distribution of the $e^+e^-$ pairs.

## 1.3 Role of the Angular Distribution in the Model of Rose

One of the successes of the model of Rose [2, 3] is the description of the angular distribution of the correlation angle between the $e^+e^-$ pair for different multipole transition since it is a more sensible factor to the type and multiple

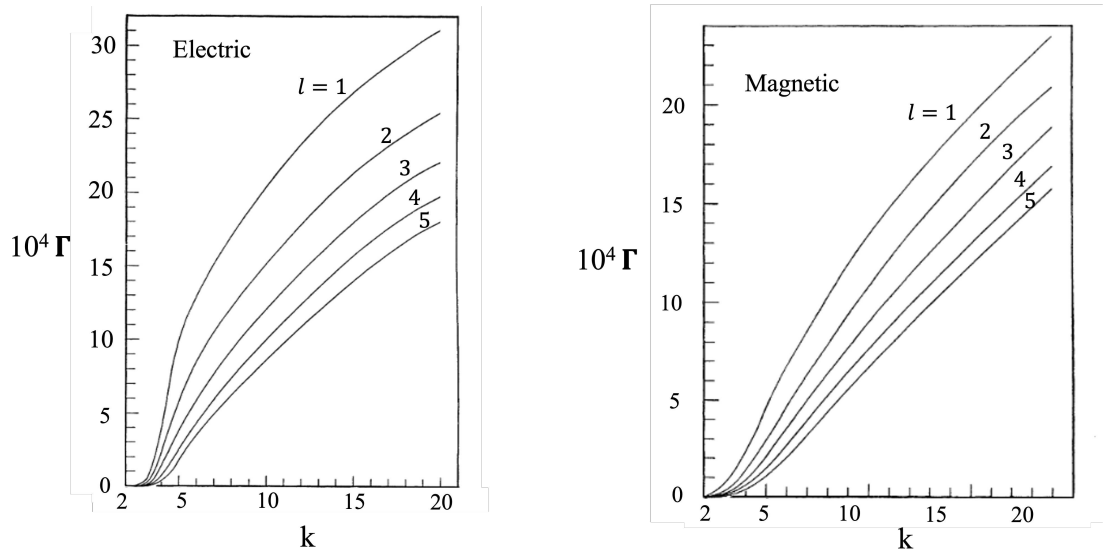


(a) (b)

Figure 1.3: Total number of $e^+e^-$ pairs per quantum for a) electric and b) magnetic multipoles. The multipole $l$ is shown on top of the corresponding curve.

order of the electromagnetic transition than the total IPCC, as it is explained below. Before 1953, the experimentalists focused on measuring the total IPC coefficient. Still, this value starts losing sensibility at large values of energy $k$, where the IPC probability is higher than the IC (the IC decreases approximately as $Z^3$ or $k^{-n}$, where n ~ 2-3). The IPC probability increases with the energy $k$, and for $k > 20$, these values are of the order of $10^{-3}$ (independently of the multipole). In this region, the value of the ratio of $\Gamma$ between two consecutive multipoles gets close to the unity, which means that it is poorly sensible to the multipolarity of the transition. This behavior is more evident by looking at the curves of Figure 1.3 a) and b) since the slope for the different values of $l$ tends to be equal for high energy values. Rose proposed an alternative approach to this issue. Instead of measuring the total IPCC (defined in Equation 1.26), the measurement of the amount of $e^+e^-$ pairs emitted at 0° and at 90° (chosen because the evaluation of Equation 1.19 or 1.20 is easier since $cos\Theta = 0$) is sensible enough. The ratio between these values can be calculated by integrating Equation 1.19 or 1.20:

$$R = \int_1^{k-1} dW_+\gamma_l(0) / \int_1^{k-1} dW_+\gamma_l(\pi/2) \tag{1.27}$$

Figure 1.4 a) shows the value of the ratio for electric transitions and 1.4 b) for magnetic transitions. Unlike the case of the total IPCC, the curves tend to separate with the energy $k$ for all the multipolarities, allowing better discrimination among them, with differences higher than 20%. In other words, the angular emission of the $e^+e^-$ pair has a higher dependency on the multipolarity than the total amount of $e^+e^-$ pairs emitted. Thus, the model of Rose changed the approach to studying electromagnetic transitions in light nuclei through this process. The angular distribution of the relative emission angle of the pair became the most helpful tool, and some laboratories around the world started the development of dedicated detector arrays.

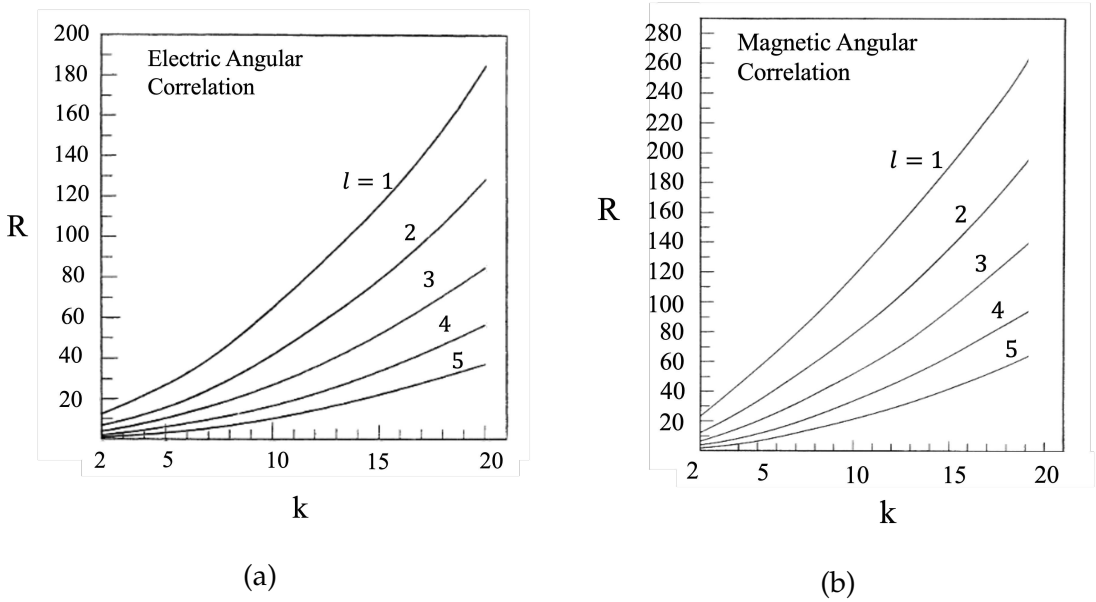


(a) (b)

Figure 1.4: Ratio (see Equation 1.27) of the number of $e^+e^-$ pairs per quantum emitted at a relative angle of 0° over the ones emitted at 90° for a) electric and b) magnetic multipoles. The multipole $l$ is shown on top of the corresponding curve.

## 1.4 IPC IN $^{16}$O AND $^{8}Be$.

This paragraph describes the historical research in the study of the IPC in $^{16}$O and $^{8}$Be, using different proton-induced reactions. The low-lying structure of those nuclei is reported in Figures 1.5 and 1.6, respectively. In the case of $^{16}$O, for the $0_2^+ \rightarrow 0_1^+$ transition, the $\gamma$-ray emission is forbidden, resulting in a high probability of IPC emission. On the other hand, high energy transitions in $^{8}$Be

can emit both $e^+e^-$ pairs or $\gamma$-rays. Over the years, the observation of anomalies between the experimental $e^+e^-$ angular distribution and the prediction of the model of Rose has been reported [1]. Recently, these results have also been interpreted as a hint of the existence of a new neutral boson named X17 [5].

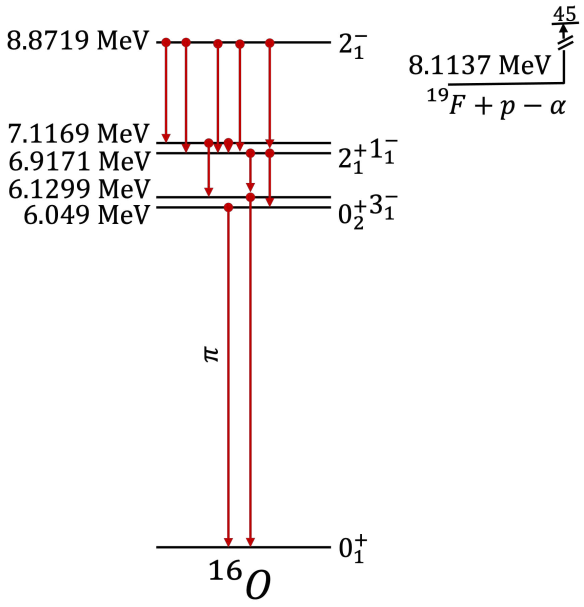


Figure 1.5: Low-lying states of $^{16}$O.

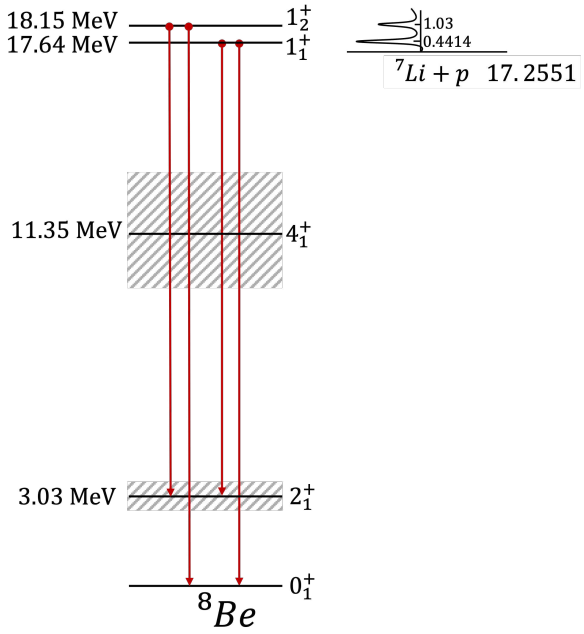


Figure 1.6: Low-lying states of $^8$Be.

The main steps of this research are summarized in Figure 1.7 and will now be discussed in detail.

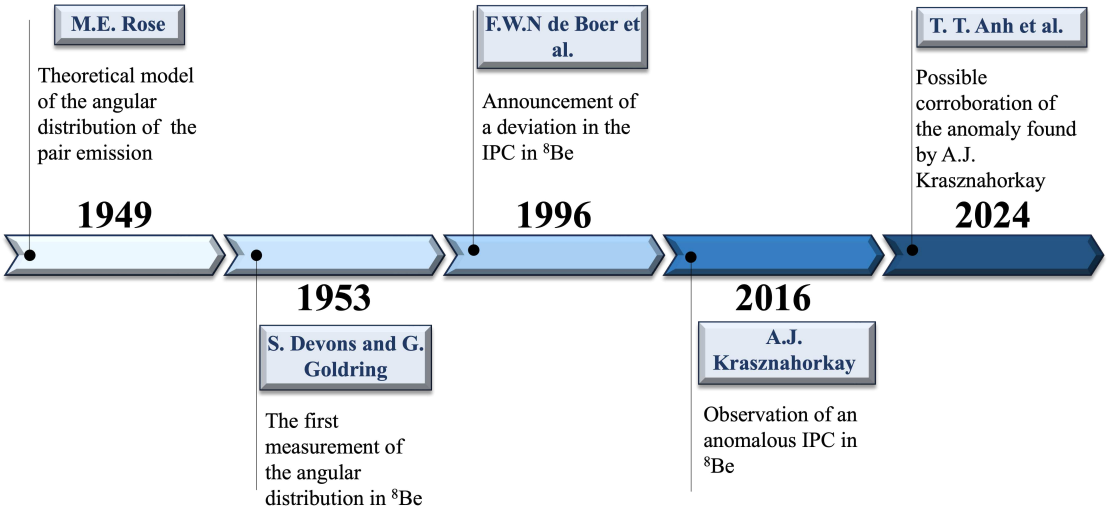


Figure 1.7: Timeline of the most relevant events related to the study of the Internal Pair Creation in $^{8}$Be.

### 1.4.1 1953: S. Devons and G. Goldring

In 1953, the IPC from the first $0^+_2$ state in $^{16}$O had already been studied, but only the absolute internal pair creation coefficient had been estimated. S. Devons and G. Goldring [6] proposed an experiment to determine the distribution of the relative angle of the emitted pairs. The population of the state was via the nuclear reaction $^{19}$F(p,$\alpha$)$^{16}$O (see Table 1.1). In the excitation energy range of 0.5-1.5 MeV, the deexcitation of other states like the $3^-$ or the first $2^+$ were responsible for $\gamma$ ray emission. A scan was needed to optimize the proton beam energy so that the pair emission was maximum from the $0^+_2$ state and the $\gamma$ ray emission was as low as possible. A $CaF_2$ target was deposited on a 0.15 mg/cm$^2$ aluminum foil by vacuum evaporation. The target was placed inside an aluminum cylinder with a 0.1 mm wall thickness to avoid stopping the $e^+e^-$ pairs. The detector array consisted of two Geiger detectors, "a" and "b," with a 0.1 mm thickness wall that could perform measurements in coincidence mode (see Figure 1.8). A third Geiger counter named "c" was used as an anticoincidence detector to avoid considering electrons scattered in "a" and going to "b" or vice-versa. A fourth Geiger detector was placed far away to monitor the $\gamma$-rays emission (on top in Figure 1.8). The apparatus was used to estimate the $\gamma$ ray and $e^+e^-$ pair yield at

Table 1.1: Main electromagnetic transitions emitting $e^+e^-$ pairs via the IPC process by the irradiation of a target containing $^7$Li or/and $^{19}$F by a proton beam at 441 keV energy.

| **Nucleus** | **Transition** | **Type** | **Energy [MeV]** |
|---|---|---|---|
| $^{16}$O | $0_2^+ \rightarrow 0_1^+$ | $E0$ | 6.0482 |
| $^8$Be | $1_1^+ \rightarrow 2_1^+$ | $M1$ | 14.586 |
| $^8$Be | $1_1^+ \rightarrow 0_1^+$ | $M1$ | 17.619 |

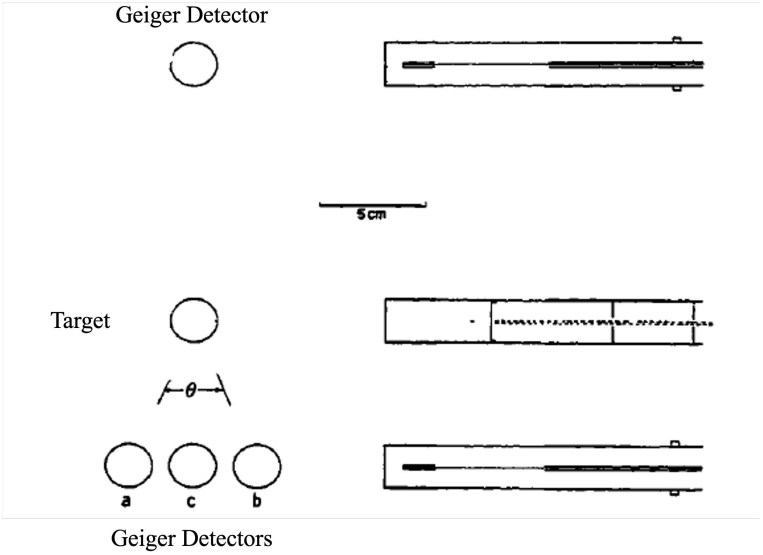


Figure 1.8: Geiger counters array for measuring the excitation function for pair production [6].

different beam energies. As Figure 1.9 shows, the energy region around 840 keV is where the maximum of the pair yield is combined with the minimum of the $\gamma$ ray yield. For this reason, this energy was chosen to measure the angular distribution.

### Angular Correlation Distribution of the $e^+e^-$ Relative Angle

All components were placed inside a vacuum chamber to minimize the scattering of the $e^+e^-$ pairs. Moreover, the setup was modified to build a simple telescope using two Geiger detectors, as Figure 1.10 shows: A) steel plate, S) slits (±1.5 mm aperture), T) target support which allows to tilt the target 45°, D) drum, c), C) pair of the electron detecting counters. One telescope was fixed, while the other was mounted on an arm that could be rotated from outside. In

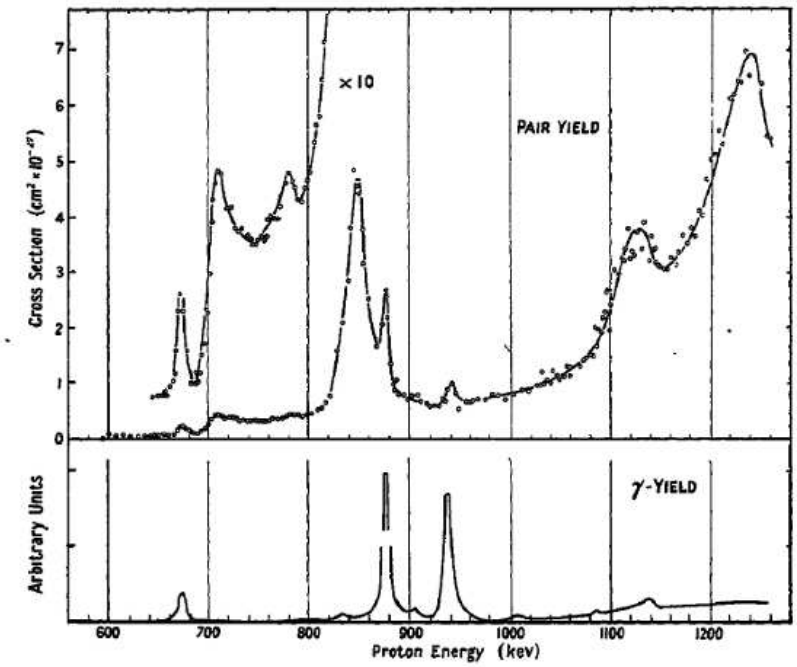


Figure 1.9: Excitation function of the pair emission and $\gamma$-yield. The low energy region of the pair yield is multiplied by 10 for better appreciation [6].

addition, a fifth Geiger counter G was mounted further away to monitor the $\gamma$-ray emission during the irradiation. To avoid the measurement of $e^+/e^-$ in this Geiger, a 1 cm lead thickness layer was used as a shielding. The current after the target was observed in the Faraday Cup F.

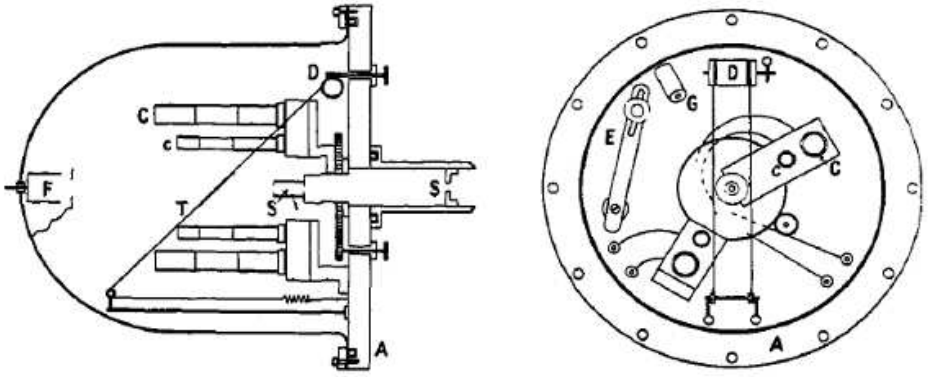


Figure 1.10: Setup for the lepton angular correlation. [6].

The telescope consisted of two counters (inner and outer) with diameters of 2.1 and 3.1 cm and effective lengths of 2 and 7.5 cm, respectively. An electron energy-dependent efficiency was applied and computed by studying the

behavior under the irradiation of an electron source. Two configurations were investigated; in the first one ("close position"), the inner counter was 7 cm away from the target, and the outer one was 10.5 cm. In the second one ("far position"), the distances were 10 cm and 15 cm, respectively. The events recorded were coincidental between the two telescopes in a time window of 1 $\mu$s. The random coincidences were estimated by applying a delay in one of the channels; in that way, the real coincidences were gone, and only the random ones were recorded. In addition, the random rate could be estimated by observing the behavior of the single counting rate as a function of the beam intensity.

The angular distribution was determined by the number of coincidences between the fixed and the moving telescopes (in the left Figure 1.10, the fixed telescope is at the bottom, and the moving one is at the top). Several angles were studied, avoiding small changes because they can add systematic errors in determining the angle. Figure 1.11 shows the angular distribution after some correction by geometry. Other effects were neglected due to the small contribution to the total distribution, like the scattering in target foil and support, cosmic radiation, background from target support, and "stray" electrons ($e^+$ or $e^-$ scattered in the chamber wall). A normalization factor of half of the sum of the counts registered in the fixed, and the moving counter was applied to the counts in coincidence (T).

The results showed a consistent form with the cosine correlation function: $A(1 + \alpha_{exp} cos\theta)$. The values of the fit calculated were:

1. Far out: $\alpha_{exp,F} = 0.980 \pm 0.009$.

2. Close in: $\alpha_{exp,F} = 0.948 \pm 0.012$.

The following section will show that these results can be compared directly with a theoretical model constructed from basic principles.

#### Comparison with Theory

Nowadays, the transition studied by Devons and Golding [6] is very well described. They discussed the results by assuming an even parity in the excited and ground state in $^{16}$O (unknown at that moment) and electromagnetic interaction between the positron and the electron. As a first-order approximation, the function of the zero-pole transition (a resonance in field theory) is of the form

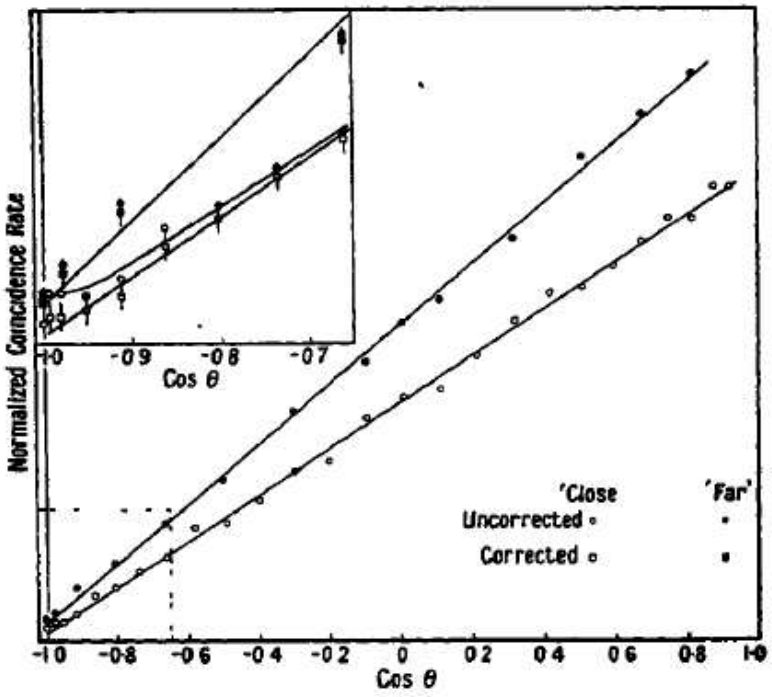


Figure 1.11: $e^+e^-$ pair angular correlation distribution from the $0_2^+ \rightarrow 0_1^+$ transition in $^{16}O$[6].

[7, 8]:

$$P(\theta)dW_+d\Omega = \frac{e^4\langle M\rangle^2}{9\pi}p_-p_+(W_+W_-1 + p_+p_-cos\theta)dW_+d\Omega \tag{1.28}$$

Where $p_\pm$ are the momenta, $W_\pm$ are the energies (in natural units) of the positron (+ subindex) and electron (− subindex). $\langle M\rangle$ is the nuclear matrix element. The angular distribution can be determined by integrating Equation 1.28 and considering the efficiency of detection by the detector array:

$$P'(\theta) = \int d\Omega_+d\Omega_-dW_+\eta(W_+)\eta(W_-)P(\theta) \tag{1.29}$$

Where $\eta(W_\pm)$ is the relative efficiency of the telescope counter as a function of the energy of the lepton. The authors mentioned in [6] that a numerical approximation of Equation 1.29 allows us to find an expression of the form:

$$P'(\theta) = A\{1 + (0.9937 - \delta)cos\theta\} \tag{1.30}$$

The value of $\delta$ depends on the geometry of the array. In the case of infinitesimally small detectors, $\delta$ equals zero. The theoretical angular distribution for

every configuration was calculated by applying this methodology:

$$\text{Far out: } P'_F(\theta) \propto 1 + (0.974 \pm 0.002)cos\theta \tag{1.31}$$

$$\text{Close in: } P'_C(\theta) \propto 1 + (0.955 \pm 0.003)cos\theta \tag{1.32}$$

The primary source of discrepancy and error is the determination of the sensitive volume of the counters. Both results are compatible with the experimental results, with around -0.002 ± 0.008 differences.

### Pair Emission from $^8Be$

The apparatus described above was used to measure the angular correlation of the IPC in $^8$Be [9]. The transition was studied via the nuclear reaction $^7$Li(p,$\gamma$)$^8$Be at 441 keV. The importance of this transition (see Figure 1.6) lies in the fact that the $\gamma$-transition energy is large (>12 $m_e c^2$), and the atomic number of the radiating nucleus is small (<8), which means a low IC probability. These characteristics make the $^8$Be an excellent candidate to use the model of Rose [2, 3].

The probability of pair emission per quantum with energies $\omega_+ k$, $\omega_- k$ ($\omega_+ + \omega_- = 1$, the energy $k$ is in $m_e$-$c^2$ units) as a function of the relative angle $\theta$ can be written in the form $\gamma_l^k = \gamma_l^k(\theta, \omega_+)\Omega_+\Omega_-$ (see Equations 1.19 and 1.20 for the expression) for radiating nucleus with a random population of states, where $l$ represents the multipole of the transition and $\Omega_\pm$ the solid angle coverage of the detection of the positron and the electron. As the next chapter will show, the Rose model [2, 3] predicts a sharp peak at small angles corresponding to the pairs emitted in the radiation zone of the transition field. In contrast, a large angle emission corresponds to the pairs created close to the nucleus. Moreover, most pairs are emitted at small angles at high energy transitions, and the total pair creation coefficient is not so sensitive to electromagnetic multipolarities. Fortunately, Rose demonstrated that the angular correlation distribution is sensitive to the multipolarity regardless of the energy:

$$g_l^k(\theta) = \int_{\omega_+=1-1/k}^{\omega_+=1/k} \gamma_l^k(\theta, \omega_+) d\omega_+ \tag{1.33}$$

Since the angular correlation functions $g_l^k$ of the electric $2^l$-pole and the mag-

netic $2^{l+1}$-pole are near, the convenient notation $\Lambda = l$ for electric $El$ transitions and $\Lambda = l + 1$ for $Ml$ transitions will be used.

### Experiment

In addition to the difficulties described in the monopole transition in $^{16}$O, some others arise in studying the $\gamma$-transitions in $^{8}$Be. The most relevant ones are the external pair creation in the target and target backing due to the interaction of the high-energy $\gamma$-rays. Since the backing and target were tin, the external production was neglected. Furthermore, the $\gamma$-rays induce stray electrons by interacting with the chamber walls, but they mainly affect the measurements of the correlation angle close to $\pi$. Regarding small angles, a low limit was set at $\pi/4$ to have an uncertainty lower than 2% for geometrical reasons.

LiH targets were irradiated by a proton beam at 440 keV. Due to the instability of the material in the air, the target was evaporated in the same chamber. Two configurations of telescopes were set: a) inner counter at 7 cm from the target and the outer at 10 cm, and b) inner counter at 7 cm from the target and the outer at 12.5 cm. The experimental angular distribution of the $e^+e^-$ correlation angle has been normalized as in the $^{16}$O case. Figure 1.12 shows the angular distribution obtained by Devons and Goldring (the dotted line represents the contribution of the stray electrons, visible near $\theta = \pi$).

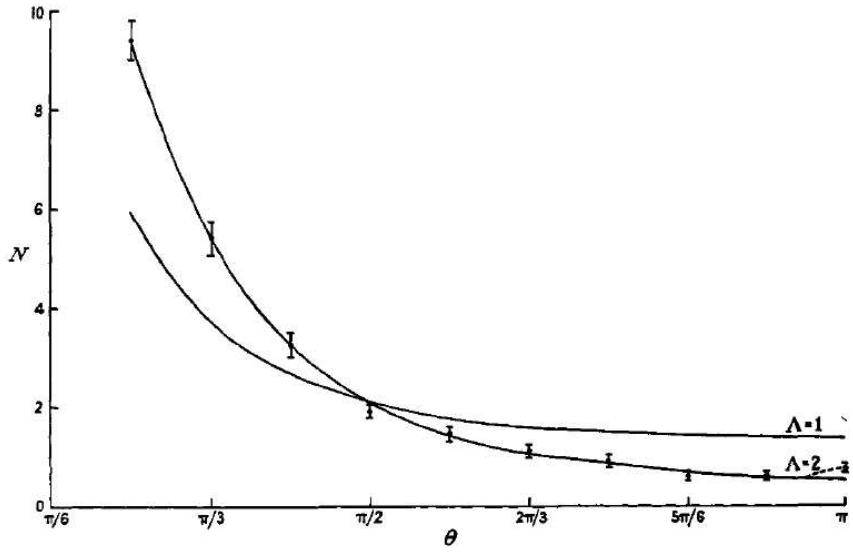


Figure 1.12: Angular correlation distribution of the $e^+e^-$ pairs from $^{7}$Li(p,$\gamma$)$^{8}$Be. The solid lines represent the theoretical calculations for $\Lambda = 1$ and $\Lambda = 2$, for Ml transitions [9].

Two $\gamma$ rays are emitted from the populated state with energies of $k = 28.2$ (14.4 MeV) and $k = 34.5$ (17.63 MeV). At that moment, the parity of the state was not determined. In 1950, Hornyak [10] proposed that the anomalous scattering of the protons impinging $^7$Li is due to p-wave scattering. Since the ground state of $^7$Li has odd parity, the resonance level in $^8$Be must be a state with even parity. Devons and Hine [11] suggested that a near-isotropy of the two $\gamma$ radiation components is related to s-protons. Furthermore, Devons and Lindsey [12, 13] claimed that a p-wave excitation could mean isotropic radiation if spins are mixed. This behavior can be caused by either a pure $p_{1/2}$ proton wave or a $S_1$ state in $^8$Be. In either case, the assumption of a total angular momentum $J = 1$ is compatible. According to Hornyak [10], the de-excitation states are the ground and the first excited states with spins and parities of $0^+$ and $2^+$, respectively. An odd parity ($1^-$, $\Lambda = 1$) implies transitions of the type $E1$, and an even parity ($1^+$, $\Lambda = 2$) implies $M1$ and $M1 + E2$ transitions. Those transitions can be expressed in a similar form. Considering only the most intense one ($k = 34.5$), we can calculate the theoretical distributions numerically:

$$\int_{2.5}^{34.5} \gamma_l^{34.5}(\theta, \omega_+) d\omega_+ \tag{1.34}$$

The cutoff energy is due to the loss of sensitivity of the detector from 0.75 MeV. The theoretical curve can be seen in Figure 1.12 (solid line). This result indicates that the transition is of the type $\Lambda = 2$ and corroborates that the $^7$Li + p is produced by p-wave protons and establishes the electromagnetic transition as a $M1$.

### 1.4.2 1996: F. W. N. de Boer et al.

Around 20 years after the former studies by Devons and Golding [6, 9], some experimental discrepancies in the measurements of X-rays in muonic atoms raised the possibility of the existence of scalar mesons $\phi$ proposed by Weinberg [14]. Expanding the theoretical framework, Resnick and collaborators [15] described the properties of a neutral boson and suggested the lepton pair emission (see Figure 1.13) as a process to find evidence of the existence of the boson claimed. In this environment, de Boer started performing experiments [1] to study electromagnetic transitions for short-lived neutral bosons in the mass range of 5-15 MeV/c$^2$ by measuring the angular distribution of the relative an-

gle in the IPC. The authors expected to observe a structure atop the theoretical angular distribution induced by a hypothetical $\phi$ boson decay.

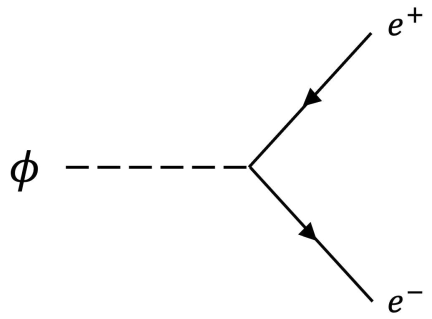


Figure 1.13: Feynamnn diagram of the isoscalar meson $\phi$ decaying into a positron and an electron.

The electromagnetic transitions chosen as an object of study were the $E1$ in $^{12}$C from the 17.2 MeV state ($J^\pi = 1^-, T = 1$) and the $M1$ in $^{8}$Be from the 17.6 MeV state ($J^\pi = 1^+, T = 1$), since they have similar transition energies to the ground state and similar target conditions. The first one has been achieved via the nuclear reaction $^{11}$B(p,$\gamma$)$^{12}$C at 1.6 MeV beam energy. This reaction populated two states in $^{12}$C, including the state of interest. The state at 17.2 MeV ($\Gamma$ = 1.15 MeV) feeds the first excited state and ground states by isovector transitions $E1$. The other populated state is the level at 16.6 MeV ($\Gamma$ = 300 keV), which feeds the first excited state ($\sigma$ = 48 $\mu$b) by the same type of transition as in the previous case. The cross-section of the population of the 17.2 MeV state via the chosen reaction is 27 $\mu$b, and for the one at 16.6 MeV, it is 3 $\mu$b.

On the other hand, the population of the state of interest in $^{8}$Be has been performed via the proton-induced reaction $^{7}$Li(p,$\gamma$)$^{8}$Be at 441 keV beam energy. At this time, the level was well-known. It has a width $\Gamma$ = 11 keV, and the isovector transition $M1$ feeds the first excited state ($\Gamma$ = 1.5 MeV). The cross-section of the population of this state is 4.5 mb.

#### Setup Description

The setup consisted of six $\Delta$E-E telescopes in such configuration that allowed to measure in coincidence 15 different combinations with angles from 20° to 130° (see Figure 1.14). As a $\Delta$E layer, the telescope had a plastic scintillator plate and, as a $E$ layer, a scintillator block. In addition, two larger telescopes were placed around $\theta$ = 42° and $\theta$ = 65°. This modification increased the combinations by

13 more angles. Metallic $^{11}$B targets from 100 $\mu$m/cm$^2$ to 600 $\mu$m/cm$^2$ thickness were irradiated with a proton beam of 10 $\mu$A. In the case of $^{8}$Be, only tin targets of 100 $\mu$m/cm$^2$ were irradiated.

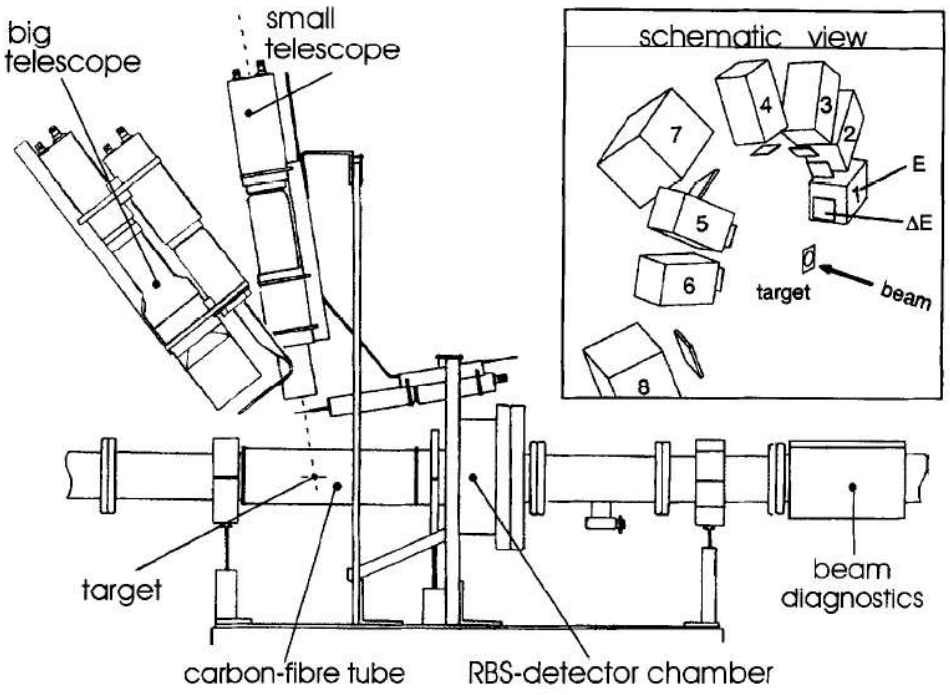


Figure 1.14: Scintillator detector array used by de Boer in the measurement of IPC distributions in $^{12}$C and $^{8}$Be [1].

The transition of interest has been selected by reconstructing the energy transition, summing up energy deposited in two telescopes in coincidence. A test in a LINAC showed an energy resolution of 10% at 8 MeV and 16% at 14 MeV. Figure 1.15 a) shows the experimental energy spectrum for the study of $^{11}$B, and the 1.15 b) is a Geant Monte Carlo simulation. The highest energy peak corresponds to the transition to the ground state, the intermediate one to the first excited state, and the low energy one to the $E0$ transition in $^{16}$O due to contamination of the target by $^{19}$F, which produces $^{16}$O via a (p,$\alpha$) reaction. Finally, Figure 1.15 c) shows the transition to the ground state in $^{8}$Be at high energy and the transition to the first excited state. The angular distribution of the IPC process was calculated by considering the angles of the central position of the two detectors in coincidence. Geometrical corrections were applied to the final distributions. Figures 1.16 a) and 1.16 c) show the distribution in $^{12}$C and $^{8}$Be, respectively. The dashed line represents the IPC distribution without

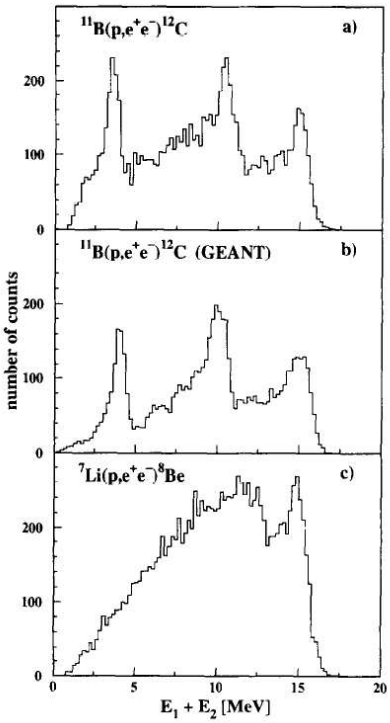


Figure 1.15: Sum-energy spectra of the pairs from the reactions $^{11}$B(p,$e^+e^-$)$^{12}$C, a) experimental, b) Geant simulation, c) $^{7}$Li(p,$e^+e^-$)$^{8}$Be[1].

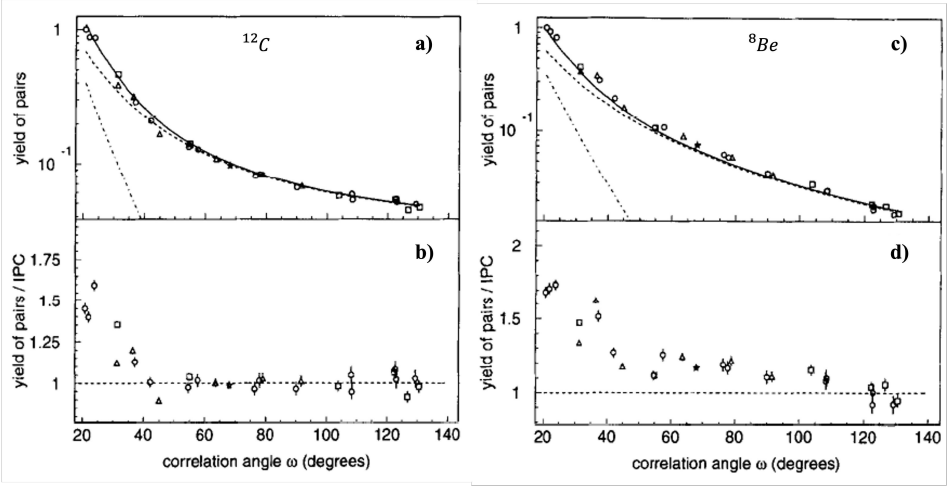


Figure 1.16: (a) Measured angular correlation for the pairs from the reaction $^{11}$B(p,$e^+e^-$)$^{12}$C, using geometrical detector efficiencies and normalized to the theoretical El-IPC correlations [2, 3] (dashed line) in the angular range over this range. The solid line includes effects from EPC and multiple scattering calculated in a Monte Carlo simulation (dot-dashed lines). (b) The ratio of the experimental data and the IPC prediction. (c) Same as (a) but related to the nuclear reaction $^{7}$Li(p,$e^+e^-$)$^{8}$Be. (b) Same as (d) for the $^{7}$Li($p$,$e^+e^-$)$^{8}$Be.

considering External Pair Creation (EPC), the dot-dashed line represents the EPC calculated by Geant simulations, and the solid line represents the sum of the two. The Figures 1.16 b) and 1.16 d) shows the ratio of the experimental data over the expected values predicted by the model of Rose. The common discrepancies observed in the angles smaller than 50° are due to the EPC. Meanwhile, the evident deviation (at 4.5 $\sigma$) observed at higher angles in $^8$Be can be explained neither by nuclear structure effects nor by $E1$-$M1$ mixing for correlation angles larger than 50°. Assuming a short-lived boson with a mass of about 9 MeV/c$^2$, in competition with the two transitions, decreases the discrepancy observed. An upper limit for the branching ratio of $1.5 \times 10^{-4}$ was determined. Applying a similar assumption to the deviation in $^{12}$C, a five times smaller branching ratio is obtained ($3.1 \times 10^{-5}$).

### 1.4.3 2016: A. Krasznahorkay et al.

In 2016, J. Gulyás et al. reported the construction of a dedicated setup to study the IPC [4] at the Atomki Laboratories, Hungary. The motivation for studying this phenomenon was the deviation found by de Boer and the theoretical existence of a neutral boson. Furthermore, the rise of research on dark matter was attracted by this hypothetical particle and made it a candidate to be the Dark Photon or the intermediate boson for the unknown fifth force. The signature of a short-lived ($\tau < 10^{-13}$ s) neutral boson is a peak-like structure at large angles in the angular distribution of the lepton pair.

The experiment aimed to reinvestigate the isovector magnetic dipole transition in $^8$Be from the 17.6 MeV level and investigate the isoscalar dipole transition from the 18.15 MeV level ($\Gamma$ = 168 keV). The same reaction as Devons and de Boer was used ($^7$Li(p,$e^+e^-$)$^8$Be) at the same energy for studying the $1^+_1$ state, but to populate the $1^+_2$ state, the energy was increased to 1.03 MeV (see Table 1.2). Two different types of targets, 15 $\mu$g/cm$^2$ thick $LiF_2$, and 700 $\mu$g/cm$^2$ thick $LiO_2$ on 10 $\mu$m Al backing, were irradiated by a proton beam with a current of 1.0 $\mu$A.

The leptons were measured in a scintillator detector array of five $\Delta E - E$ telescopes placed at 0°, 60°, 120°, 180°, and 270°, perpendicular to the beam direction (see Figure 1.17 a)). The $\Delta E$ and $E$ components are of dimensions of $78 \times 60 \times 70$ mm$^3$ and $38 \times 45 \times 1$ mm$^3$, respectively. The setup is placed close to the end of the beamline, in a compact configuration as Figure 1.17 b) shows. In front of every telescope, a Multiwire Proportional Counter was placed

Table 1.2: Main electromagnetic transitions emitting $e^+e^-$ pairs via the IPC process by the irradiation of a $LiF_2$ target by a proton beam at 1.05 MeV energy

| **Nucleus** | **Transition** | **Type** | **Energy [MeV]** |
|---|---|---|---|
| $^{16}$O | $0_2^+ \rightarrow 0_1^+$ | $E0$ | 6.0482 |
| $^{8}$Be | $1_2^+ \rightarrow 2_1^+$ | $M1$ | 15.095 |
| $^{8}$Be | $1_2^+ \rightarrow 0_1^+$ | $M1$ | 18.128 |

to determine the incidence position of the positron and electron. Estimations performed by Geant4 simulations indicated an angular resolution of 7°.

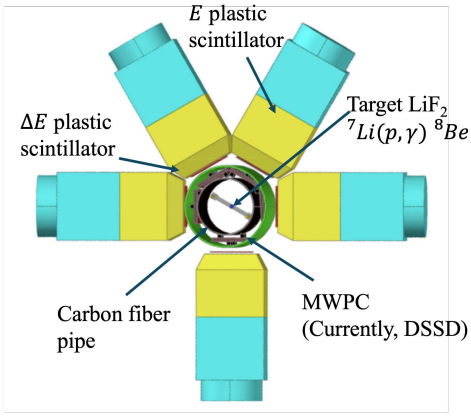


(a)

(b)

Figure 1.17: (a) CAD scheme of the pair spectrometer built at Atomki Laboratories, (b) Picture of the experimental setup [4].

Figure 1.18 a) shows the sum of energy deposited in the detectors in coincidence at 0.441 MeV proton beam energy. The high-energy peak corresponds to the transition from the 17.6 MeV state to the ground state in $^{8}$Be, the mid-energy one corresponds to the transition to the first excited state, and the low-energy one to the $0_2^+ \rightarrow 0_1^+$ in $^{16}$O.

The experimental angular distribution of the isovector transition (see Figure 1.18 a)) in $^{8}$Be slightly deviated from the theoretical calculation performed with the model of Rose [2, 3]. This behavior can be explained by adding a

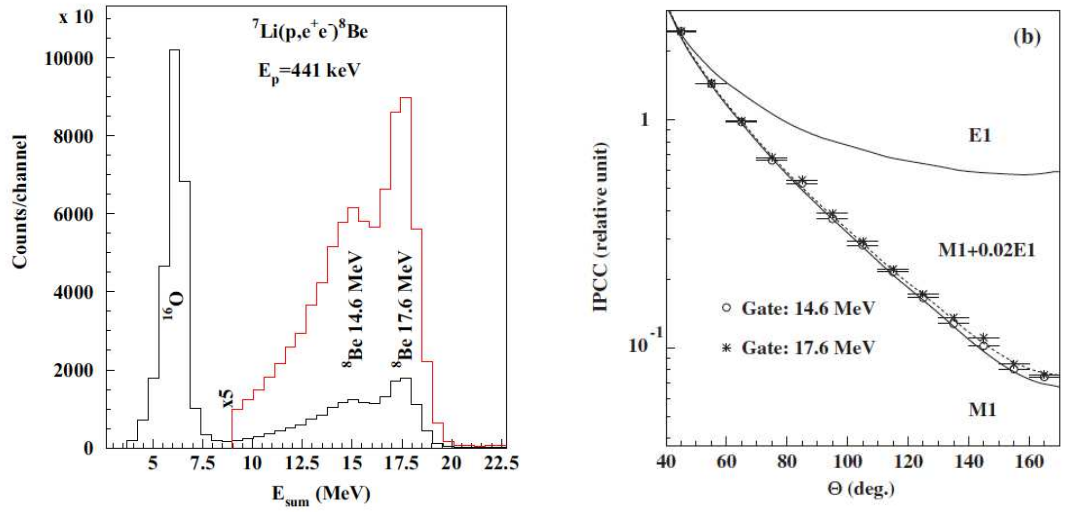


(a) (b)

Figure 1.18: (a) Sum energy spectrum of the pairs from the irradiation of a $LiF_2$ target by protons at the 441 keV energy [4], b) Angular distribution of the pairs from the 17.6 MeV transition in $^8$Be compared with the simulated angular one for M1 and E1 transition (solid lines) and a mixing of them dashed line [5]

.

contribution of 2% of $E1$ transition. In the case of the $E0$ transition in $^{16}$O, the theoretical model is consistent with the experimental angular distribution as Figure 1.19 b) shows.

Figure 1.19 a) shows the energy spectrum obtained when the energy was increased to study the 1.03 MeV resonance in $^8$Be. Figure 1.19 b) shows the angular distribution of the IPC with two different energy gate selections (15 - 18 MeV and 18 MeV). A condition in the energy asymmetry, defined in function of the electron ($E_{e^-}$) and positron ($E_{e+}$) energy, as $y = (E_{e^-} - E_{e^+})/(E_{e^-} + E_{e^+})$, was applied. In both cases, the model of Rose does not reproduce the experimental angular distributions at high angles (>120°). A peak-like structure is observed centered around 140°. This anomaly is more evident with a narrow gate at 18 MeV and can be explained neither by a contribution of a $M1$ transition nor by background gamma rays. Under the assumption of a neutral boson that decays into a positron and electron, the shape of the distribution can be reproduced with an isotropic emission of the pairs and the IPC process of a $M1$ transition.

Figure 1.20 has been produced by considering an IPCC for the $M1$ transition of $3.9 \times 10^{-3}$, a boson to $\gamma$ braching ratio of $5.8 \times 10^{-6}$. A $\chi^2$ method was applied to determine the mass of the boson, obtaining a value of $m_o c^2 = 16.7 \pm 0.35$(stat) MeV.

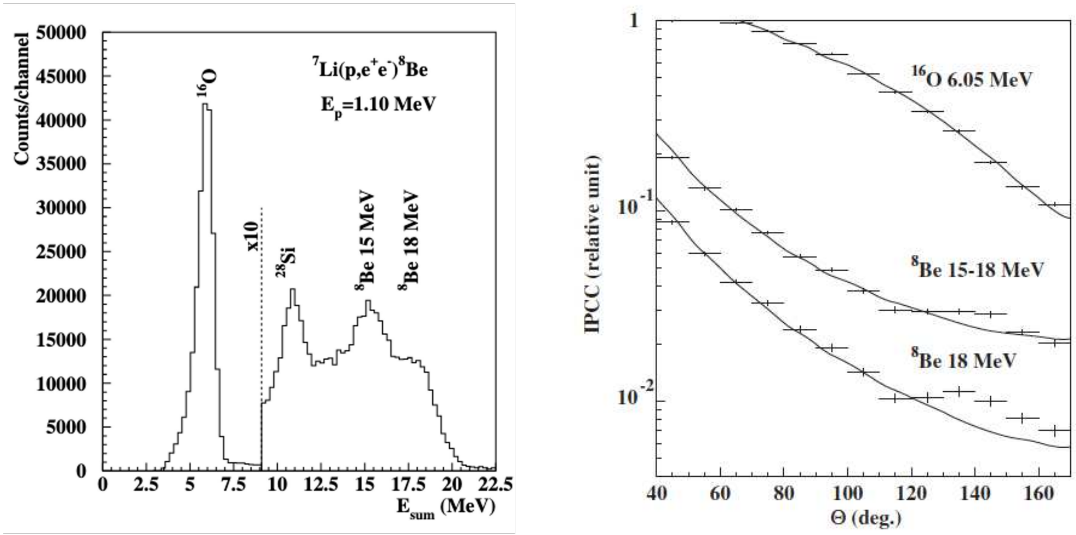


(a) (b)

Figure 1.19: (a) Sum energy spectrum of the pairs from the irradiation of a $LiF_2$ target by protons at the 1.03 MeV energy [16], (b) Measured angular correlations at 1.03 MeV beam energy. Theoretical estimations (solid lines) performed assuming $E0$ and $M1 + E1$ transitions [5].

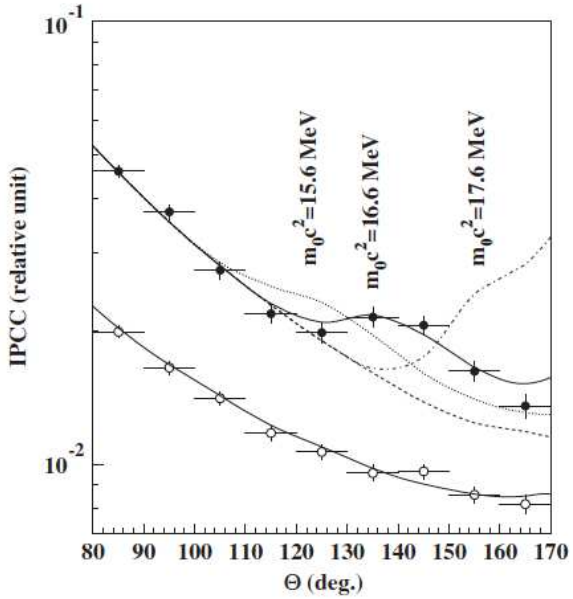


Figure 1.20: Angular distribution of the $e^+e^-$ pairs measured in the proton irradiation of the $LiF_2$ target at 1.10 MeV energy with the $|y| \leq 0.5$ condition (closed circles), and the $|y| > 0.5$ condition (open circles). The addition of simulations of the boson decay with different masses is shown [5].

Since, in the case of the isovector transition, it was possible to explain the deviation of the angular distribution by mixing a $M1$ and a $E1$ transition, the nature of the boson is deduced to be isoscalar. Due to the mass value, the claimed boson was named X17.

### 1.4.4 2024: A. T. T. Anh et al.

Recently, A. T. T. Anh et al. [17] corroborated the anomaly found by A. Krasznahorkay et al. [5]. A similar setup to the one used at Atomki [4] was built at the VNU University of Science (HUS, Vietnam). A two-telescope array was placed with a 140° (20° and 160°) separation angle (see Figure 1.21) to obtain maximum efficiency at the center of the peak structure in the IPC process in the isoscalar magnetic dipole transition in $^8$Be. The dimensions of the scintillator block were $82 \times 82 \times 80$ mm$^3$ each. Double-sided Silicon Strip Detectors (DSSD) were in front of the blocks to measure the incidence position of the leptons.

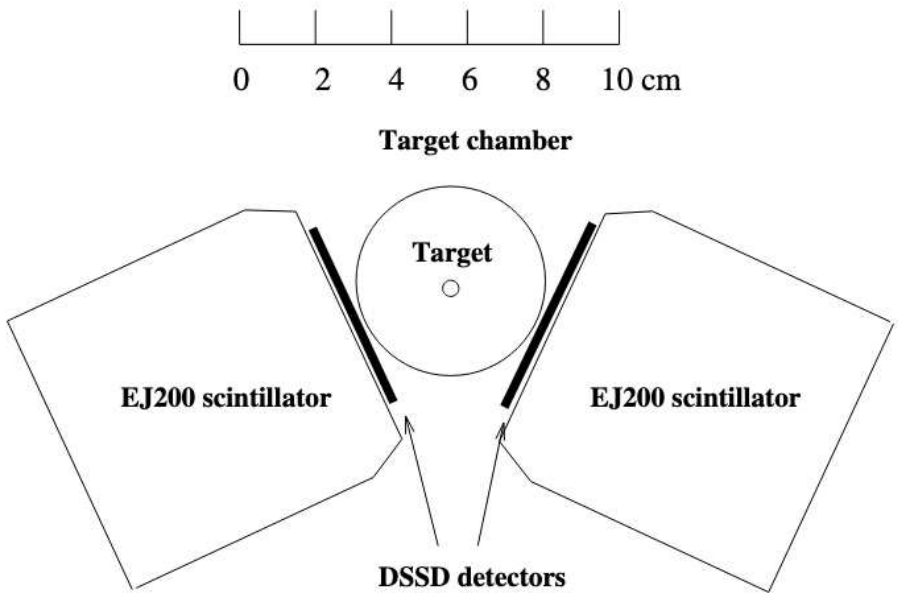


Figure 1.21: Pair of telescopes to measure $e^+e^-$ pairs in coincidence [17].

LiF targets with a thickness of ≈30 $\mu$g/cm$^2$ on ≈10 $\mu$g/cm$^2$ thick Al backing and ≈ 0.3 mg/cm$^2$ on 1 $\mu$g/cm$^2$ Ni were irradiated. The first one was used for calibration purposes and to study the isovector magnetic dipole transition in $^8$Be. In contrast, the second one was used to study the isoscalar magnetic dipole transition in the same nucleus. The proton beam energy was $0.4 < E_p < 1.3$ MeV

with a beam intensity of 1 - 1.5 $\mu$A.

The energy spectrum of the pair measured in coincidence was obtained by summing the energy deposited in every block. Figure 1.22 shows the energy transitions reconstructed by the analysis mentioned before by a bombarding energy of 441 keV. The authors reported that a background subtraction was applied, but it is unclear if Geant4 simulations or experimental data have achieved the estimation of this contribution. The energy spectrum is similar to the ones obtained by de Boer and Krasznahorkay but with a higher resolution. For the 17.6 MeV energy peak, a FWHM of 5.2% was obtained.

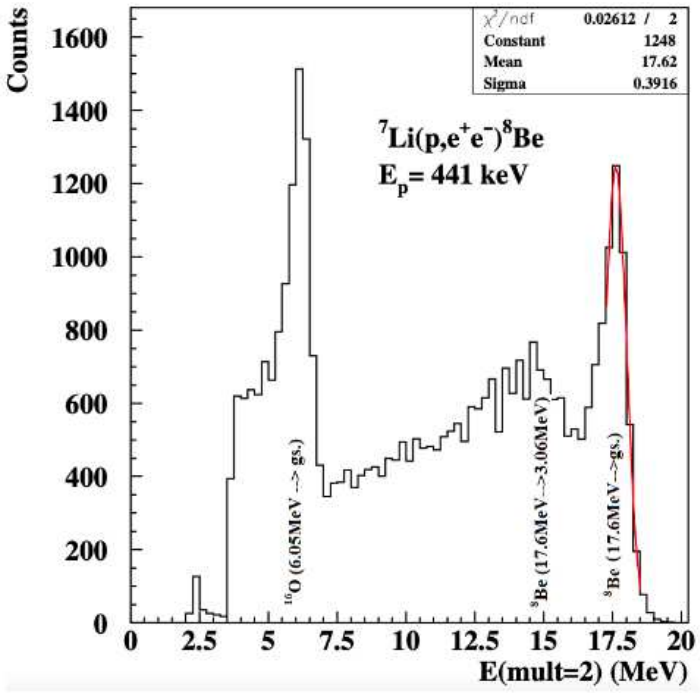


Figure 1.22: Sum energy spectrum of the pairs from the irradiation of a LiF target by protons at the441 keV energy [17].

The angular distribution is shown in Figure 1.23 a). A good agreement was obtained with Geant4 simulations, which included the geometry of the detectors, target, target backing, and arm structures. A dominant 87.4% of $M1$ and a contribution of 12.8% of $E1$ mixing transition were estimated for the angular correlation. An off-resonance experiment was performed at 800 keV proton beam energy. A similar analysis showed no deviation from the simulated angular distribution considering 48.9% $E1$ and 51.1% $M1$ mixing (see Figure 1.23 b)).

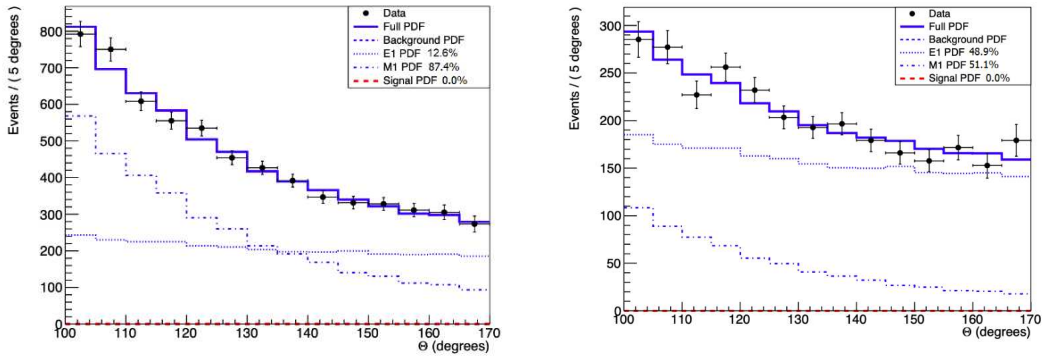


(a)




(b)

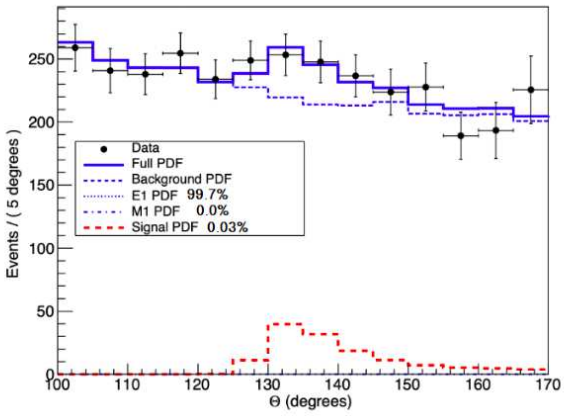


(c)

Figure 1.23: (a) Angular correlation of the pairs at a proton beam energy of 441 keV. The background line is the sum of the E1 and M1 transitions. The detection efficiency corrects experimental data and simulations. The point markers represent the experimental data; the blue solid line is the Probability Density Function; the dashed blue line is the cosmic background of the PDF; the blue-pointed line is the contribution of the $E1$ transition to the PDF, and the blue point-dashed line the contribution of the $M1$; the red dashed line represents the deviation of the PDF calculated and the experimental points, b) Same as a) but with a beam energy of 800 keV, c) Angular correlation of lepton pairs from the irradiation of $Li_2O$ target by 1.225 keV protons [17].

The last experiment explored the angular distribution effect at higher energies than the 1.03 MeV resonance. The beam energy was increased to 1.225 keV. The energy spectrum is not reported. A deviation around 135° was observed in the angular distribution (see Figure 1.23 c)) that the mixing of multipolarities cannot explain. Assuming the creation and decay of an intermediate particle, a mass of $m_X c^2 = 16.66 \pm 0.47$ (stat.) was estimated with a $4\sigma$ confidence. The branching ratio calculated was $2.8 \times 10^{-3}$ for the IPC and $1.1 \times 10^{-5}$ for the $\gamma$

to boson, which differs from the value obtained by A. Krasznahorkay [5]. The authors suggested a possible explanation for the neutral boson being created in the $E1$ transition instead of the $M1$ one.

### 1.4.5 Theoretical Interpretation of the X17 Boson

The anomaly found by A. Krasznahorkay and collaborators in the isoscalar magnetic dipole transition ($1_2^+ \rightarrow 0_1^+$) in $^8$Be was interpreted as the creation and subsequent decay of a previously unknown short lived ($\tau < 10^{13}$) neutral boson called X17 with a mass of $m_o c^2 = 16.7 \pm 0.35$(stat) MeV. This anomaly was not observed in the isovector magnetic dipole transition ($1_1^+ \rightarrow 0_1^+$), and it disappeared as long as the energy was increased from the resonance proton beam energy (1.03 MeV) that populates the $^8$Be$^*$ ($J^\pi = 1_2^+; I = 0$) state at 18.15 MeV. According to the authors, the X17 boson decays via the $e^+e^-$ pair emission, with a branching ratio of $B(^8\text{Be}^+ \rightarrow ^8\text{Be X17}) \,/\, B(^8\text{Be}^+ \rightarrow ^8\text{Be}\,\gamma) = 5.8\times10^{-6}$ (cosidering $B(\text{X17} \rightarrow e^+e^-) = 1$) with respect to the $\gamma$-ray emission.

The scalar nature of the X17 boson is constrained if the parity is conserved, since the $1^+ \rightarrow 0^+0^+$ transition contradicts the angular momentum conservation due that the requirement is to have a final angular momentum of $L = 1$, in contrast to the request by the parity conservation $+1 = (-1)^L$. J. L. Feng et al discuss the nature of this boson in [18] as a "*massive spin-1 Abelian gauge boson that couples non chirally to standard model (SM) fermions with charges $\varepsilon_f$ in units of $e$*".

Feng et al define a new lagrangias as:

$$\mathcal{L} = -\frac{1}{4}X_{\mu\nu}X^{\mu\nu} + \frac{1}{2}m_X^2 X_\mu X^\mu - X^\mu J_\mu \tag{1.35}$$

where $X_{\mu\nu}$ is the field strength of the X17 particle and couples to the current $J_\mu = \sum_f e\varepsilon_f \overline{f}\gamma_\mu f$. This current can be expressed at the nucleon legels as $J_\mu^N = e\varepsilon_p \overline{p}\gamma_\mu p + e\varepsilon_n \overline{n}\gamma_\mu n$, where $\varepsilon_p = 2\varepsilon_u + \varepsilon_d$ and $\varepsilon_n = \varepsilon_u + 2\varepsilon_d$.

The Atomki result request

$$\frac{B(^8Be^* \rightarrow ^8\, BeX17)}{B(^8Be^* \rightarrow ^8\, Be\gamma)} = (\varepsilon_p + \varepsilon_n)^2 \frac{|\overrightarrow{p_{X17}}|^3}{|\overrightarrow{p_\gamma}|^3} \approx 5.8 \times 10^{-6} \tag{1.36}$$

For a mass $m_{X17} = 17$ MeV $\Rightarrow |\varepsilon_p + \varepsilon_n| \approx 0.011$

$$\Rightarrow |\varepsilon_u + \varepsilon_d| \approx 3.7 \times 10^{-3} \tag{1.37}$$

Even when there are no restrictions for the X17 decaying through $\nu\overline{\nu}$ or $\gamma\gamma\gamma$ emission, Feng et al. mentioned that the $\gamma\gamma$ decay is negligible, and they assumed that the $\nu\overline{\nu}$ is highly suppressed. According to [19], the decay of the X17 through its electron coupling has a width of:

$$\Gamma(X17 \rightarrow e^+e^-) = \varepsilon_e^2 \alpha \frac{m_{X17}^2 + m_e^2}{3m_{X17}} \tag{1.38}$$

where short decay lenght of the X17 boson ($L \approx \varepsilon_e^{-2} 1.8 \times 10^{-12}$) implies:

$$|\varepsilon_e| \gtrsim 1.3 \times 10^{-5} \tag{1.39}$$

On the other hand, the anomaly trace factor ($N_\pi \equiv (\varepsilon_u q_u - \varepsilon_d q_d)^2$) is limited by the dark photon bound $N_\pi < \varepsilon_{max}^2/9$. This result implies that

$$|2\varepsilon_u + \varepsilon_d| = 8 \times 10^{-4} \tag{1.40}$$

Since Equations 1.37 and 1.40 must be satisfied with a ~10% cancellation, the following relations are found:

$$-2.3 < \frac{\varepsilon_d}{\varepsilon_u} < -1.8 - 0.067 < \frac{\varepsilon_p}{\varepsilon_n} < 0.078 \tag{1.41}$$

According to the authors [18], *"we call the general class of vector models that can both explain the $^8$Be and satisfy pion decay constraints* ***protophobic****"*.

## 1.5 Motivation for New Experiments

The relevance of the results recently obtained by A. Krasznahorkay et al. motivates the development of a new experimental program. The main goal of this activity is the independent reproduction of the experimental results and, possibly, a more detailed characterization of the anomalous angular distribution. This is the subject of the present thesis work, where a new detection setup was developed and characterized, and preliminary data allowed us to evaluate its performance. While writing this thesis, the MEG II collaboration reported its results on investigating the $^8$Be [20]. The experiment was performed at the Paul Scherrer Institute (PSI) in Switzerland. LiPON (lithium phosphorus oxynitride) targets of $\approx 7$ $\mu$m thickness were irradiated with a 1.1 MeV proton beam. The $e^+e^-$ pairs from the IPC in $^8$Be, via the nuclear reaction $^7$Li(p,$e^+e^-$)$^8$Be, were

detected in the MEG II apparatus (see Figure 1.24). This machine consists of a multi-wire cylindrical drift chamber made up of (CDCH) 1728 separate cells and two 256 scintillator tiles read out by SiPM (pTC) to measure the timing of the ions. In addition, a $4 \times 4$ Bismuth Germanate (BGO, with a crystal matrix of $4.6 \times 1.6 \times 20$ cm$^3$ each) was placed for $\gamma$ rays measurements. The detector array is inside a solenoid aligned with the beam axis and features a gradient magnetic field (COBRA) of 1.27 T. The analysis method is based on reconstructing the $e^+e^-$

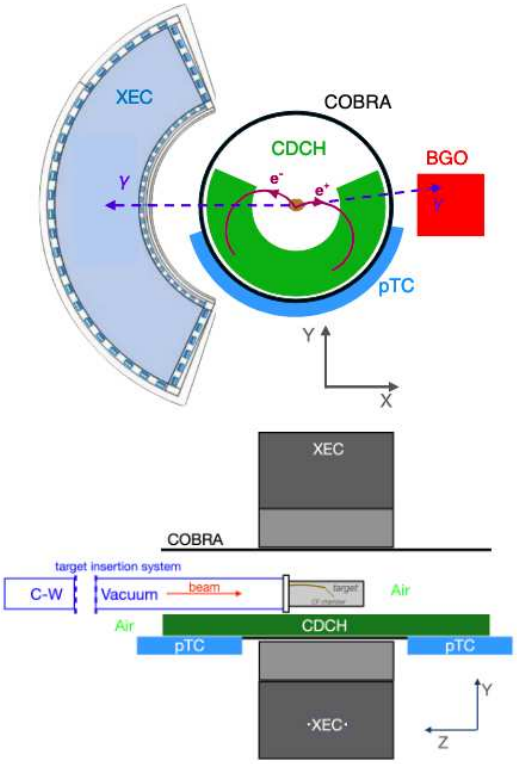


Figure 1.24: Scheme of the MEG II apparatus [20].

trajectory inside the CDCH. This information is used to determine the energy of the $e^+e^-$ and their relative angle (See Figure 1.25). The likelihood method was implemented to compare the experimental results with the Zhang-Miller (Z-M) model, which accounts for photon anisotropy and multiple interferences. The group reported: *In our dataset,* $^8Be^*(18.1) \rightarrow {}^8Be + e^+e^-$ *represents 21.6(25)% of all IPC transitions to ground state. No significant evidence of the X17 particle was found*. This result, in contrast with the Atomki results, further motivates the completion of the experimental activity presented in this work.

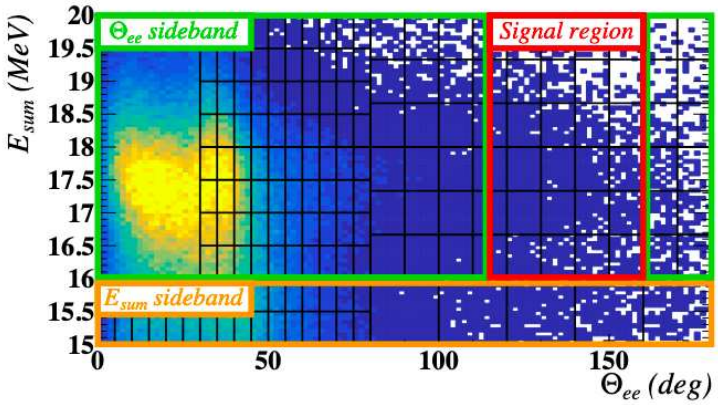


Figure 1.25: Sum energy of the $e^+e^-$ versus its relative angle. The orange sideband contains events out from the region of interest. The green sideband contains events of the transition of interest in $^8$Be (isoscalar transition from the $1^+_2$ state). Angles smaller than 80° were not considered since a high dependency of the beam spot in the target was observed. The red sideband contains the expected events with a signal of the X17 boson [20].

# 2

# Design of a new $e^+e^-$ Pair Spectrometer

*The present chapter describes the design and the Monte Carlo simulation of the $e^+e^-$ pair spectrometer built to study the IPC in $^8$Be. The first section describes the components of the detectors of the $e^+e^-$ pair spectrometer. The second section describes the Geant4 simulation, from the geometrical constructions to the description of the $e^+e^-$ emission. The last section is an overview of the simulation analysis and concludes with an evaluation of the $e^+e^-$ detection efficiency.*

## 2.1 Conceptual Design

The design of the $e^+e^-$ pair spectrometer aimed to address the main challenges in the IPC angular measurements. The detector array must determine the energy deposited in the range of interest, precise position, lepton-$\gamma$ discrimination, and perform coincidence measurements. Those characteristics can be affected by the $\gamma$-ray background and the tortuous path of the leptons inside matter.

The $\Delta E - \Delta E - E$ telescope detector configuration (see Figure 2.1 ) has been chosen because it allows the $\gamma$-lepton discrimination by asking for the coincidence between the $\Delta E$ and $E$ parts of the detector.

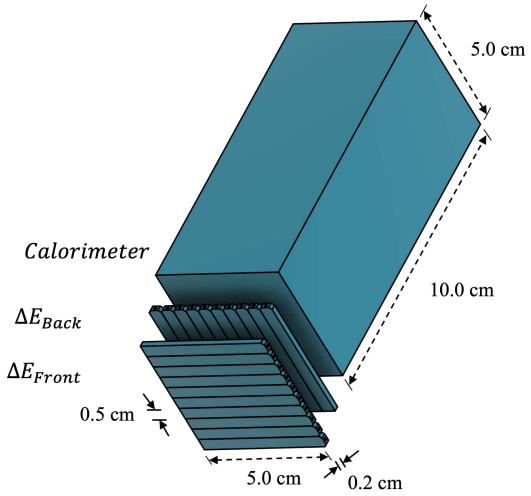


(a)

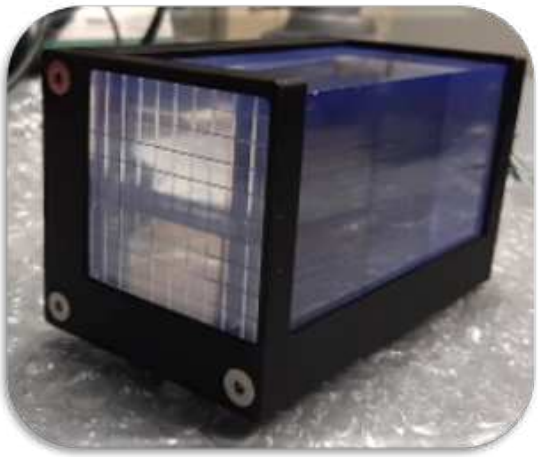

(b)

(c)

Figure 2.1: a) Components of one $\Delta E - \Delta E - E$ telescope detector (courtesy of Diego Tagnani), b) One telescope assembled, c) Four telescopes assembled in the clover configuration.

### Calorimeter

The energy of the $1_2^+ \rightarrow 0_1^+$ transition in $^8$Be is 18.128 MeV. This value means that the material used in the construction has to be able to measure energies between 1-18 MeV since the energy is shared between the electron and the positron. Scintillator materials are good candidates because of the high scintillation efficiency from the lepton interaction and the lower cost than the solid-state ones. Guyas et al. [4] have shown that polyvinyl toluene is among the best candidates. Table 2.1 compares the scintillator products of the Eljen Technology Company [21]. The EJ-200 scintillator has important features that are helpful for this

application, such as fast timing, long optical attenuation, high light efficiency production, and maximum emission wavelength (compatible with SiPM detectors, discussed later). Those characteristics make it ideal to be selected for the detector array construction. In addition, this material can be modeled in different shapes. The rectangular cuboid has some advantages over others, like the easy assembly of multiple blocks.

Table 2.1: Comparison among the commercial scintillators of the Eljen Technology Company [21].

| **Properties** | **EJ-200** | **EJ-204** | **EJ-208** | **EJ-212** |
|---|---|---|---|---|
| Light Output (% Anthracene) | 64 | 68 | 60 | 65 |
| Scintillation Efficiency (photons/1 MeV $e^-$) | 10,000 | 10,400 | 9,200 | 10,000 |
| Wavelength of Maximum Emission (nm) | 425 | 408 | 435 | 423 |
| Light Attenuation Length (cm) | 380 | 160 | 400 | 250 |
| Rise Time (ns) | 0.9 | 0.7 | 1 | 0.9 |
| Decay Time (ns) | 2.1 | 1.8 | 3.3 | 2.4 |
| Pulse Width, FWHM (ns) | 2.5 | 2.2 | 4.2 | 2.7 |
| No. of H Atoms per cm3 ($x10^{22}$) | 5.17 | 5.15 | 5.17 | 5.17 |
| No. of C Atoms per cm3 ($x10^{22}$) | 4.69 | 4.68 | 4.69 | 4.69 |
| No. of Electrons per cm3 ($x10^{23}$) | 3.33 | 3.33 | 3.33 | 3.33 |
| Density ($g/cm^3$) | 1.023 | 1.023 | 1.023 | 1.023 |
| Polymer Base | Polyvinyltoluene | | | |
| Refractive Index | 1.58 | | | |
| Softening Point | 75°C | | | |
| Vapor Pressure | Vacuum-compatible | | | |
| Coefficient of Linear Expansion | $7.8 \times 10^{-5}$ below 67°C | | | |
| Light Output vs. Temperature | At 60°C, L.O. = 95% of that at 20°C | | | |
| Temperature Range | -60°C to 60°C | | | |

According to Geant4 simulations, the energy loss in the material is close to 2 MeV per centimeter. Considering this value and the energy of the transition of interest, the natural dimension choice of one side of the block is 10 cm (calorimeter). Taking advantage of the geometry discussed, the other two dimensions can be 5 cm, and by assembling four blocks, a 10x10x10 $cm^3$ block can be created. Thus, the option chosen for the telescope is a single block of 5.0×5.0×10.0 $cm^3$ (see Figure 2.2). The most common option is to read out the scintillating light using Photomultiplier Tubes (PMT). However, new technologies allow us to build more compact arrays that can be placed in the same reaction chamber as

the target. Silicon Photomultipliers (SiPM) are convenient options because they come in several sizes. The light detectors, two $6 \times 6$ mm$^2$ SIPMs, have been placed in the back face of the calorimeter. The coincidence of the two SiPM is used to read the light emitted by the calorimeter, thus reducing the impact of the dark current of the SiPM and allowing to lower the individual detection threshold on the SiPM. The energy deposited can be calculated by summing up the signal, event by event, of the two SiPMs:

$$E_{cal} = sig_{SiPM_1} + sig_{SiPM_2} \tag{2.1}$$

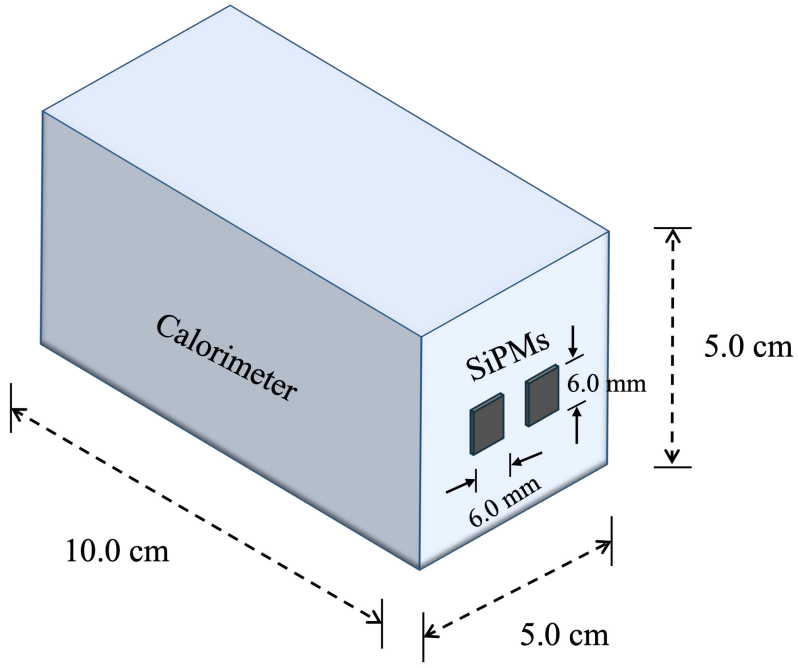


Figure 2.2: Scintillator calorimeter and two SiPM in its back face for reading out the light.

The SiPM option selected is the Hamamatsu S13360-6075CS 6.0x6.0 mm$^2$ [22] (Operation Voltage Bias 55/60V and 0.01 mA from Aim-TTi PLH120 DC Power Supply [23]. Low Voltage 2.5 V and 0.77 A from Rigol DP832 Power Supply [24]) with a pixel pitch: 75 $\mu$m. Figure 2.3 a) shows the spectrum of the light emitted by the scintillator and Figure 2.3 b) shows the efficiency of the SiPM as a function of the wavelength. The maximum emission of light from the scintillator and the maximum efficiency of the SiPM is in the wavelength range of 400-500 nm. Therefore, this type of SiPM can read out the light emitted from the calorimeter. To avoid the light diffusing out of the scintillator material, the

calorimeter blocks were polished and painted with the refractive paint EJ-510 by Eljen Technology Company [25].

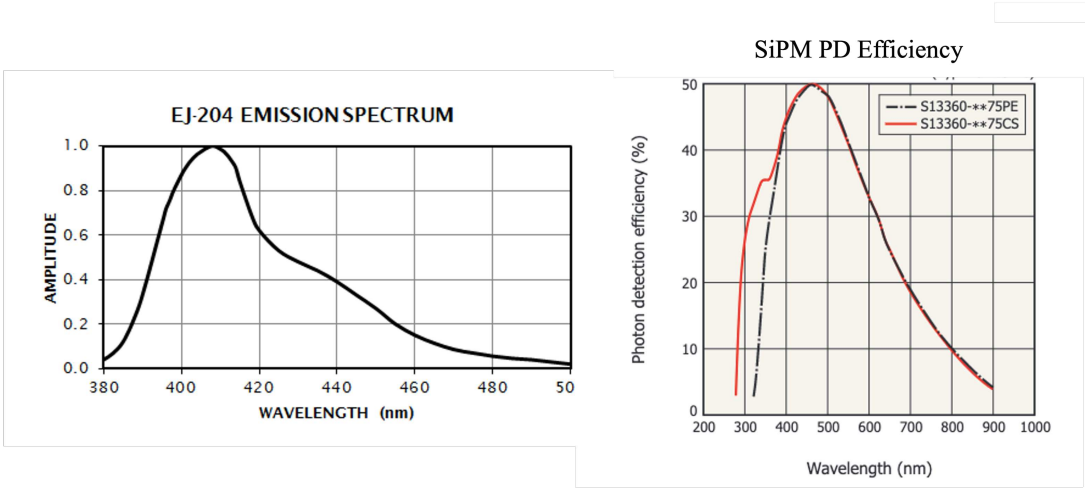


a) b)

Figure 2.3: a) Light spectrum emission of the scintillator EJ-200 [21] and b) the efficiency of the Hamamatsu S13360-6075CS SiPM [22] as a function of the wavelength.

### System of Bars

In the design of a $e^+e^-$ position interaction detector, the thickness selection is based on the amount of detector material needed to generate a signal above the noise. Another essential characteristic of this detector is the low-Z to reduce the scattering. Even when the material has a low Z, the probability of scattering increases with the thickness; therefore, the detector has to be as thin as possible. For those reasons, the polyvinyl toluene material was chosen for the position interaction part of the detector because it achieves the characteristic of being a low-Z material since it is an organic scintillator (mainly in the form of H, C, and O). In contrast, silicon detectors have a higher Z, and the price per $cm^2$ is higher than that of scintillators. The option selected was the construction and design of a new scintillator array position sensible based on the EJ-200 material, but several conditions had to be addressed. The unit of the array is a rectangular cuboid bar. The dimension sizes $0.5 \times 5.0 \times 0.2$ $cm^3$ were chosen to match the block described in the previous section and obtain an angular resolution lower than $\sim 3°$ at around 10-15 cm distance from the target position. This bar geometry was chosen since it offers the possibility of easy assembly in more

complex structures. In addition, a local coordinate system can be defined by the grid generated by the front and back bars in perpendicular configuration (see Figure 2.4).

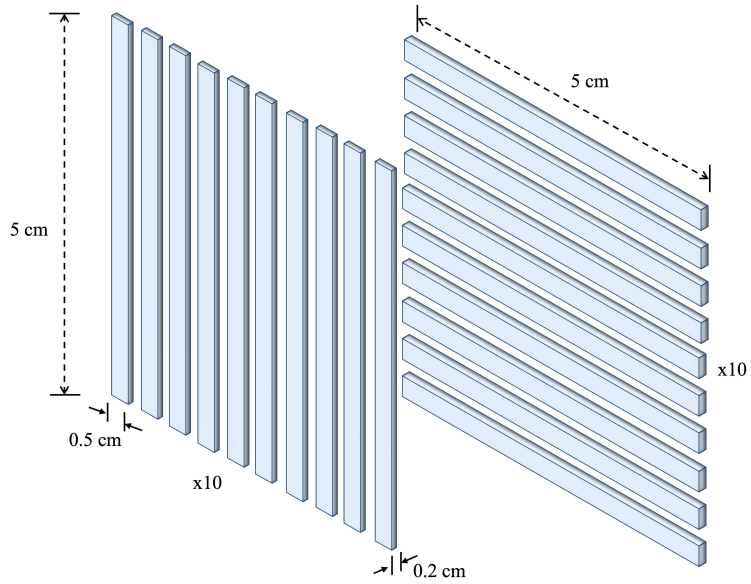


Figure 2.4: Bars grid configuration. Ten bars are placed at the front face of the telescope in a vertical configuration. Behind those bars, a second set of ten bars is placed perpendicular to the first ones. This system of bars is used to determine the position of ions.

Due to the size of the individual bars, the best option is using SiPM. The new technologies allow us to use tiny light detectors. In our case, a set of 10x1 SiPM of 3x3 $mm^2$ has been used to read out the scintillating light. The electronic system has been designed at the Fondazione Bruno Kessler (FBK [26]) by Fabio Acerbi. The bars shape was modified for a better match of one face and the SiPM, reducing the dimension in the upper part as the Figure 2.5 a) shows. The refractive painting EJ-510 was used to cover the bar surface. One problem encountered during the first test was a lower light collection efficiency due to the internal reflection in the bar because of its size. In other words, the light is attenuated before reaching the SiPM because its path could be longer than the size of the axis of the bar (5 cm). The solution implemented was to drill a 1 mm canal through this axis. An optical fiber was placed inside the bar as the Figure 2.5 b) shows.

If every bar had its dedicated readout channel, the number of channels in the acquisition for every telescope would be 20 (excluding the channels for the calorimeter), which is a large number that would have strongly limited the

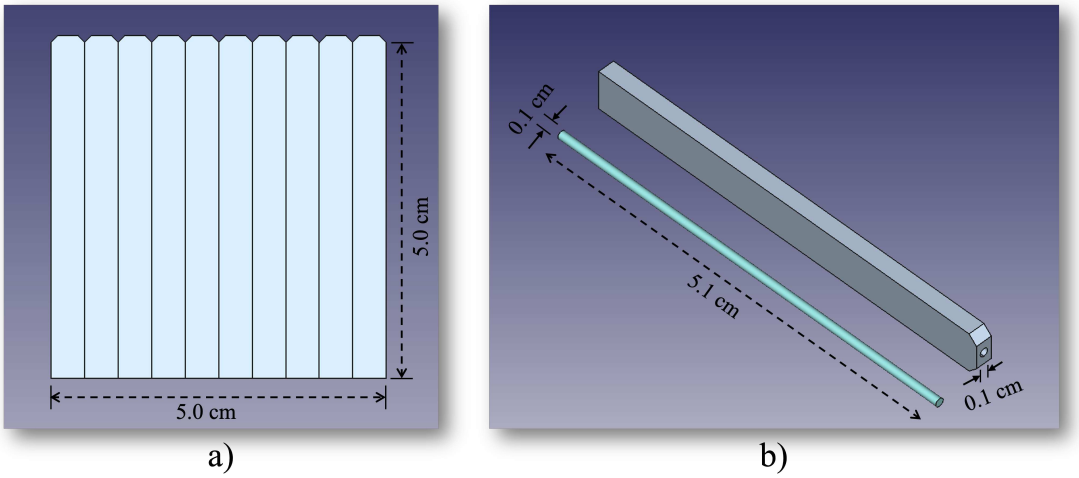


Figure 2.5: a) Set of 10 bars with a reduction of their size on the top for the SiPM coupling, b) optical fiber and scintillator bar.

number of telescopes to be used in the experiment. Thus, a reduced channel technology [27] was implemented, allowing us to use only two channels for every set of 10×1 SiPM to determine the fired bar. In other words, it is possible to decrease the number of channels by a factor of ~5, having only four channels per telescope. The method consists of splitting the signal collected from a SiPM. The electronic board uses a system that weights these signals using the values in Table 2.2. The weight performance is achieved using different resistor values in two groups (left and right). So, the split left signal ($sig_l$) is created after weighting the values of the signals of the 10 SiPM in the board by the values in the column "Weight (Left)" of Table 2.2. The split right signal ($sig_r$) is generated similarly but with the values of column "Weight (Right)." To recover the original signal, summing the two signals generated is sufficient:

$$E = sig_r + sig_l; \tag{2.2}$$

On the other hand, the subtraction of the two signals and the normalization with the sum indicates the SiPM that fired:

$$x = \frac{sig_r - sig_l}{sig_r + sig_l} = \frac{sig_r - sig_l}{E}; \tag{2.3}$$

A strong dependency on the temperature in the performance of the bars system was observed in experiments performed by F. Acerbi [27], setting the temperature from 0° to 30° and sending light from a pulse-LED. The best position

Table 2.2: Weights of every SiPM in a board for 10 bars.

| SiPM | Weight (Left) | Weight (Right) |
|---|---|---|
| 1 | 1.0 | 0.1 |
| 2 | 0.9 | 0.2 |
| 3 | 0.8 | 0.3 |
| 4 | 0.7 | 0.4 |
| 5 | 0.6 | 0.5 |
| 6 | 0.5 | 0.6 |
| 7 | 0.4 | 0.7 |
| 8 | 0.3 | 0.8 |
| 9 | 0.2 | 0.9 |
| 10 | 0.1 | 1.0 |

determination has been obtained at 0° (see Fig. 2.6). This information was crucial for the design of the board support. The electronic boards were attached to a metallic empty block with the option to be filled with a specific liquid (see Figure 2.7), which, in this case, was an anti-freezer at 0°. The bars and the SiPM were assembled using optical cement to couple the refractive index of the components.

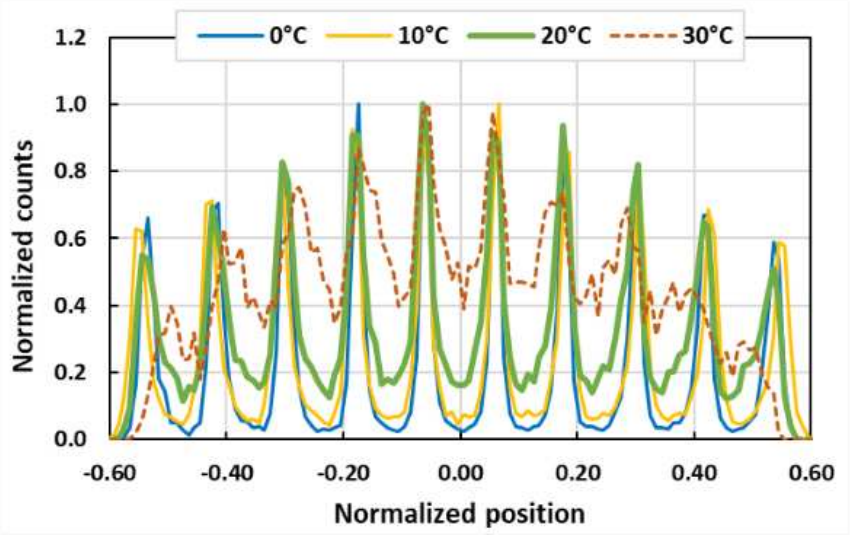


Figure 2.6: Performance of the 10x1 SiPM board at different temperatures [27].

### Clover Description.

Assembling four telescopes in a cluster implies having better angular coverage and a bigger calorimeter to increase the probability of stopping the leptons

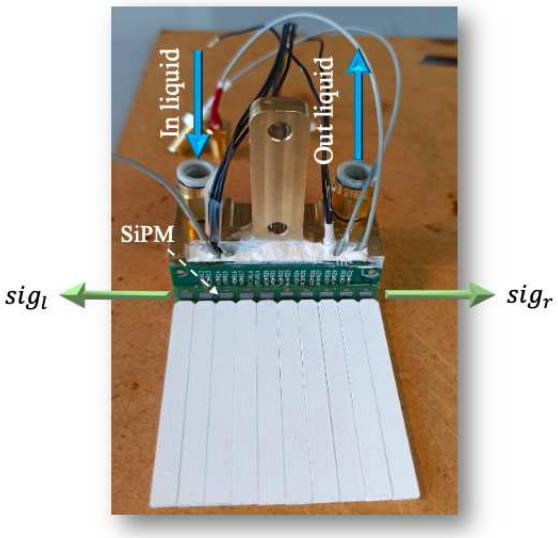


Figure 2.7: 10 bars coupled to a 10x1 SiPM board.

inside the detector. From now, the cluster detector will be called "Clover". A Clover support has been designed (see Figures 2.8 and 2.10). This support holds a liquid distributor that splits one pipe to spread the liquid to the eight boards in one clover and one distributor to take the output. The support also allows for fine-tuning the distance from the target with a tolerance of 1 cm. The elements of the Clover, the cooling system, and the support are vacuum-compliant. Figures 2.9 and 2.10 show the cooling and electronic connections of the clover detectors. Thus, the complete setup and target can be placed inside the reaction chamber.

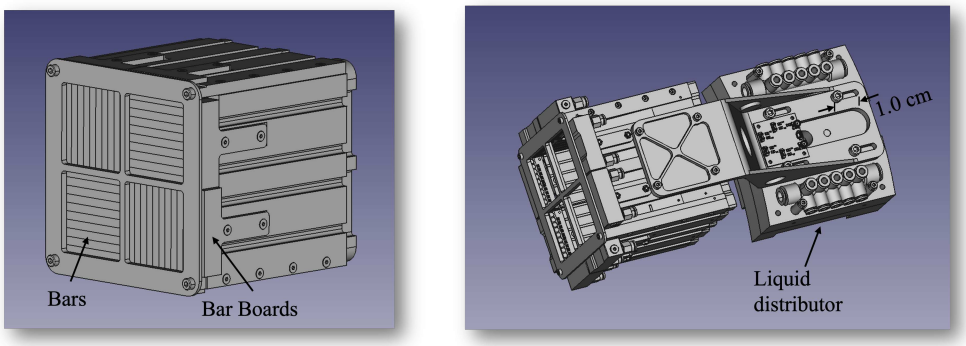


Figure 2.8: a) Clover structure b) Clover support (courtesy of Diego Tagnani).

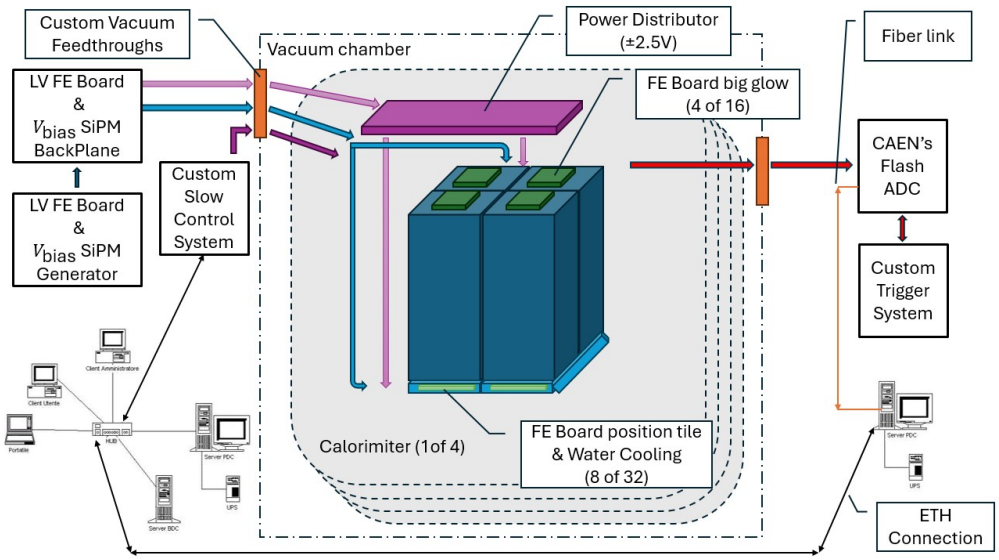


Figure 2.9: Diagram of the cooling and electronic connections of the clover detectors. In orange, the feed-throughs contain the connection between the inside and outside of the reaction chamber. The low voltage (LV) is shown in violet, where inside the chamber is a power distributor for the calorimeter and bars. The voltage bias for the SiPM is shown in blue. A slow control system regulates the intensities of the voltage. The cooling system is shown in green for the bars boards. The signals from the clover are collected and sent to the CAEN Digitizers and the acquisition PC. (courtesy of Diego Tagnani)

## 2.2 Geant4 Simulation

Geant4 offers classes that allow us to construct complicated geometries, define particles and materials, track particles, evaluate deposited energy in different materials, produce secondary particles, and more (see reference [28]). The simulation package has a graphical interface to visualize the detector array and particles.

### 2.2.1 Simulation Construction

From a global point of view, the simulation construction is divided into two parts: the geometrical construction of the $e^+e^-$ pair spectrometer and the emission of radiation. The Monte Carlo Simulation Package Geant4 offered the ideal framework for building it. The geometry of the $e^+e^-$ pair spectrometer has four essential elements: bar, optical fiber, block, and paint coat. A previous simulation can be found in [29], but the missing of a more realistic geometrical

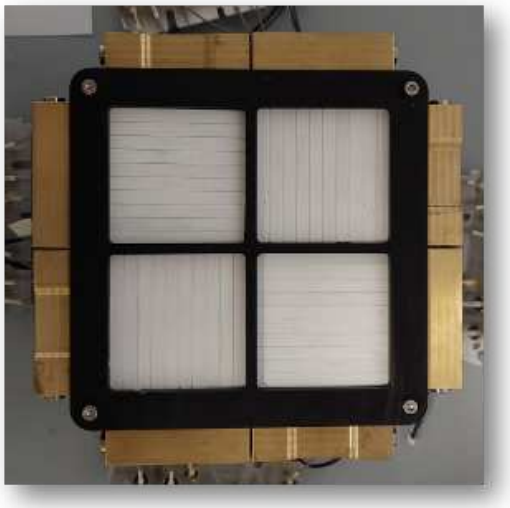

(a)

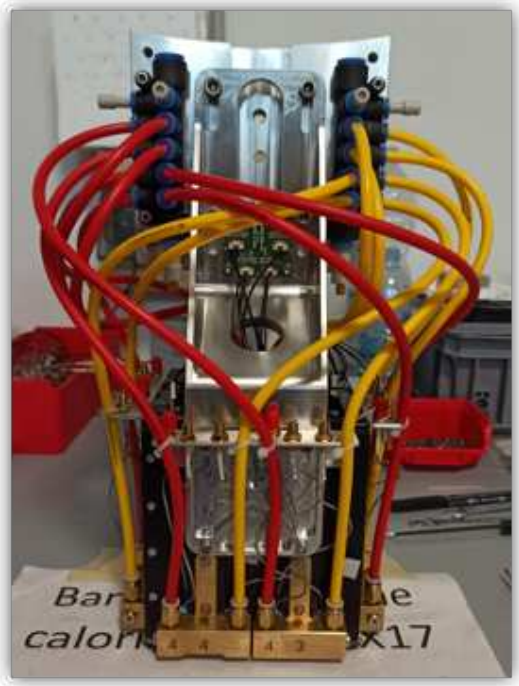

(b)

Figure 2.10: Pictures of a clover detector in its support (a) front face, where the bars can be seen (b) Lateral view, where the pipes for the antifreeze liquid are shown.

construction, an energy distribution of the shared energy between the $e^+$ and the $e^-$ (different from a uniform one), and a method to simulate the position interaction reconstruction complicated the comparison with the experiments

performed in this work (see Chapter 4). In order to comply with such requests, a new simulation has been developed.

### Detector Geometry Description

#### Bar geometry

The bars are the unit elements of the ΔE-layer of the telescope. The first step is to describe this basic structure. As Chapter 3 describes, the bars have a canal and an optical fiber is inserted in it (see Figure 2.11 a)). Two coating layers of the refractive paint EJ-510 [25] cover the long sides of the bar (see Figure 2.11 a)), excluding the face in contact with the SiPM. The geometric construction of the bar contains three 3D components: a box, a trapezoidal prism, and a cylinder.

The base of the structure is a $0.2 \times 0.5 \times 5.0$ cm$^3$ box of plastic scintillator polyvinyl toluene ($[CH_2CH(C_6H_4CH_3)]_n$), whose name in the Geant4 library is G4_PLASTIC_SC_VINYLTOLUENE. An extension bar with a cross-section reduction function has been applied at one of the ends of the box to attach the bar to the $0.3 \times 0.3$ cm$^2$ SiPM. In the simulation, this part has been designed with a trapezoidal prism with a square base of $0.2 \times 0.5$ cm$^2$, a top ceiling of $0.2 \times 0.3$ cm$^2$, and a height of 0.3 cm. A union method has been applied to the box and the extension to join them and create the final prototype of the scintillator bar (see Figure 2.11 b)).

The next step is to "drill" the bar and define the optical fiber. Both processes used a cylinder with a 0.5 mm radius and 1.1 cm height. Then, the cylinder volume was removed from the bar using a boolean volume subtraction method along its axis. The material used for the optical fiber is plexiglass ($[C_5H_8O_2]_n$), whose name in the Geant4 library is G4_PLEXIGLASS. Figure 2.11 c) shows the assembly of the bar and the optical fiber.

The painting coat is constructed by defining a box plus a bar extension and adding a 0.1 mm paint thickness in every dimension, excluding the face in contact with the SiPM. The value of the paint thickness was calculated from the nominal value shown on the website of the EJ company [25] and considering only two coating layers. By subtracting the bar volume from this volume, a two-layer coating paint is obtained. The material used for the refractive paint was taken from the data proportioned by the company [25]. The paint material was defined using the proportions shown in Table 2.3, and a 13.0 mg/cm$^2$ density. The final bar includes the scintillator bar, the optical fiber, and the painting coat

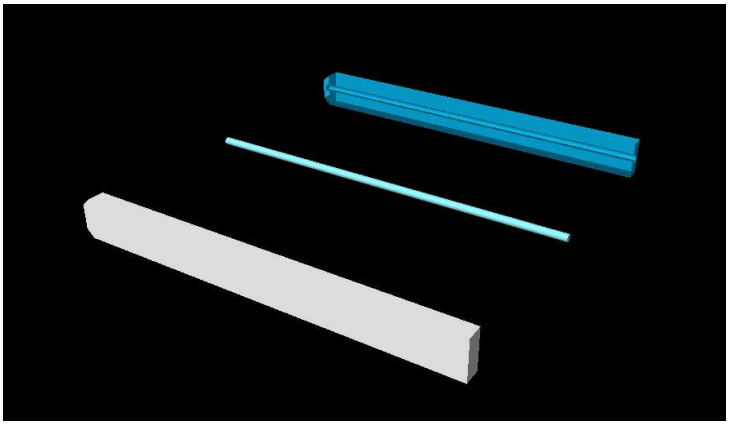

(a)

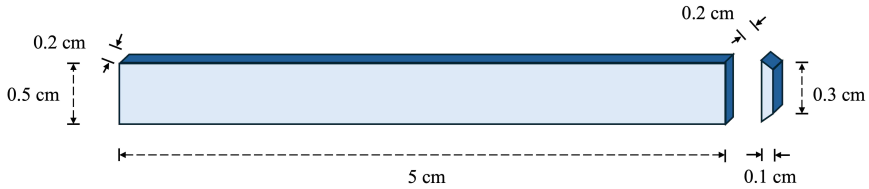


(b)

(c)

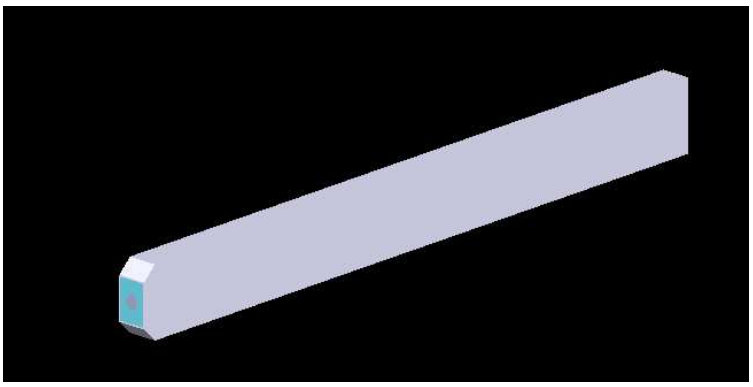

(d)

Figure 2.11: a) Geometric components of one single bar (from top to bottom): scintillator bar, optical fiber, and two layers of coat paint, b) Scintillator bar: box base (at the left) and extension bar (at the right), c) Optical fiber inside a scintillator bar, d) Final bar model including the scintillator part (blue), the optical fiber (violet), and the paint coating (white).

see (Figure 2.11 d)).

Table 2.3: Scintillator bar: box base (at the left) and extension bar (at the right).

| Component | Atoms per $cm^2$ |
|---|---|
| **Ti** | $6.71 \times 10^{19}$ |
| **C** | $1.12 \times 10^{20}$ |
| **H** | $2.25 \times 10^{20}$ |
| **O** | $1.90 \times 10^{20}$ |

### Calorimeter Geometry

In contrast with the bar construction, the calorimeter consists only of two elements: the scintillator block and the two-layer paint coating. For both, the box shape was used: the first one was a $10.0 \times 5.0 \times 5.0$ $cm^3$ box (see Figure 2.12 a)), and the second was a similar box but added the paint thickness (see Figure 2.12 b)), excluding the back part where the two $6.0 \times 6.0$ $cm^2$ SiPMs are placed. Figure 2.12 c) shows the front face of the "painted" calorimeter and Figure 2.12 d) the back face.

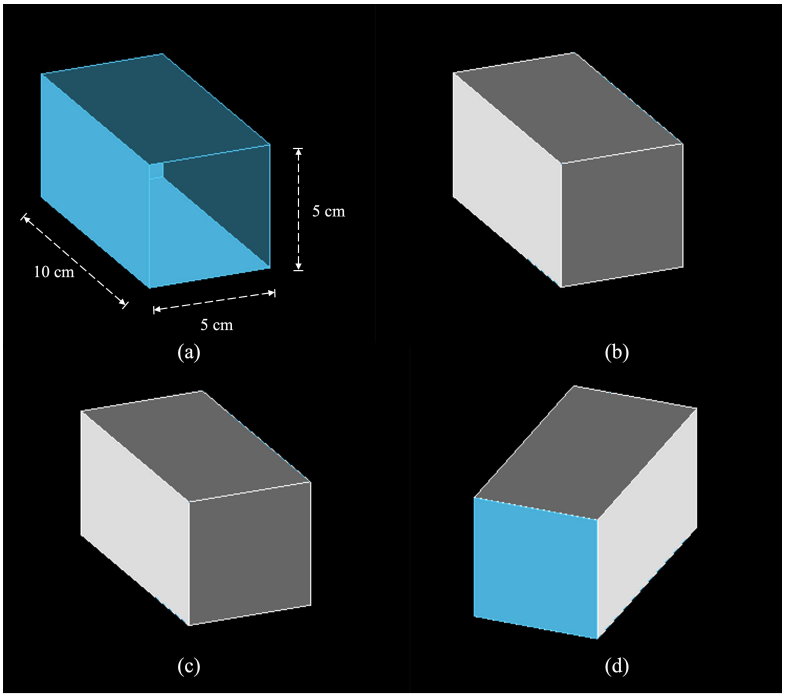


Figure 2.12: Calorimeter: a) scintillator block, b) paint coating, c) front, and d) back face of the "painted" block.

### Telescope Assembly

The telescope detector is created by assembling the front and back bars structures and the calorimeter. The building of the telescope starts with the ΔE-layer. The front bars structure contains ten copies of the bar geometry. The back bars structure contains ten additional bars rotated 90° with respect to the front bars. The order of the definition of the bars is crucial because its function is to determine the incidence position of the $e^-e^+$. The building loop has been performed from left to right and from bottom to top. The last structure defined is the E-layer, which consists of the calorimeter. It is positioned after the structure of the back bars. All placement definitions have considered the paint thickness to avoid overlapping among the different structures. Figure 2.13 a) shows the assembly of one telescope.

### Clover Assembly

The *clover* assembly consists of clustering four telescopes in a square configuration (see Figure 2.13 b)). The reduced part of the bars is in the outer part of the clover where the SiPMs are placed.

As a final step, the clover is placed in the corresponding position in the array. First, it is translated to the target-distance position and then rotated to the corresponding angle. Figure 2.14 shows three examples of detector array configurations with detector at:

- Conf 1: 30°, 315° (Figure 2.14 a))
- Conf 2: 30°, 165°, 240°, 315°, (Figure 2.14 b))
- Conf 3: 30°, 150°, 240°, 330° (Figure 2.14 c))

Those configurations used in the experimental data-taking (see Chapter 4) need to be evaluated in terms of detection efficiency. The detection efficiency will be discussed in the last section of this Chapter.

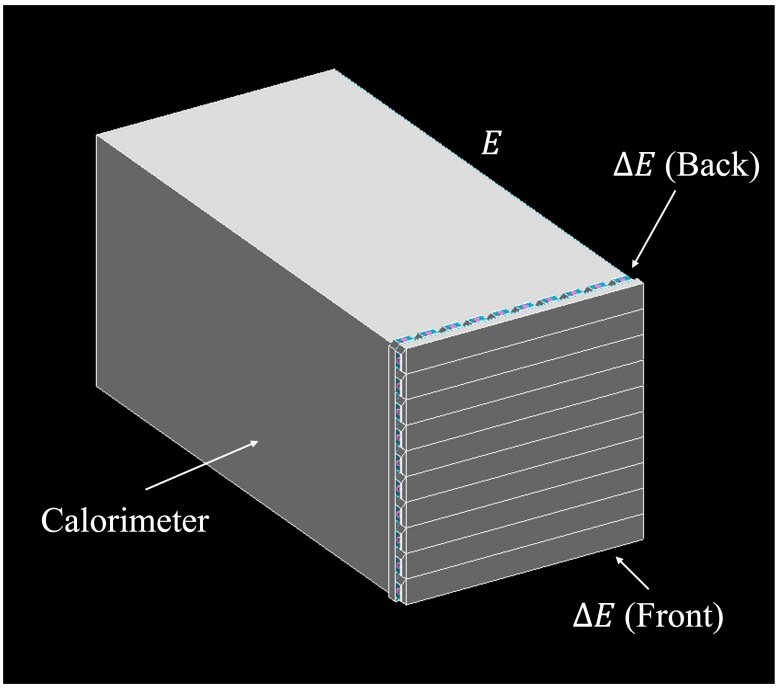


(a)

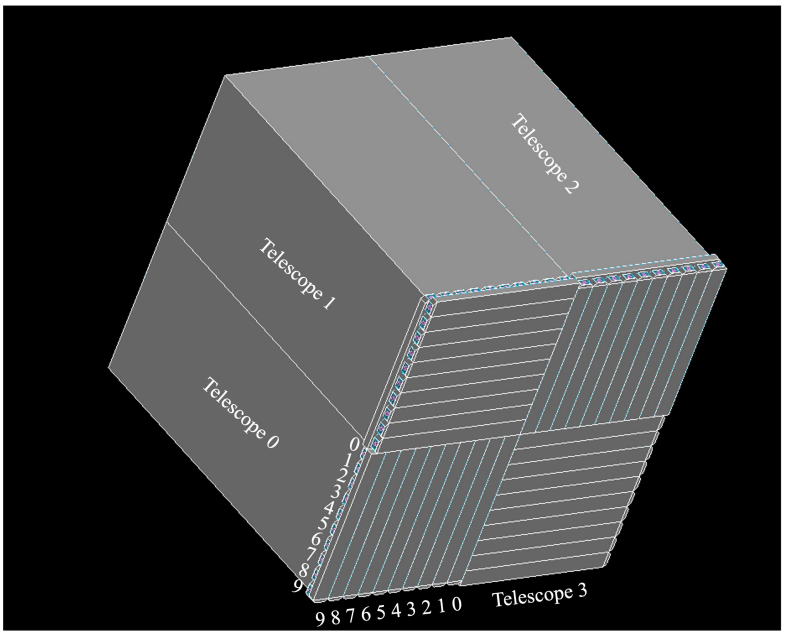


(b)

Figure 2.13: a) One telescope detector. The Figure includes the front and back bar structures and the calorimeter. All of them include the two-layer coat paint. b) Clover: a cluster of 4 telescopes. The local numeration of the bars for the other telescopes follows a rotation on the axis that passes through the center of the clover (where the four telescopes converge).

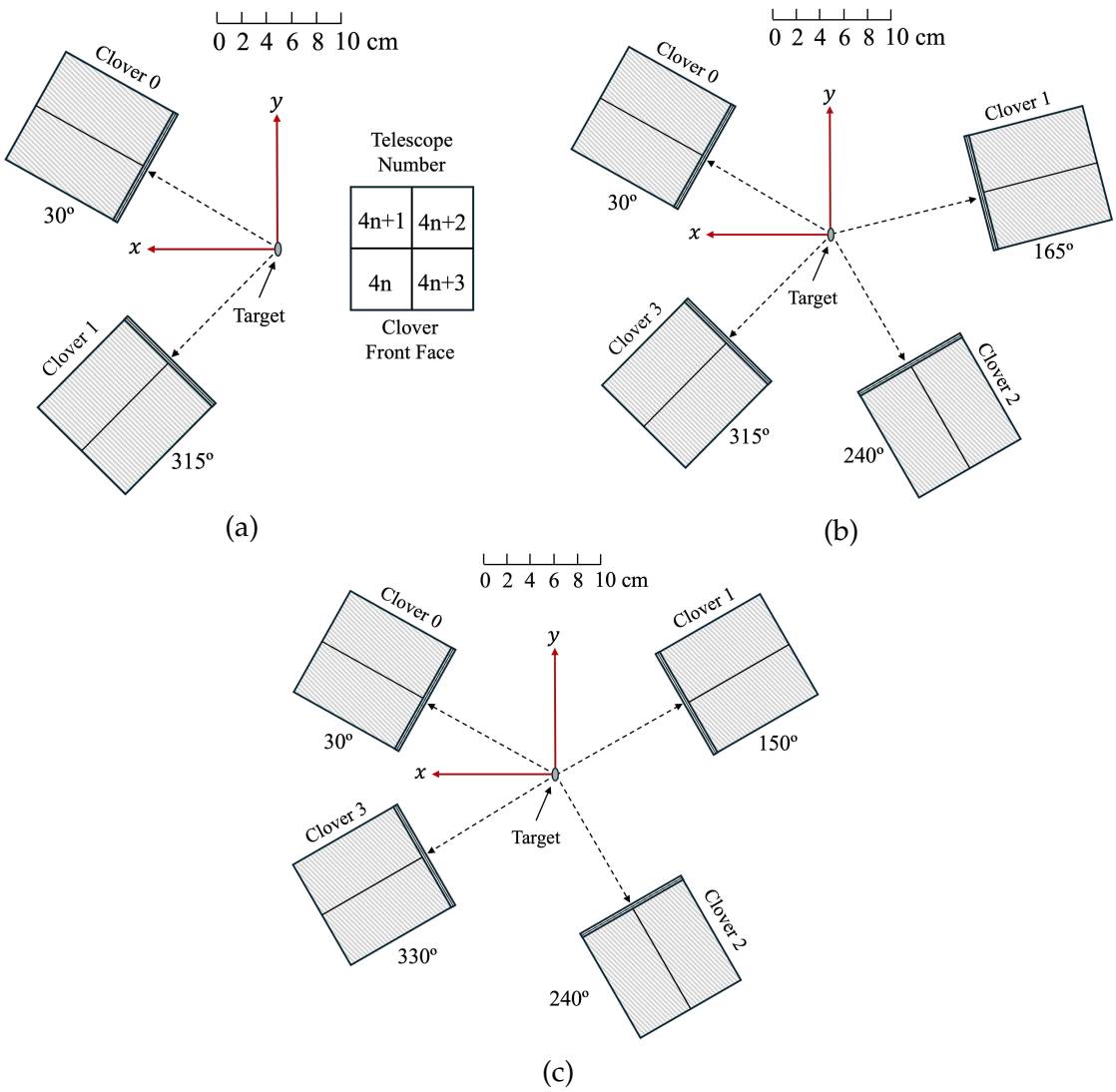


Figure 2.14: Three examples of the $e^+e^-$ pair spectrometer detector array configurations. Those configurations were used during the experiential campaign in the a) commisioning (in the telescope number, "n" corresponds to the clover number), b) first experiment, and b) second experiment.

The reaction chamber, target ladder, detector support structures, and cooling block for the target have been included in the simulation to consider the scattering on those structures as well as the external pair creation (see Figure 2.15).

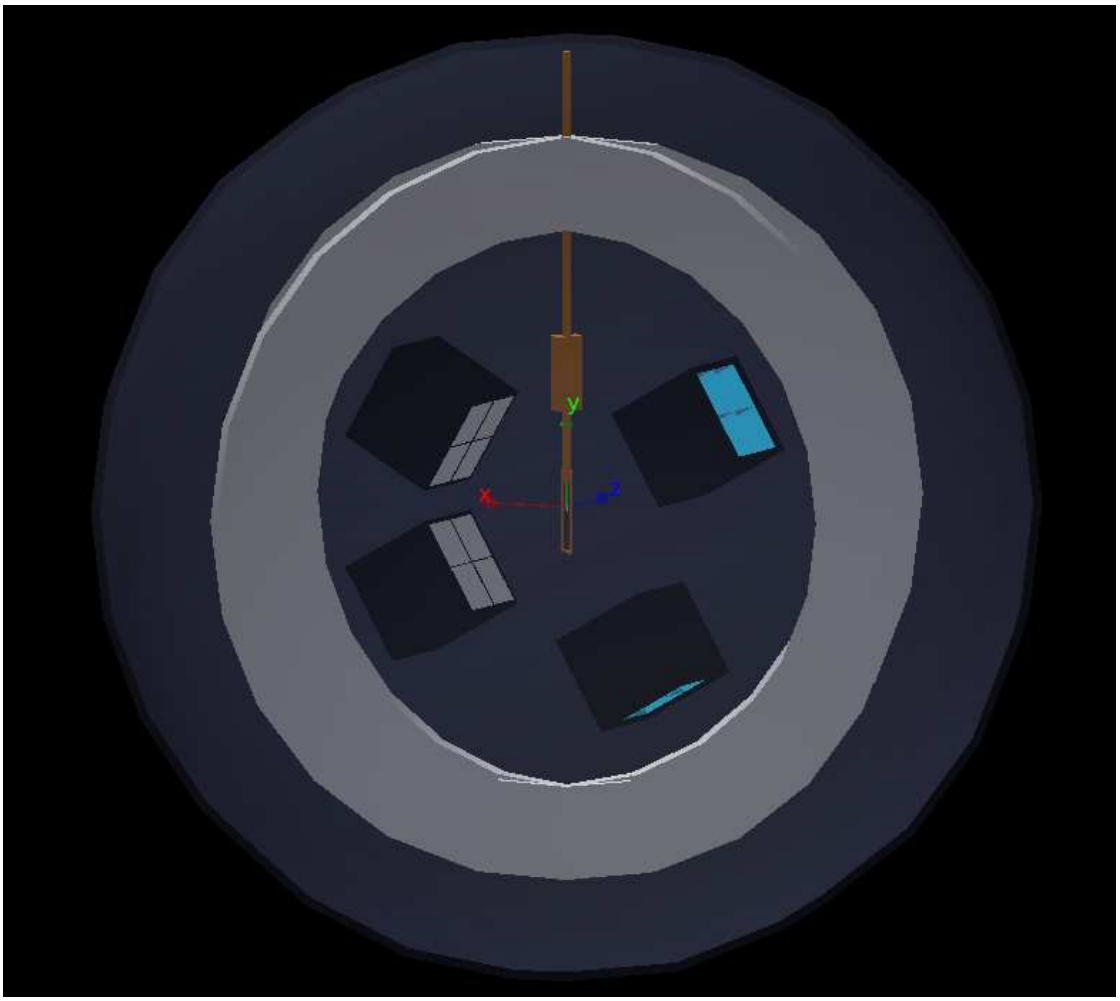

Figure 2.15: Geant4 geometry construction of the complete experimental setup for the configuration shown in Figure 2.14 c).

### Emission Radiation

The $e^+e^-$ pair simulation is divided into two sections: the origin, which is the target construction, and the kinematics.

### Target construction

The target is constructed using a cylinder with an elliptical base. The target dimensions are shown in Figure 2.16, the $x$ corresponds to the major axis, the $y$ the minor axis, and the $t$ the thickness. On the other hand, the backing target is also constructed by using the same geometrical shape. The material used for the target is LiF (named G4_LITHIUM_FLUORIDE in Geant4), and the backing material used is carbon (G4_C) or aluminum (G4_Al). In addition, the target and backing were titled by 45° with respect to the beam direction to avoid shadowing the detectors.

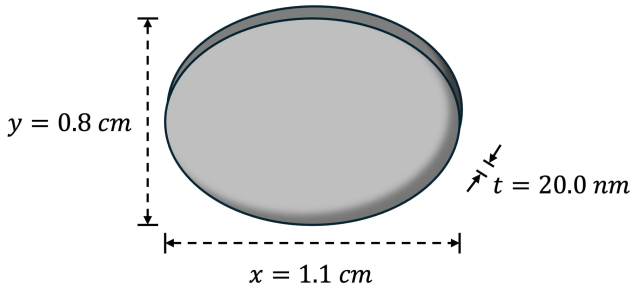


Figure 2.16: Geometry construction of the target and backing.

### $e^+e^-$ Kinematics

The $e^+e^-$ pair emission definition is fundamental because the energy spectra and the position reconstruction depend on it. The energy of the positron and electron depends on the energy of the electromagnetic transition. The energy used to create the pairs must be subtracted to calculate the available energy (see Equation 1.3). The energy of the electron is chosen randomly in a Gaussian distribution centered at half of this available energy and a $\sigma$ of one-eighth of the same value (see top Figure 2.17). The energy of the positron is calculated as the remaining energy; in that way, the sum is equal to the transition energy (see bottom Figure 2.17).

The angular distribution of the $e^+e^-$ emission can be selected between two options: fixed angle (the positron and the electron are shot in a fixed angle)

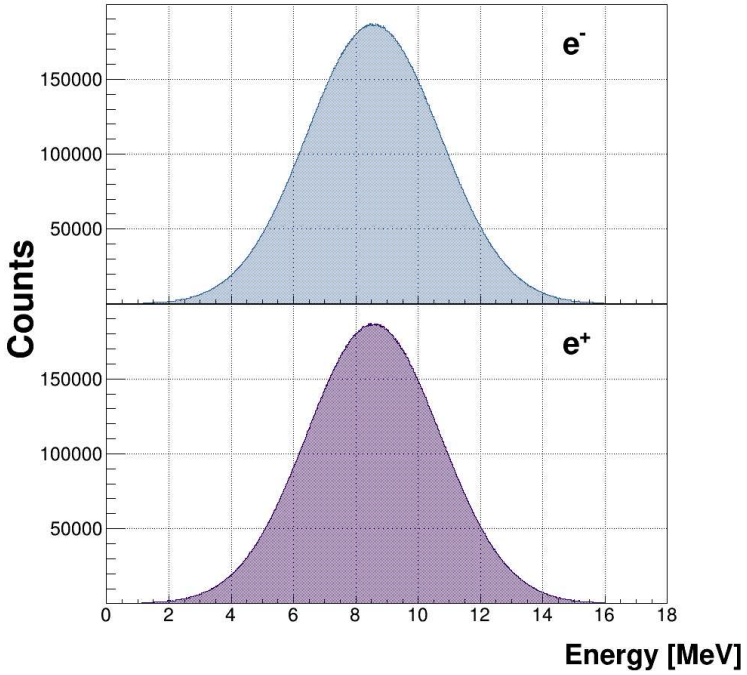


Figure 2.17: Energy distribution for a $e^+e^-$ pair simulated from a 18.13 MeV transition.

and uncorrelated pairs (based on a sinusoidal distribution on the polar angle between the pair; see Figure 2.18).

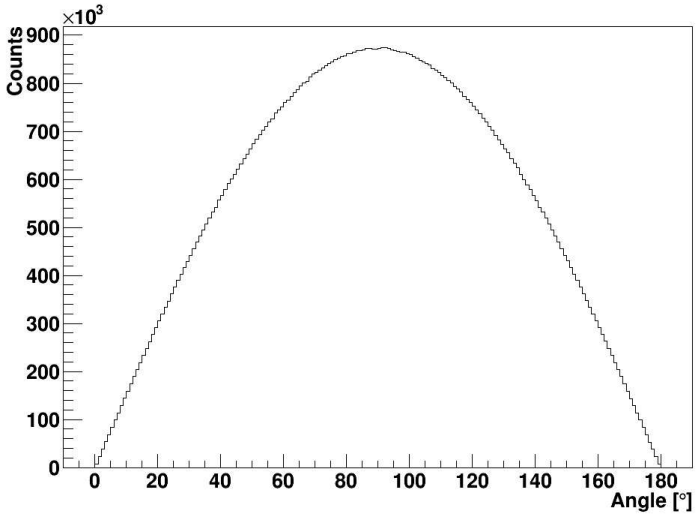


Figure 2.18: Simulated Angular correlation distribution of $e^+e^-$ uncorrelated.

### 2.2.2 Simulation Ouput

The simulation output is an idealized data set to better understand the experimental setup. The analysis is divided into two parts: the transition energy reconstruction and the determination of the relative angle. This analysis is based on the fact that a $e^+$ or $e^-$ that gives valuable information is the one that passes through the three layers of a telescope. The expected experimental outputs will be discussed in the following subsections.

#### Deposited Energy

#### Bars

The $e^+$ or the $e^-$ entering a telescope can deposit energy in the two sublayers of the ΔE-layer according to the length of the path. Unlike heavy ions, the lepton does not follow the Bethe-Bloch equation, making it more difficult to identify them through energy deposition analysis. Still, the coincidence between the $\Delta E$ and $E$ parts of the detector can be used to discriminate between $e^+$ or $e^-$, and $\gamma$-rays. Figure 2.19 shows the energy deposited in the a) front layer and b) back layer for IPC at 17.6 MeV transition. In the two cases, two peak structures can be appreciated. The two peaks refer to events releasing the energy only in the scintillator volume (high-energy peak) or partly in the optical fibers (lower-energy peak). The tail has two components: bremsstrahlung radiation and the tortuous path of the $e^+e^-$ inside the detector (the longer the path length, the higher the deposited energy is).

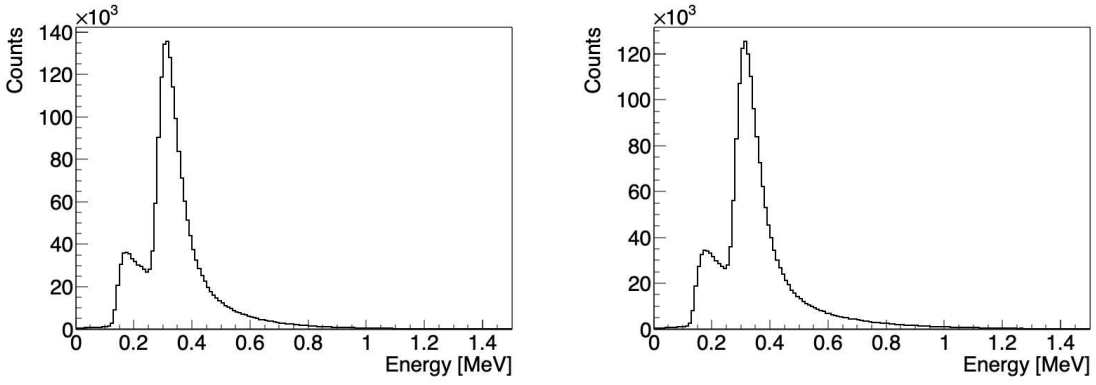


(a) (b)

Figure 2.19: Deposited energy in (a) the front and (b) back layers of the $\Delta E$-layer, for $e^+e-$ pairs from an IPC process at 17.6 MeV.

A detailed analysis can be performed if the deposited energy is plotted as a function of the length path inside a bar. Figure 2.20 shows graphically the accumulation of counts in the region close to the bar thickness and an intermediate area between the fiber and bar thickness. In Figure 2.20 a), the accumulation is shifted a few millimeters with respect to Figure 2.20 b) due to the different entrance angles in the telescope. While in Bar 0, the incidence angle is near 0°, in Bar 9, the incidence angle is ≈20°, which means that the path is longer and more energy is deposited.

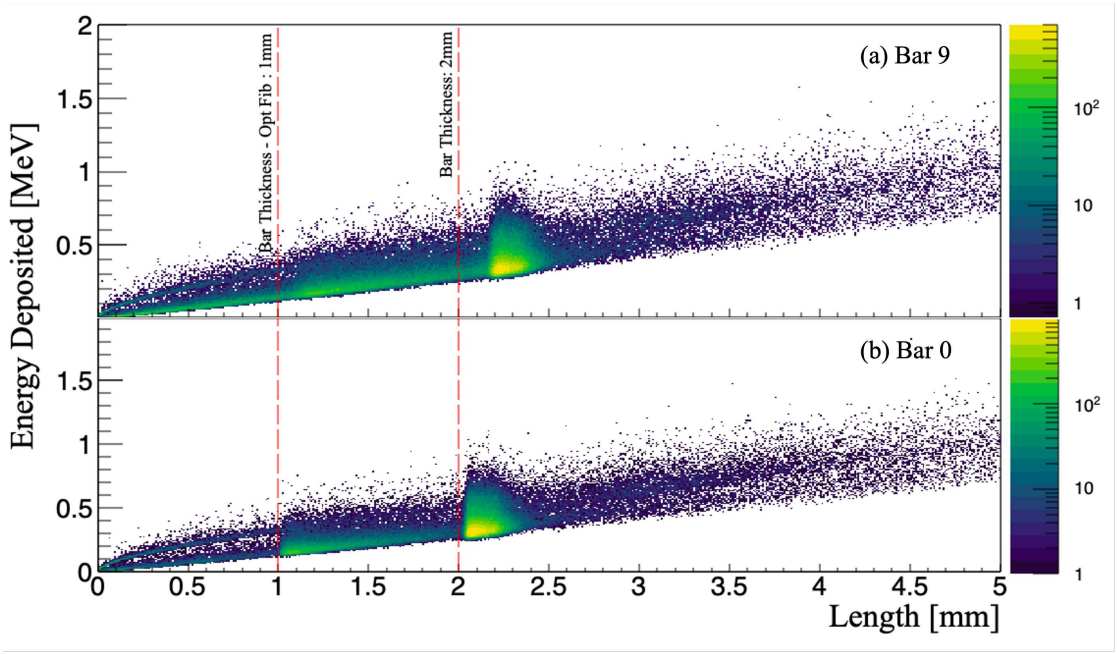


Figure 2.20: Comparison of the length and deposited energy between (a) a bar close to the center of the clover and (b) a bar far from the center, for $e^+e-$ pairs from an IPC process at 17.6 MeV.

The energy deposited by leptons with the straightest path can be determined by applying a gate in the areas close to the bar thickness in Figures 2.20 a) and b). The narrower the gate, the straighter the path is. However, the events where the electron or positron loses energy due to bremsstrahlung radiation emission will be rejected even if they go straight inside the material. For this reason, the tail at the right in the energy spectra of Figure 2.21 a) can be included in the analysis.

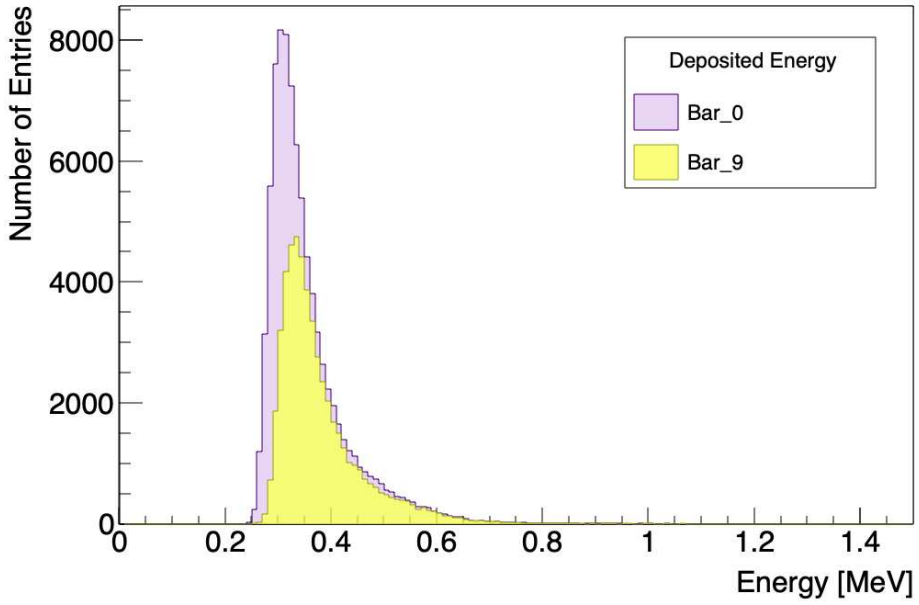


(a)

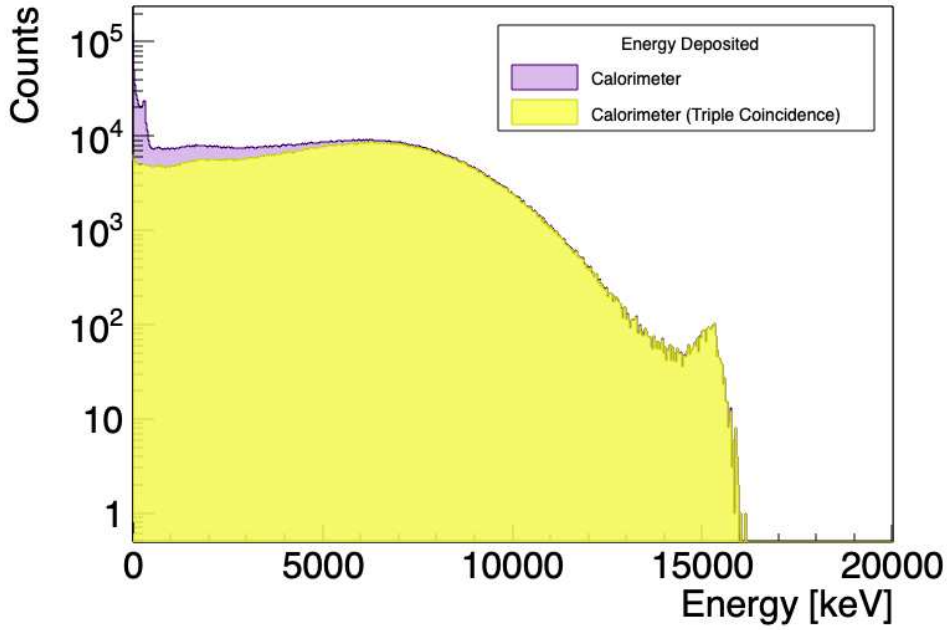


(b)

Figure 2.21: a) Deposited energy in a bar close to the center of the clover (Bar 0, in purple) and a bar far from the center (Bar 9, in yellow), for $e^+e-$ pairs from an IPC process at 17.6 MeV. b) Deposited energy in the calorimeter layer of the telescope, for $e^+e^-$ pairs from an IPC process at 17.6 MeV.

### Calorimeter

The size of the calorimeter is enough to stop the ≈ 18 MeV $e^+$ or $e^-$ (traveling along its longest axis) since they lose about 2 MeV/cm. Figure 2.21 b) shows that the maximum deposited energy in the calorimeter is around 16 MeV, corresponding to the maximum energy available for one of the leptons once it passes through the scintillator bars. The purple spectrum shows the deposited energy in the calorimeter with no condition; meanwhile, the yellow one is the energy deposited in the calorimeter in coincidence with the ΔE-layer. The rejected events occur when the annihilation $\gamma$-ray arrives in the calorimeter without interaction with the bars (low energy peak of the purple spectrum in Figure 2.21 b)) or scattered leptons from other structures that hit only the calorimeter (main discrepancy between the yellow and purple spectra in the 0.5 - 8.0 MeV region in Figure 2.21 b)). They are not helpful in the analysis, and the triple coincidence ($\Delta E_{Front} - \Delta E_{Back} - E_{Calorimeter}$) helps us to avoid them and calculate a wrong correlation between the $e^+e^-$ pair. The wide edge around 8 MeV is the average energy shared between the two leptons, and the peak at the highest energy is the events where the two entered one single telescope.

### Transition Energy Reconstruction

The reconstruction of the transition energy starts with the data selection of the events where two telescopes were in coincidence. The bar and calorimeter energy analysis showed that a gate up to 0.6 MeV in the energy deposited in every sub-layer of the ΔE-layer and the coincidence with the calorimeter filters the events related to the $e^+$ or $e^-$, with straight paths. Continuing with the analysis, the ΔE-E matrix (see Figure 2.22) exhibits only two distinguishable areas. The first one is the brightest line around $\Delta E \approx 0.5$ MeV, which corresponds to the sum of energy of the peaks of the back and front energy spectra. The area in the $E > 16$ MeV region mainly corresponds to the pairs entering the same telescope; in this case, we cannot calculate the relative angle because the signals in the $\Delta E$ matrix will be overlapped. The $\Delta E - E$ correlation matrix cannot be used for the analysis because positrons or electrons do not create structures in this matrix like in the case of heavier ones (for example, $p$, $^4He$,$^{12}$C).

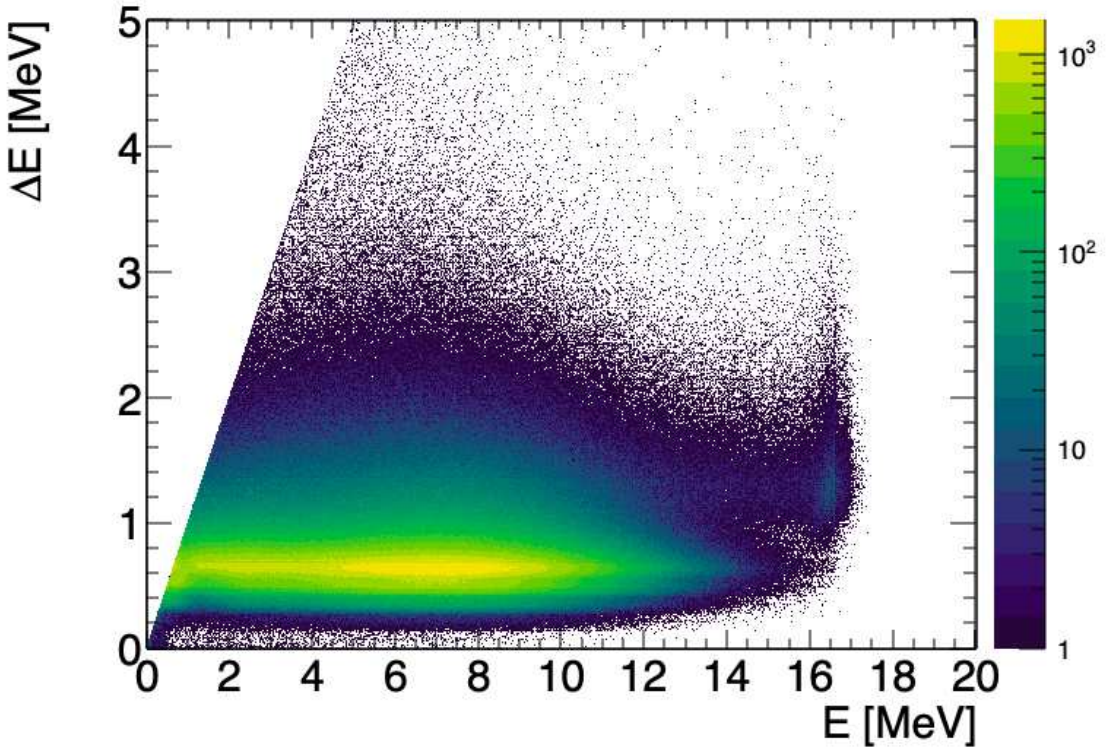


Figure 2.22: $\Delta E - E$ matrix of the $e^+/e^-$ in the telescope detectors.

When the $e^-e^+$ pair hits two telescopes, a correlation energy arises from the energy deposited. Because the deposited energy is coming from a well-defined energy (energy of the electromagnetic transition), we expect to see a limit in the deposited energy of a calorimeter once we know the value deposited in the other. This is reflected in an anti-diagonal, like the ones shown in Figure 2.23. The sum of the deposited energy in every telescope in that region is close to the available energy of the electromagnetic transition after creating the pairs. Thus, this structure is one of the first indications we can expect to see in the study of pair creation. All the events below the anti-diagonal are due to the leptons escaping from the calorimeter before entirely depositing their energy or bremsstrahlung radiation that scapes. This effect is called the *wall effect* and depends on the size of the detector. Unfortunately, those events cannot be used in the analysis and will interfere with the reconstruction of the transition energy. The bright side is that with more than one transition (one at 17.6 MeV and one at 6.05 MeV, for example), the one with the highest energy does not contain events of the other when gating on the antidiagonal region.

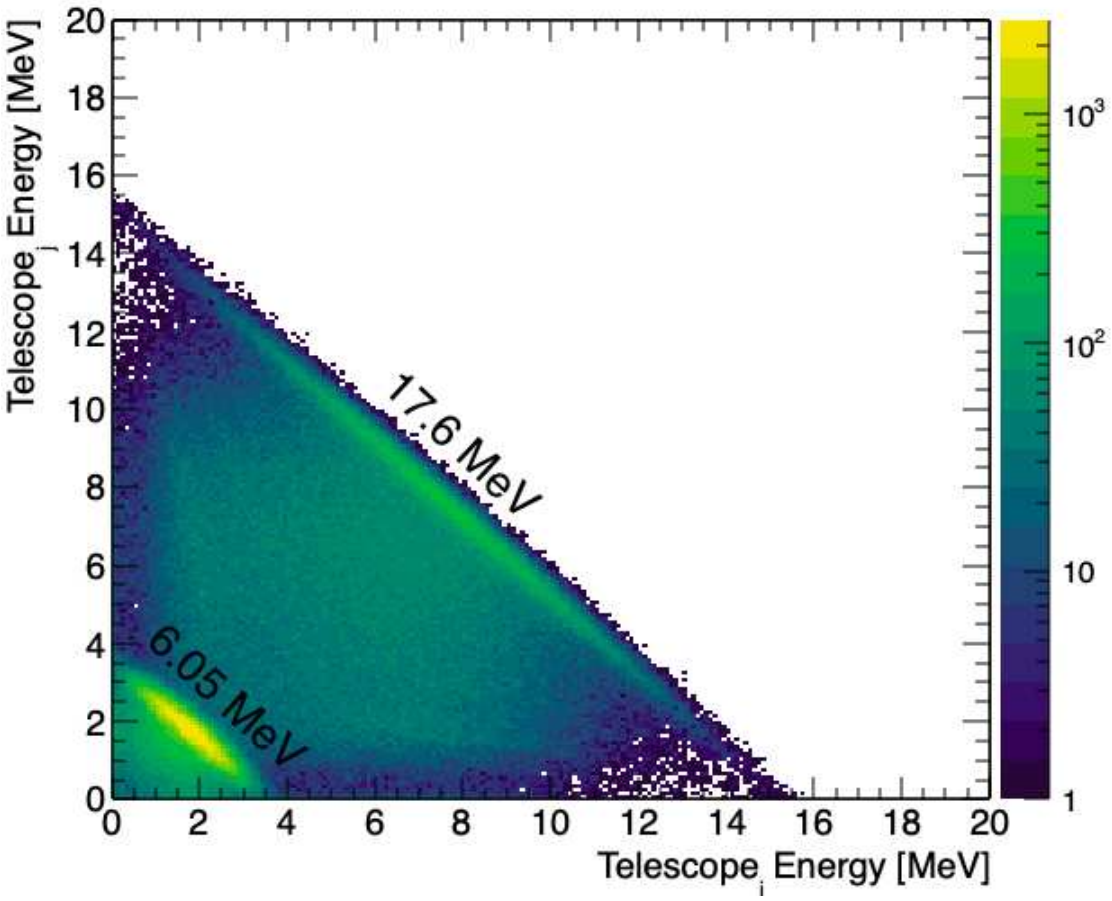


Figure 2.23: Calorimeter correlation energy of two telescopes fired in coincidence. The anti-diagonal lines represent a constant sum energy of the two calorimeters. In this case, two electromagnetic transitions of 6.05 MeV and 17.6 MeV were simualted

According to A.J. Krasznahorkay [5], another useful parameter is the energy asymmetry $y$, defined as:

$$y = \frac{E_i - E_j}{E_i + E_j} \tag{2.4}$$

Where $E_i$ is the deposited energy in the i-th calorimeter and $E_j$ in the j-th calorimeter. Figure 2.24 shows the sum energy of two telescopes in coincidence as a function of the asymmetry parameter $y$. This matrix shows that most events are emitted close to the symmetric region when the sum of the energy is maximum (closest to the transition energy). So, a restriction in the asymmetry parameter can filter events where the wall effect is present, but it is not so

effective in that it does not improve the transition energy resolution notably. In this analysis, the range selected is $y \leq |0.75|$.

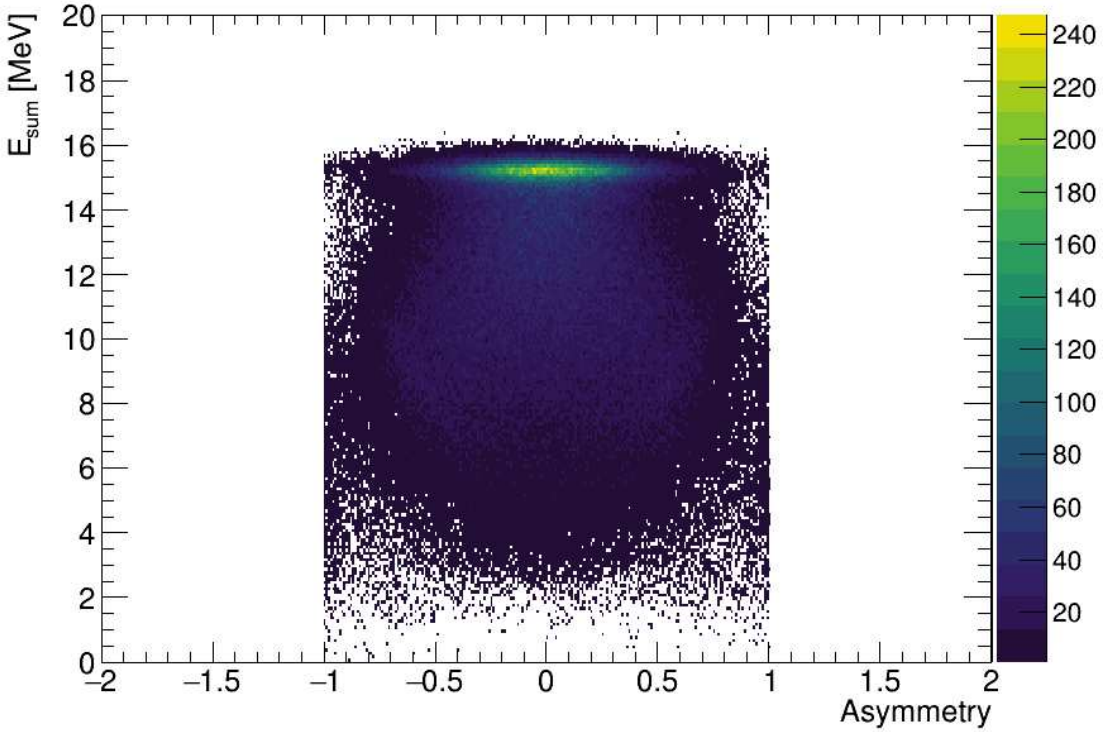


Figure 2.24: Sum energy of the calorimeters fired in coincidence as a function of the asymmetry parameter defined in Equation 2.4.

The advantage of having cluster detectors is that we can use the add-back technique. Once a $e^+e^-$ entered in a clover, either the $e^+e^-$ itself, the X-rays from the bremsstrahlung effect, or the $\gamma$-rays (from the $e^+$ annihilation) can hit a near calorimeter in the same clover, different from the one that the $e^+$ or the $e^-$ hit at the beginning. In such cases, the sum of the deposited energy in the complete clover will be more precise than the one where only the energy in one calorimeter was considered. Figure 2.25 shows the effect of applying the add-back in the reconstruction energy of the pairs, where some events in the orange spectrum are pushed to the high-energy peak, recovering around 15% of the events.

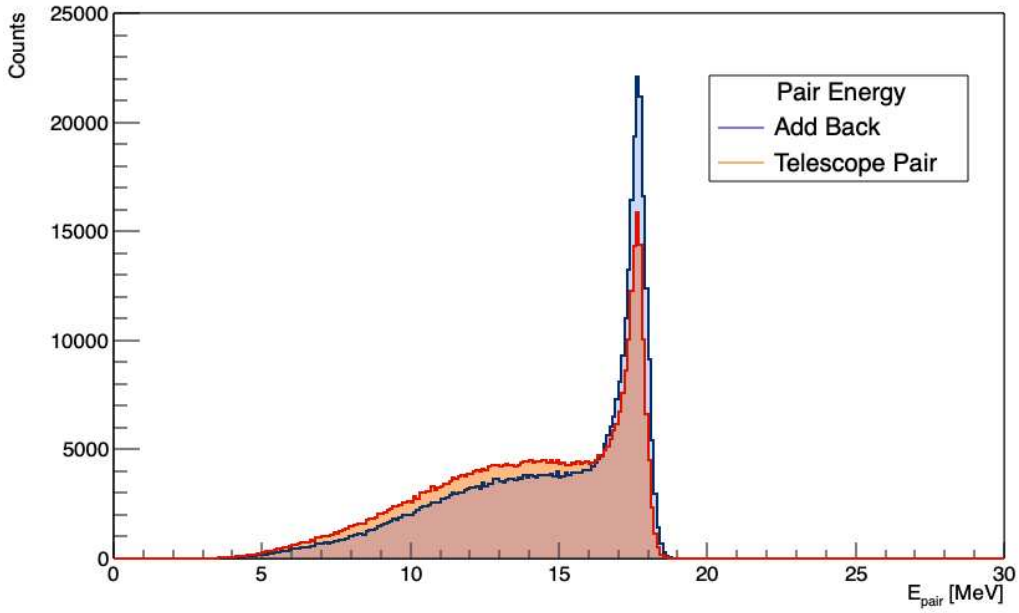


Figure 2.25: Reconstruction energy of the $e^+e^-$ pair by (orange) summing the deposited energy of two telescopes where the pair arrived, and (blue. add-back) summing the deposited energy of the two clovers where the pair arrived.

### Position Reconstruction

Figure 2.26 a) and b) show the position spectra for the back and front bars, respectively. Well-separated structures can be seen for every bar fired. The energy shared between bars does not produce appreciable interferences in the position determination. The reconstruction of the position interaction in the clover is shown in Figure 2.27, where every Lego bar corresponds to one front and back bar intersection pixel. As expected, the most efficient part for a random pair emission distribution is the center of the clover because there is more scintillator material where the $e^+e^-$ pairs can deposit their energy than in the borders.

One basic test of the position reconstruction method is shooting a $e^-$ with a random direction and a $e^+$ at a fixed angle with respect to the $e^-$ one (in a random plane). If the angle selected is inside the angular coverage, the shape of the reconstructed correlation angle is not catastrophically affected by the efficiency. This can help us to prove that the array can measure precise correlation angles and calculate the angular resolution. For this simulation, the detector configuration of Figure 2.14 c) has been used. Figure 2.28 shows the reconstructed angular correlation distribution of the random emission discussed before. The

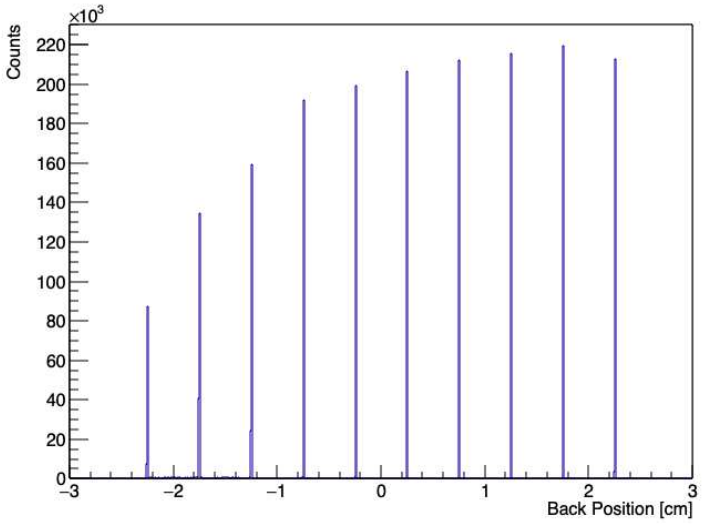


(a)

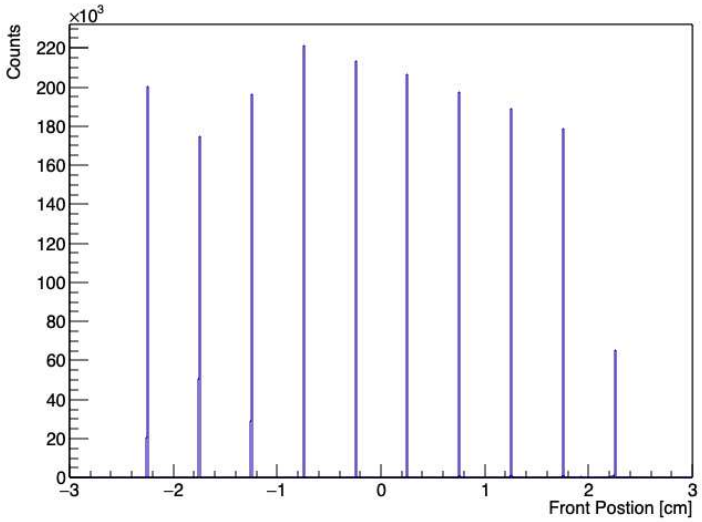


(b)

Figure 2.26: Reconstructed $e^+/e^-$ incidence position in (a) the back and, (b) front sublayer of the $\Delta E$ layer of one telescope.

peak of the spectrum is centered at 90°±0.03° with a FWHM of 2.52°±0.02°, which is the angle of the simulated $e^+e^-$ pair. The final step of the analysis is the computation of the efficiency for different detector array configurations, which will be discussed in the next section.

Figure 2.29 shows the response of the detector array for $e^+e^-$ pairs emitted in a) a $E0$ transition, b) a $M1$ transition, and c) the decay of a 17 MeV/c$^2$ mass boson. The $e^+e^-$ pair spectrometer shows different distributions according to

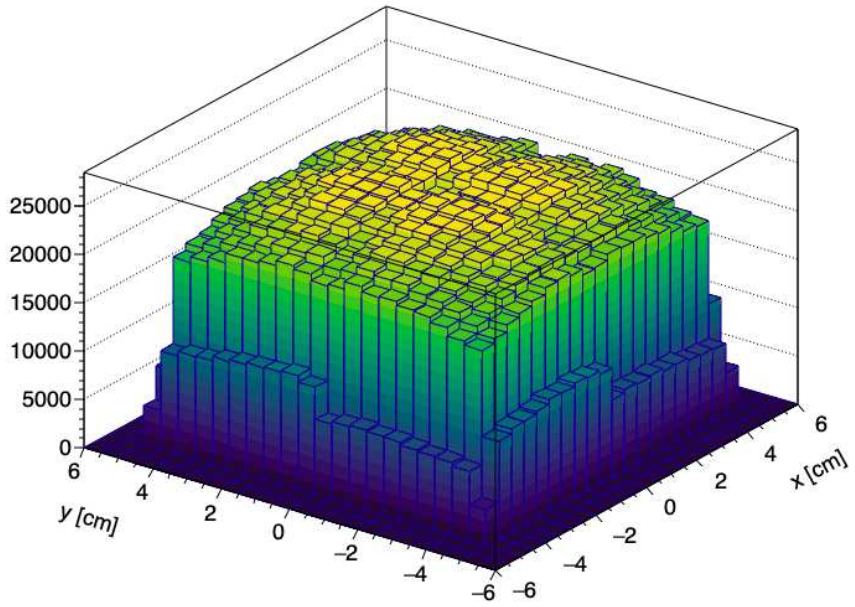


Figure 2.27: Reconstructed $e^+/e^-$ incidence position in one clover detector.

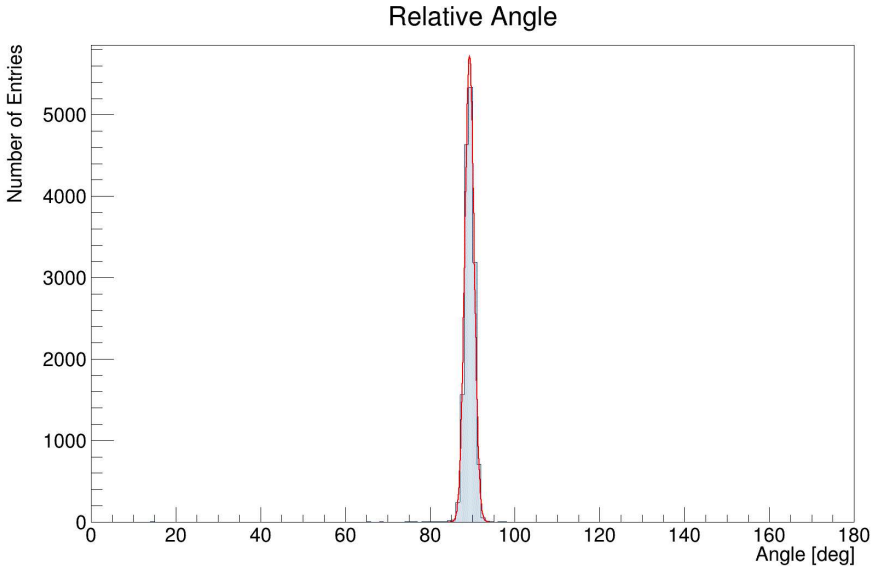


Figure 2.28: Reconstructed angular distribution of a $e^+e^-$ pair with a 90° relative angle emission in different planes.

the type of transition as expected (the model of Rose has been used for the emission of the $e^+e^-$ pairs). On the other hand, the decay of a 17 MeV/c$^2$ mass boson can be observed as a peak structure $\approx 140°$, similar to the result reported by the Hungarian group [5]. In conclusion, the simulation shows that the $e^+e^-$

pair spectrometer is sensible to different types of electromagnetic transitions, as well as the decay of a particle with a mass of 17 MeV/c$^2$.

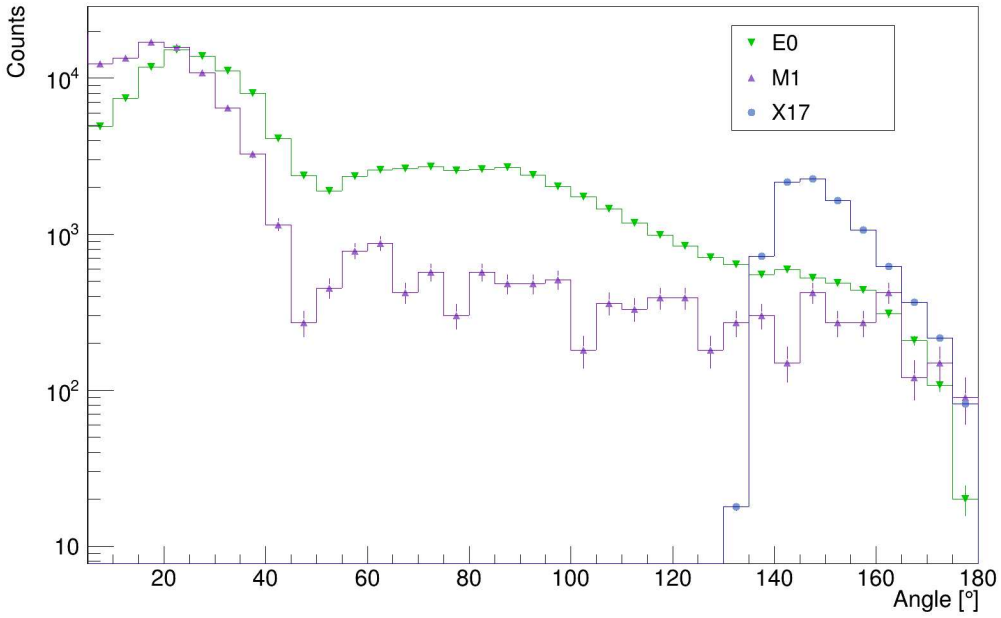


Figure 2.29: Response of the detector array for $e^+e^-$ pairs emmited in a) a $E0$ transition, b) a $M1$ transition, and c) the decay of a 17 MeV/c$^2$ mass boson. The electromagnetic distributions were calculated using the model of Rose.

## 2.3 Efficiency Estimation

The simulation can be used to compute the efficiency of the setup for different configurations. Figure 2.30 shows the angular efficiency for the detector arrays shown in Figure 2.14 for uncorrelated $e^+e^-$ pair emission at the corresponding energies of the electromagnetic transitions in $^{16}$O ($0_2^+ \rightarrow 0_1^+$) and $^8$Be ($1_2^+ \rightarrow 0_1^+$ and $1_1^+ \rightarrow 0_1^+$). Conf 1 (Figure 2.30 a)) contains two structures due to the correlation angle detected in the same clover (0° - 40° region), and the second one is the correlation angle in two different clovers (40° - 110° region). Conf 2 (Figure 2.30 b)), in addition to the structures of Figure 2.30 a), contains a third structure peaked at 150° due to the correlation angle between the two largest angles possible to detect. This angle value is close to the angle of the anomaly found at Atomki [5]. The last configuration, Conf 3 (Figure 2.30 c)), was thought to avoid drastic holes in the angular efficiency, even though only four

detectors were used (the maximum number of detectors for this experimental campaign). The high efficiency at large angles (> 140°) benefits the angular correlation determination since the probabilities for the $E0$ and $M1$ transitions are very small at those angles (see Figure 1.2).

Table 2.4 contains the total efficiency detection for the detector array configurations shown in Figure 2.30. As expected, the efficiency increases with the number of detectors and decreases with the $e^+e^-$ energy. The efficiency value for the $1_2^+ \rightarrow 0_1^+$ transition in $^8$Be is roughly half of the value reported by A. Krasznahorkay et al. [5], so the setup is a good candidate to measure the angular distribution of the $e^+e^-$ pair correlation by a longer measurement that the one performed in [5].

Table 2.4: Efficiency estimation for three different array configurations.

| **Electromagnetic Transition** | **Energy [MeV]** | **Efficiency [%]** | | |
|---|---|---|---|---|
| | | Conf 1 | Conf 2 | Conf 3 |
| $^{16}O : 0_2^+ \rightarrow 0_1^+$ | 6.048 | 0.22 | 0.71 | 0.67 |
| $^8Be : 1_1^+ \rightarrow 0_1^+$ | 17.62 | 0.14 | 0.45 | 0.42 |
| $^8Be : 1_2^+ \rightarrow 0_1^+$ | 18.13 | 0.14 | 0.44 | 0.41 |

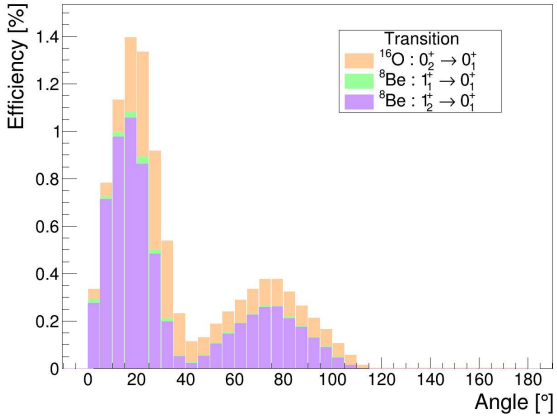


(a)

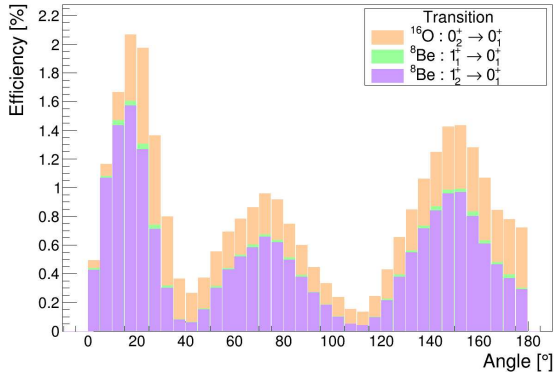


(b)

Efficiency

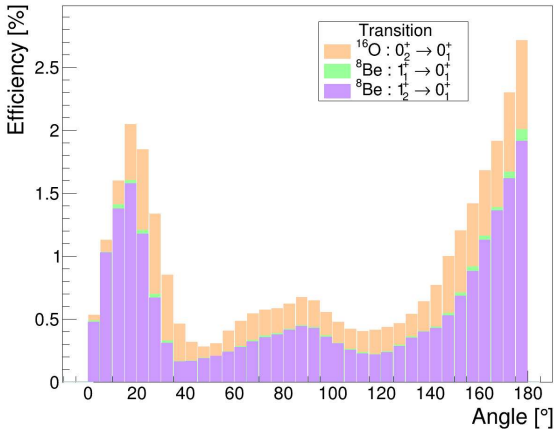


(c)

Figure 2.30: Angular efficiency of the correlation angle of the detector array configurations: a) Conf 1, b) Conf 2, and c) Conf 3 shown in Figure 2.14.

# 3

# Characterization of the $e^+e^-$ Pair Spectrometer

*The present chapter describes in detail the characterization experiments of the $e^+e^-$ pair spectrometer components, where the energy and position capabilities of the detectors were tested for the first time.*

## 3.1 The Energy Measurement

The first experimental test about the correct functioning of the energy measurement of the detector was performed with cosmic muons. Considering the high energy of the muons (~4 GeV on average), the energy deposited in one detector depends mainly on the effective thickness of the scintillator seen by the muon. A trigger detector was placed to prioritize the normal angles to one face of the calorimeter and then select a deposited energy range. The configurations chosen are shown in Figure 3.1 (left), where the trigger detector is a 0.5×4.0×7.0 cm EJ-200 scintillator coupled to a PMT at 32 cm distance from the calorimeter. The acquisition was carried out by using a CAEN 1730 digitizer [30] (16CH, 14BIT, 500MS/s, 2Vpp, DPP-PSD) and the CoMPASS software [31] with a time-coincidence window of 1 $\mu$s between the trigger detector and the calorimeter. The experiment aimed to check if the energy deposited in the calorimeter block in a horizontal configuration was half the one deposited in a

vertical configuration. The expected behavior is that the leptons travel approximately double the distance inside the detector in the vertical configuration, on average. The effect has been corroborated, as the energy spectra of Figures 3.1 a) and 3.1 b) show. For the first configuration (Figure 3.1 a), a peak structure in the energy spectrum was observed at channel 604.40 ± 2.32, while for the second (Figure 3.1 b), at channel 1222.32 ± 7.04. Thus, the energy deposited in the configuration of Figure 3.1 b) is approximately twice the energy deposited in Figure Figure 3.1 a), as expected. Geant4 simulations have been performed to estimate the energy deposited in the detector in the two configurations (8.99 MeV and 18.5 MeV, respectively). Those values were used to perform a 2-point calibration of the calorimeter. This result means that one single calorimeter can measure energies close to 20 MeV. The tail observed at the right of the peak in the spectra is because the muons can enter with different angles. Then, the effective path could be longer than if they enter normal to the surface, or/and the muons can be scattered inside the scintillator or/and the bremsstrahlung radiation can be absorbed in the scintillator.

The path of the $e^+e^-$ of the IPC is not as straight as in the case of the muons because their energy is orders of magnitude lower (~2-3), and this behavior has to be considered in the design of the detector. To increase the probability of measuring the complete energy of $e^+e^-$ that did not follow straight lines, an increase of the detection volume is needed. This can be achieved by assembling four calorimeters in a square configuration of $2 \times 2$. Unfortunately, the $e^+e^-$ scattering out of the detector (wall effect) cannot be rejected from the acquisition since there is no veto detector. The treatment performed to decrease this effect is discussed in Chapter 5.

## 3.2 The Position Measurement.

An experiment was performed to determine the position interaction, an $\alpha$ source was used for this purpose. The paint of one bar was scratched at the center of its face to avoid the energy loss of the ion before reaching the scintillator material. The front face of the telescope was covered by an aluminum foil with a hole of 3 mm diameter, as Figure 3.2 shows. In this configuration, the $\alpha$ particles can only hit one bar where the paint was removed. The $^{241}$Am $\alpha$ source and the telescope were placed in a vacuum chamber since the low temperature generates condensation and the water can damage the electrical circuits. The

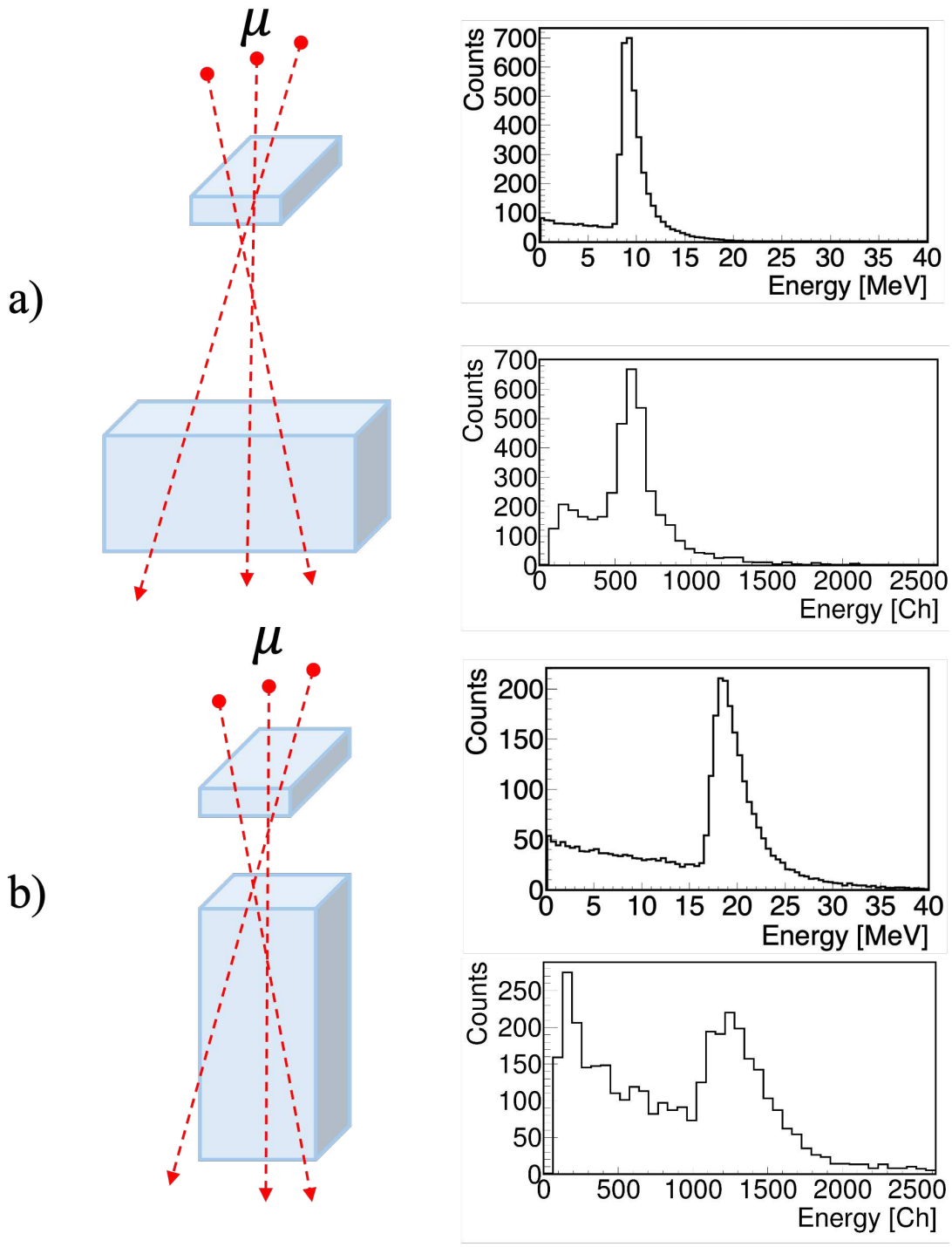


Figure 3.1: Comparison between the two calorimeter configurations with respect to a trigger detector above: a) horizontal configuration and b) vertical configuration.

DAQ system used was the same as in the muon test, including a similar time

window coincidence for every pair of channels. The low-voltage and high-voltage power supplies were the same, too, but the high-voltage was set to 35 V. Every bar position has been irradiated separately for 5 hours. The detection of cosmic muons has been decreased by setting a gate in the energy deposited in the layer calculated with Equation 2.2. The top spectrum in Figure 3.3 corresponds to the energy deposited by the $\alpha$ particles (not visible without the source), and the range selected was from 248 to 568 digitizer channels (red box). The position interaction was determined using Equation 2.3. As the bottom plot of Figure 3.3 shows, only one peak is observed and indicates that the system can detect which bar has been fired by the $\alpha$ particles. Continuing the test, the other bars were scanned using the abovementioned methodology. The result can be seen in Figure 3.4; every peak corresponds to one bar irradiated, and a different color was set for clarifying purposes. In addition, a position calibration was performed to place the peak centroid at the center of the bar irradiated. The scintillator bars coupled to the SiPM board have a position resolution that depends on the size of the bar and not on the width of the peak in the plot. The width of the peak depends on the attachment of the scintillator bar to the SiPM because it can be slightly modified when assembling and mounting the detector.

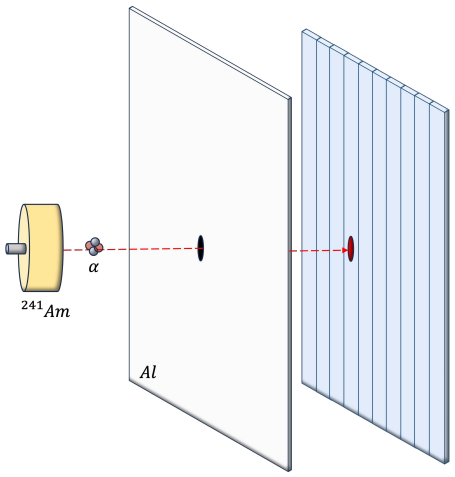


Figure 3.2: Setup of the irradiation of one bar by an $^{241}$Am $\alpha$ source.

As a final test, an electron measurement has been carried out. A $^{90}$Sr/$^{90}$Y source was placed in front of the telescope, and the aluminum foil in the middle at a specific position to shine only one bar in each sub-layer of the telescope. The matrix in Figure 3.5 shows the maximum number of counts in one pixel with the condition of 100 ns time coincidence between the two layers. The

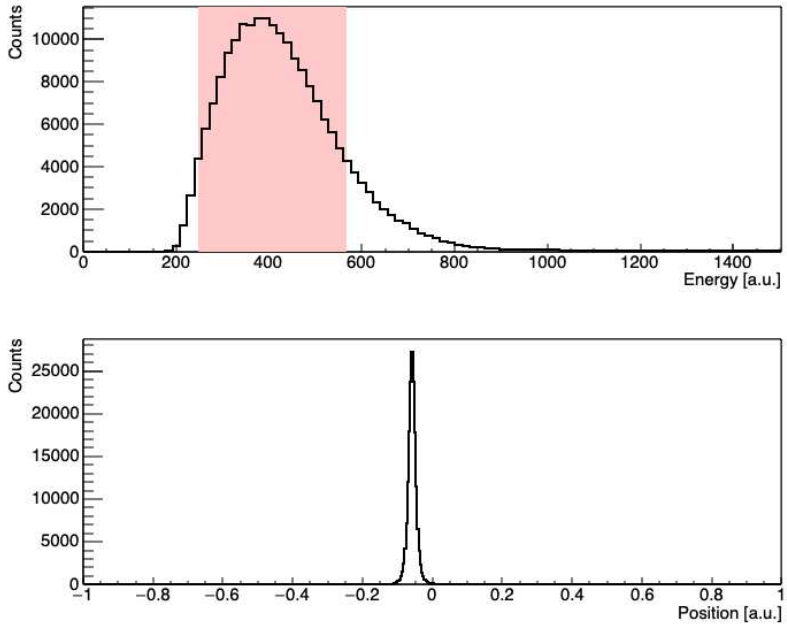


Figure 3.3: Energy (top) and position spectrum (bottom) measured by the front bars irradiated by an $^{241}$Am $\alpha$ source. Notice that in the position plot, only one peak appears, indicating that the cross-talk among the bars is almost nonexistent.

projections of the matrix are shown on top and at the right of the figure. The x-axis corresponds to the front bars layer and the y-axis to the back bars layers. The counts out of the most prominent peaks are associated either with cosmic rays or with light sharing of the SiPMs. These results demonstrated that the set of bars of the telescope can determine the position where an ion enters with the precision of the $0.5 \times 0.5$ cm pixel created by the coincidence of the bar fired in front and back.

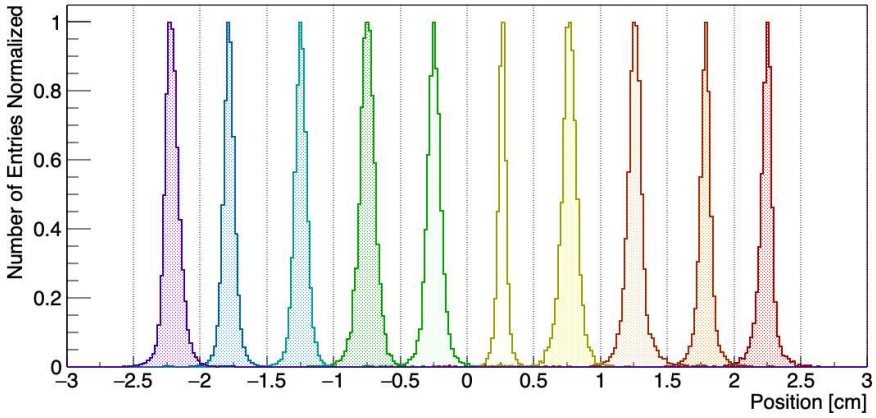


Figure 3.4: Position measurements of independent irradiation of the ten bars by an $^{241}$Am $\alpha$ source. The position of the source was changed to irradiate only one bar per run (represented by different colors).

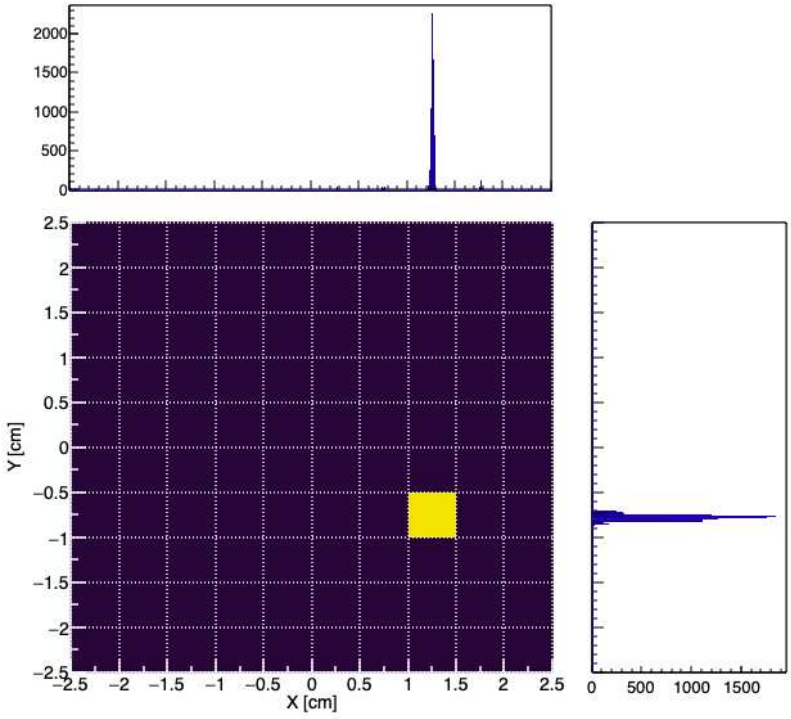


Figure 3.5: Matrix position measured by a $^{90}$Sr/$^{90}$Y electron source.

# 4

# Experimental Campaign

*The present chapter reports on the experimental campaign performed with the previously described $e^+e^-$ pair spectrometer in 2023 and 2024 at the LNL-INFN. The chapter starts by describing the data taking, where the experimental details are discussed, such as the setup configuration, the targets used, the data acquisition (DAQ), and the monitoring system of the experimental parameters. The last part describes the data processing necessary for analysis, including the calibration method.*

## 4.1 Data Collection

The experimental campaign to search for the anomalous IPC in $^8$Be was performed at the AN2000 accelerator [32] of the INFN-LNL. This campaign was approved by the LNL Program Advisory Committee (PAC) and divided into three stages. The *first stage*, which lasted 8 days, consisted of the commissioning of the $e^+e^-$ pair spectrometer. *The second and third stages* consisted of two experiments with different angular covering regions by the detector array to define the best configuration for measuring the angular correlation distribution in the IPC process. These two stages lasted 30 days in total. The time mentioned includes the time spent on the detector mounting and beam preparation.

### 4.1.1 AN2000 Accelerator.

The AN2000 Accelerator (see Figure 4.1 a)) is one of the six accelerators at the LNL-INFN. Its size allows it to be placed in the same hall as the beamlines

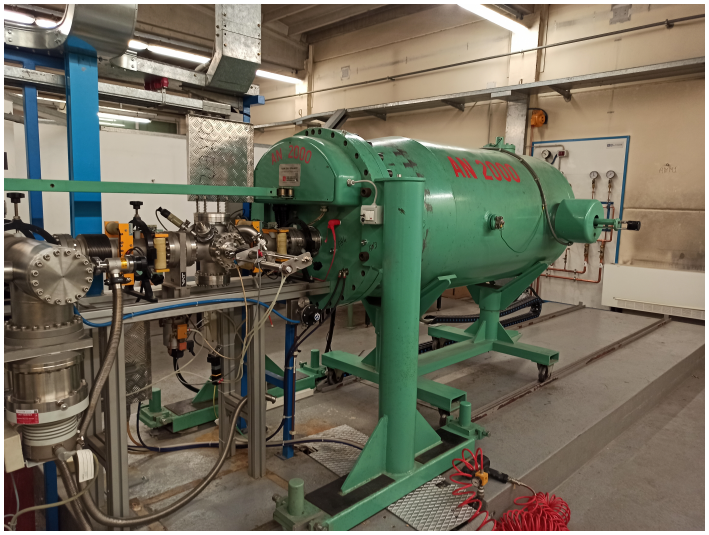

(a)

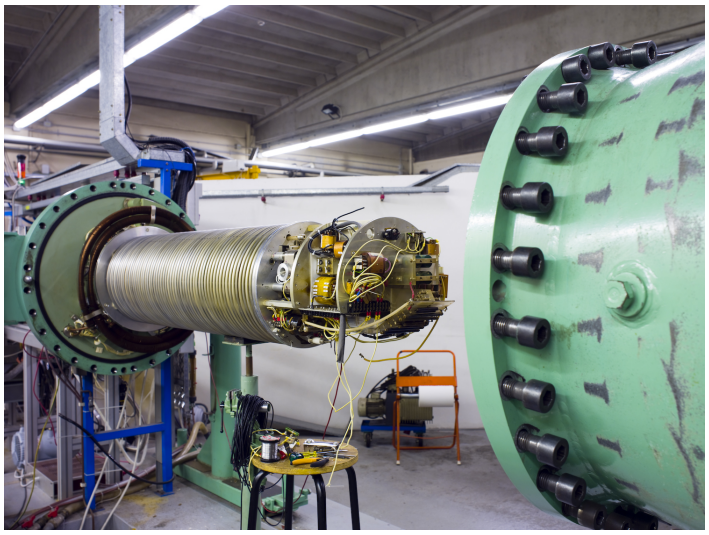

(b)

Figure 4.1: (a) Picture of the AN2000 accelerator tank, and the (b) Van de Graaff generator of the AN2000 accelerator.

for the different experiments. An electrostatic system accelerates the ions (see Figure 4.1 b)) with a maximum voltage of 2 MV. It can provide proton and helium beams with intensities of hundreds of nA. Currently, this machine is used for material analysis, dosimetry applications, and astrophysics research. In our case, the characteristics of the accelerator match with the requirements for the IPC studies in $^{16}$O and $^{8}$Be since it can provide a proton beam and energies between 0.4-1.1 MeV and intensities up to $\approx$ 800 nA. These performances are analogous to the case of the experiment performed at Atomki laboratories [5].

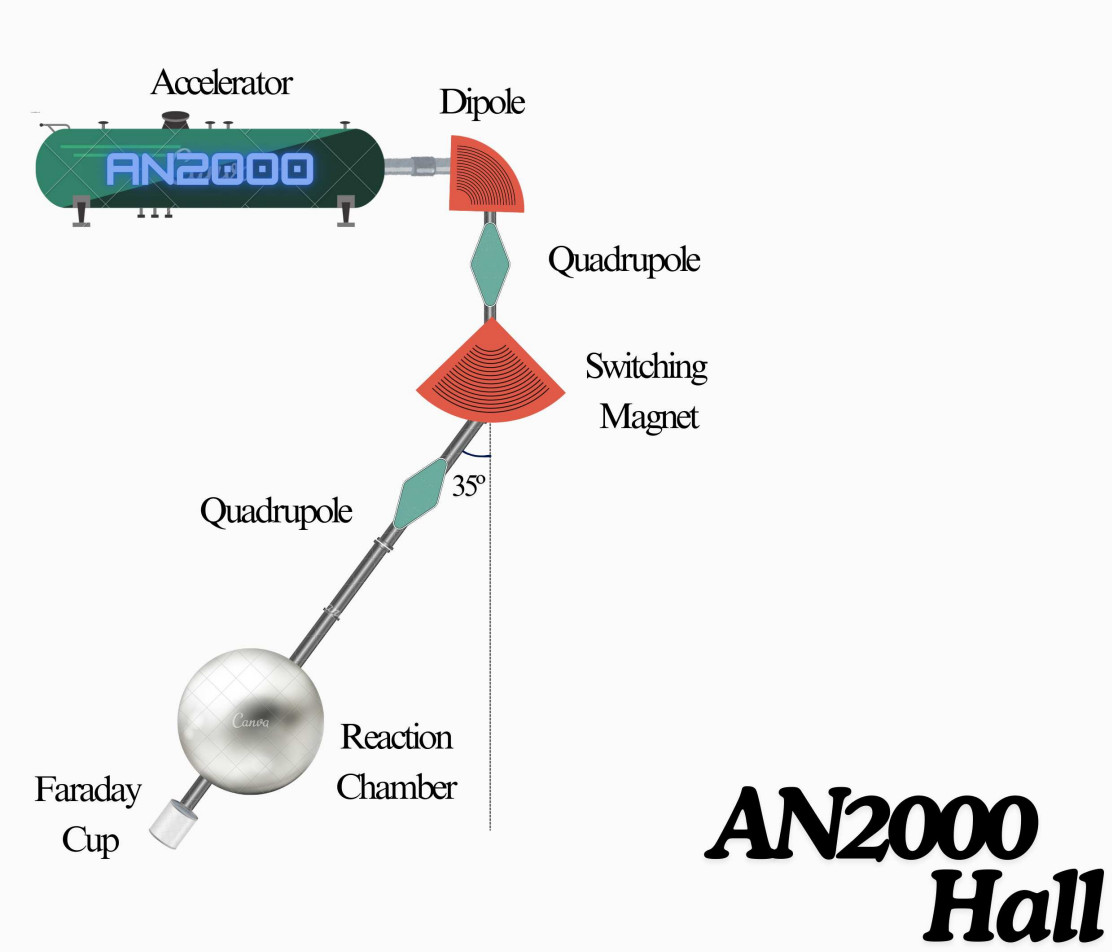


Figure 4.2: Scheme of the AN2000 accelerator Hall. The beam is transported from the accelerator machine to the reaction chamber at the 35° beamline.

A dedicated reaction chamber (1 m of diameter and 2 mm thickness) was installed at the end of the 35° beamline (see Figure 4.2). The proton beam is transported from the accelerator to the beamlines through a switching magnet. The focusing stages comprise a set of two quadrupole magnets, before and after the switching dipole, and a pair of steering dipoles: This allows the beam to be focused on both the x-axis and y-axis, obtaining a circular beam spot of a few mm diameter at the center of the target. Before reaching the chamber, a set of four slits is placed to measure the beam halo via the current induced on them and verify the beam trajectory. At the end of the chamber, around one meter after the target position, a Faraday Cup was placed to measure the current and perform the beam transport for the focusing, i.e., the two reference points for the beam alignment are the slits and the Faraday Cup.

For focusing, two pieces of quartz were placed, one before entering the chamber and one in the target position with a 1 mm diameter hole in the center (see Figure 4.3). When the proton beam hits this material, the quartz emits light. Once the beam enters through the center of the hole of the quartz, a minimum (or nothing) of light is appreciated. The current and the light coming from the quartz can be monitored from outside the hall, with the help of a Faraday Cup and a video camera, respectively. In addition, an empty aluminum frame has been placed in the target ladder (see top position in Figure 4.3) to minimize the part of the beam that hits it via the measurement of the induced current.

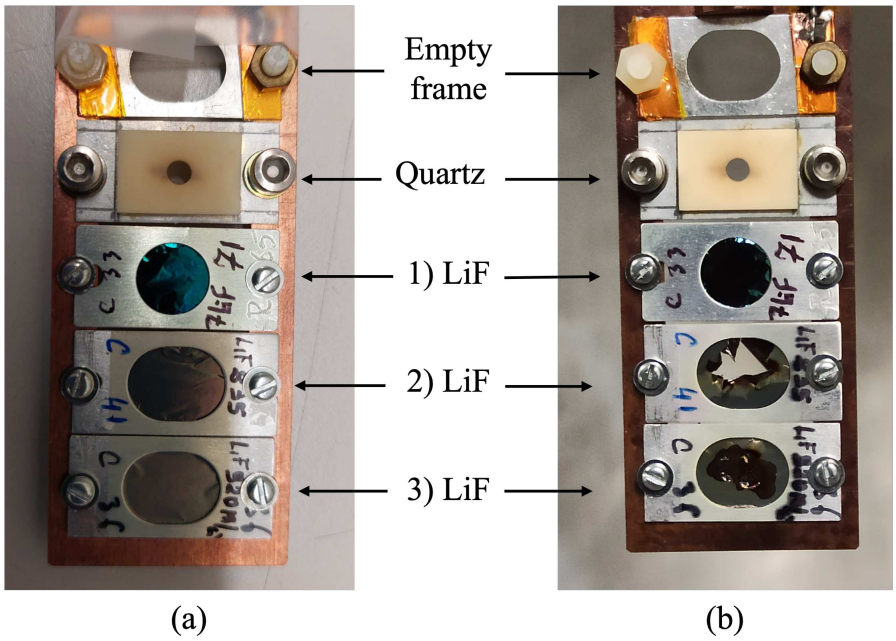


Figure 4.3: Comparison of a set of LiF targets with different thickness: 1) 71 $\mu g/cm^2$ (backing 33 $\mu g/cm^2$), 2) 235 $\mu g/cm^2$ (backing 41 $\mu g/cm^2$), and 3) 320 $\mu g/cm^2$ (backing 36 $\mu g/cm^2$). a) Shows the targets before and b) after the irradiation. The target with a backing thickness of 33 $\mu g/cm^2$ was the least damaged.

### 4.1.2 Nuclear Reactions

To study the IPC for the isovector and isoscalar transitions in $^8$Be, the selective population of the $1^+_1$ and $1^+_2$ is needed. This can be achieved via the nuclear reaction $^7$Li$(p,\gamma)^8$Be ($Q-$value = 17.254 MeV) [33]. Figure 4.4 a) shows the energy excitation function of the reaction, where the first resonance corresponds to the population of the $1^+_1$ and the second one to the $1^+_2$.

The energy excitation function drops by two orders of magnitude from the resonance at 441 keV to the one at 1030 keV, making studying the last one more challenging. Moreover, even when the two peaks are well separated in energy, they overlap, having the same value at a point between 800-900 MeV. As the energy increases, the ratio between those two cross-sections becomes more favorable for the higher-lying resonance. Experimentally, the selection of the resonance is endangered by the target thickness since it defines the integration region of the energy excitation function. The calibration of the energy of the accelerator is crucial for this step. In the case of the AN2000, the uncertainty at 1 MeV energy is ≈1 keV, which is small enough to not affect the energy selection. In the case of our study, the beam energy has been chosen as the one that placed the center of the resonance at the middle of the target (discussed in the next section). Figure 4.4 a) shows for a 100 mg/cm$^2$ LiF target (tilted 45 °, explained in *The Setup* section), where the blue-dark area represents the range of energy within the target.

In addition to the previously discussed reaction, the production of $^{16}$O in an excited state is used as a calibration point due to the high $e^+e^-$ pair emission for the $0_2^+ \rightarrow 0_1^+$ transition, which is very well-studied [6, 4]. This can be achieved with the proton-induced reaction $^{19}$F($p$,$\alpha$)$^{16}$O in a target that contains $^{19}$F (100% natural abundance), like the already mentioned LiF. The high cross-section of this reaction (of the order of barns around ~ 1 MeV proton energy) facilitates its study. Figure 4.4 b) shows the energy excitation function of the $^{19}$F($p$,$\alpha$)$^{16}$O reaction, with two areas that represent the energy loss of the beam in a 100 mg/cm$^2$ LiF target (tilted 45°, explained in *The Setup* section).

### 4.1.3 Targets

As metallic lithium is highly reactive with air, a stable target configuration requires using Li-containing molecules such as LiF and LiO. A backing material is needed for thin target layers (<1 mg/cm$^2$) to get acceptable mechanical stability. The backing materials used were Al, Cu, and C, from 10-60 $\mu$g/cm$^2$. As discussed above, the target thickness depends on the desired integration range of the energy excitation function shown in Figure 4.4 a). In the case of the 441 keV resonance, a target up to 500 $\mu$m/cm$^2$ can be used since the energy loss of the proton beam is not larger than 200 keV (see Figure 4.5) and an increase of 100 keV (from the resonance energy) of impinging beam energy is still in the

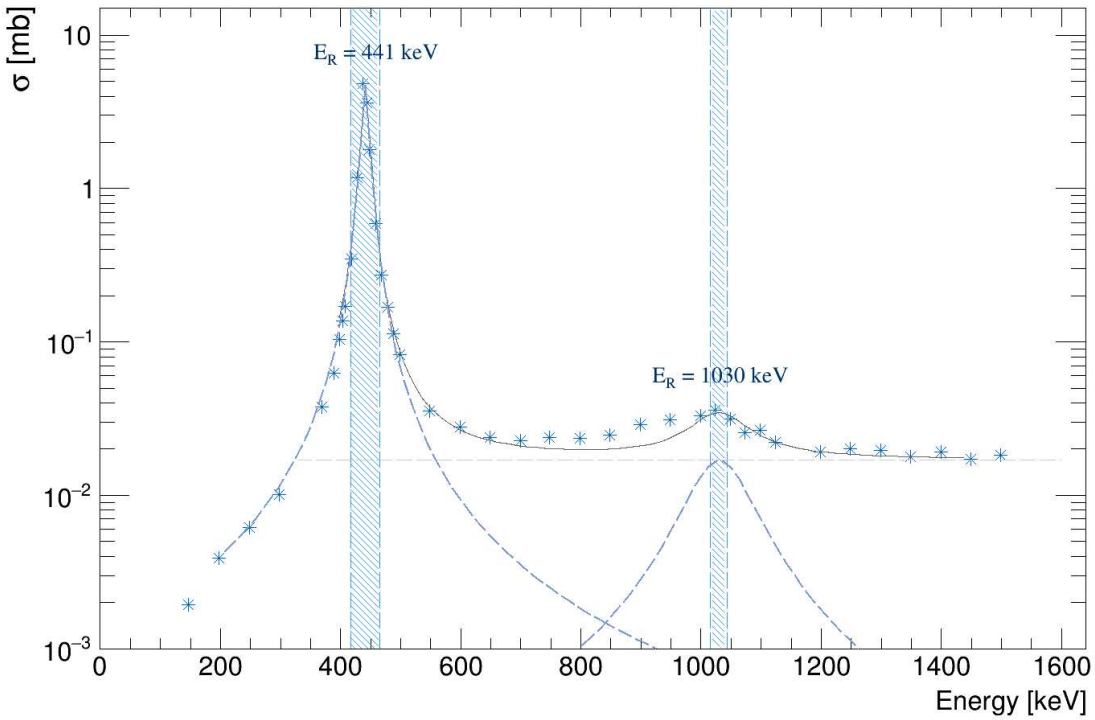


(a)

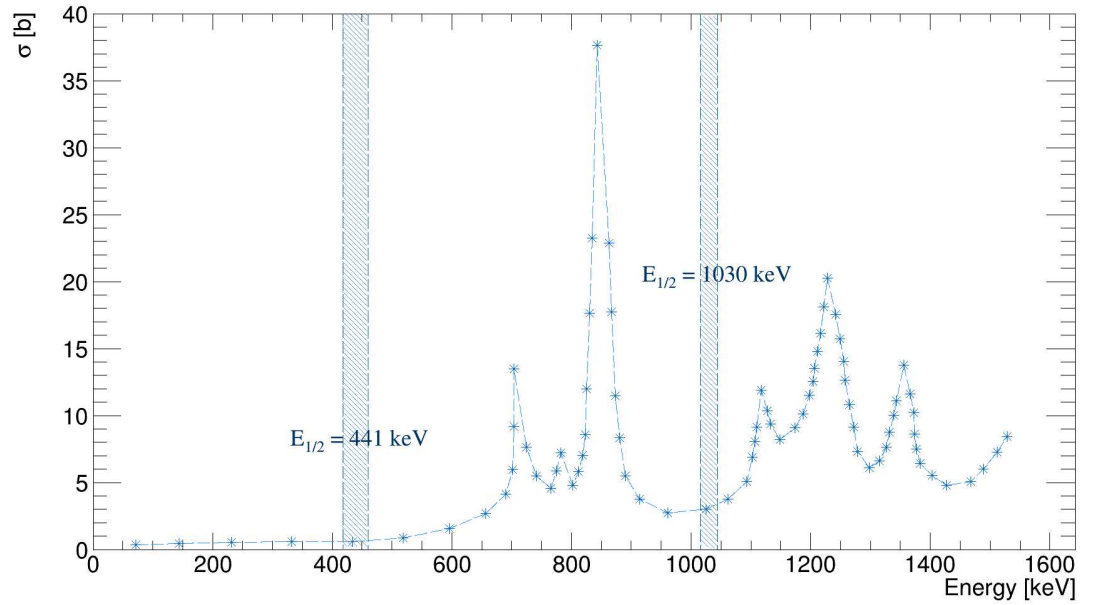


(b)

Figure 4.4: Excitation function of proton-induced nuclear reactions: a) $^{7}$Li($p$,$e^{+}e^{-}$)$^{8}$Be [33], (b) $^{19}$F($p$,$\alpha$)$^{16}$O [34]; Notation: Blue-dark area represents the energy loss of the beam in a 100 $\mu$g/cm$^2$ LiF target (tilted 45°); $E_{1/2}$ energy at the middle of the target, $E_R$ resonance energy.

region where there is not a significant overlapping with the 1030 keV resonance (which is between one and two orders of magnitude lower). For the 1030 keV resonance, a thinner target is needed. An energy loss larger than ≈30 keV from that resonance energy significantly overlaps the 441 keV resonance. By examining the energy loss shown in Figure 4.5, the maximum thickness of the target to avoid this overlap is ≈ 200 $\mu g/cm^2$, keeping in mind that the thinner the target, the lower the overlap is.

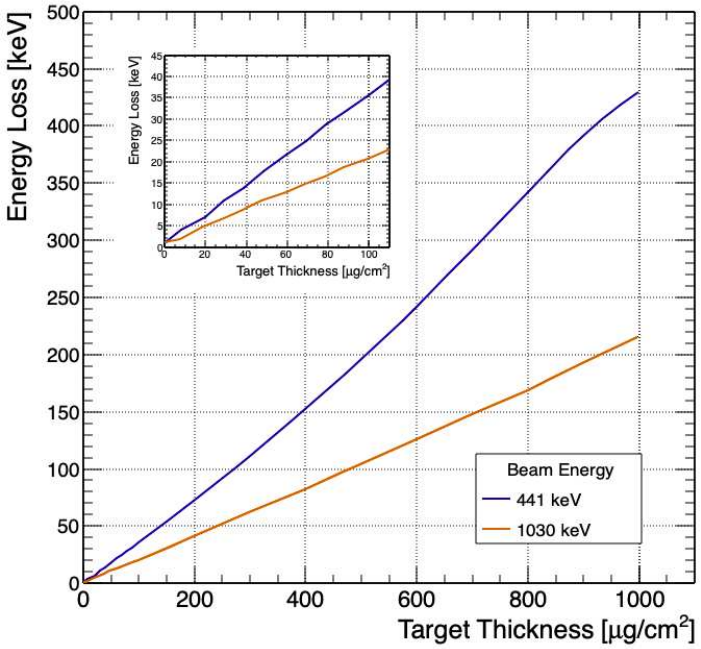


Figure 4.5: Energy loss of a proton beam as a function of the target thickness. Beam energy: 441 keV (blue), 1030 keV (orange).

The target thickness also depends on the power delivered by the beam on the target. The backing layer partially dissipates the heat. This work achieved the best performance by a 20-35 $\mu g/cm^2$ C backing because the target resisted for around two days in stable rate conditions with minimum degradation. Other configurations only allowed us to measure for 6-8 hours in stable rate conditions or before they got broken (see Figure 4.3 a) and b)).

The targets irradiated were from thickness ranging from 34 to 935 $\mu g/cm^2$ (see Table 4.1). As discussed above, the thickest ones (>100 $\mu g/cm^2$) were used only in the run commissioning to get a better collection of statistics since it allows us to integrate a more extensive range of the energy excitation function. Moreover, an attempt to use a $Li_2O$ target with 486 $\mu g/cm^2$ thickness was tested

to check its stability under irradiation conditions. Unfortunately, this target was broken immediately by a 500 nA proton beam current at 1.05 MeV. Thus, the only targets used for the study of the IPC in $^{8}$Be were the LiF ones with a thickness lower than 100 $\mu$g/cm$^2$, where the most stable ones were the ones with a thickness of around 40 $\mu$g/cm$^2$. A laser was used to check that the target was placed at the correct position in the target ladder, taking the hole in the quartz as a reference and exchanging the quartz with the target (see Figure 4.6 a)). During this experiment, the LiF target fluorescence was observed by proton irradiation, and it was a direct form of checking its integrity by monitoring with a video camera (see Figure 4.6 b)).

Table 4.1: List of targets used in the study of the IPC in $^{8}$Be

| **Target** | **Number of Targets Irradiated** | **Thickness [$\mu$g/cm2]** | **Backing** | **Backing Thickness [$\mu$g/cm2]** |
|---|---|---|---|---|
| LiF | 2 | 34-50 | C | 30-45 |
| LiF | 6 | 34-50 | C | 20-45 |
| LiF | 6 | 51-100 | Cu/C | 25-60 |
| LiF | 3 | 101-200 | Cu/C | 25-60 |
| LiF | 1 | 201-300 | Cu/C | 25-60 |
| LiF | 3 | 301-400 | Cu/C | 25-60 |
| LiF | 2 | 900-1000 | Cu/C | 25-60 |
| $Li_2O$ | 1 | 486 | Al | 34 |

In summary, the target thickness selection was based on the energy deposited by the proton beam; the thicker the target is, the more energy is deposited. This means that the target will have to be replaced more often than a thin one. But the most important fact to consider is that a thin target will allow us to reduce the population of the $1_2^+$ state in $^{8}$Be (see Figure 4.4 a)). For this experiment, the optimal value of the target thickness was in the range 34-100 $\mu$g/cm$^2$ with a C backing of 30-50 $\mu$g/cm$^2$ thickness.

### 4.1.4 The Setup

#### Detector Array

The three stages of the experiment involved different detector (see Figure 4.7) configurations (see Table 4.2). In the commissioning, two clover detectors

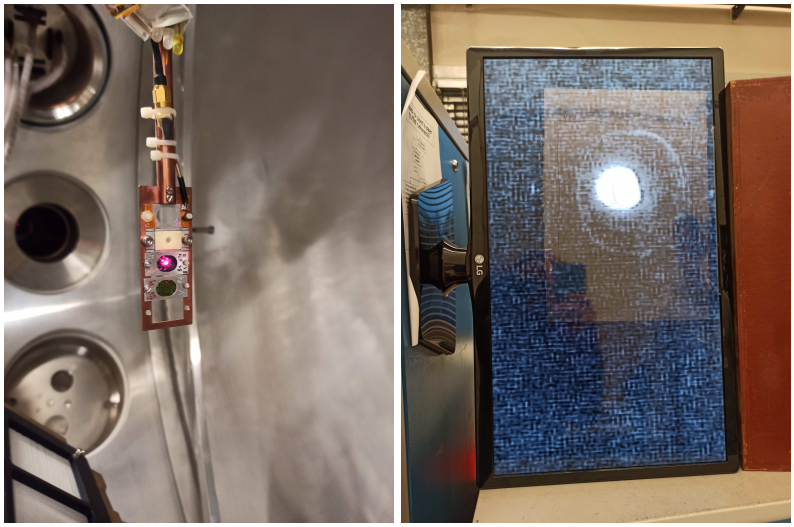

(a) (b)

Figure 4.6: (a) Target alignment by a pointing laser, (b) Target fluorescence during the irradiation.

were placed at 30° and 315° (see Figure 4.8 a)). The target-detector distance was 12.5 cm for the two clovers. This configuration was chosen because the angular distribution of the pair emission drops quickly with the correlation angle, and it was better to start with favorable conditions. The target was tilted 45° toward the beam direction, facing the clovers and avoiding shadowing them. The data recorded consisted of 155 hours of irradiation (76 hours at 441 keV and 79 hours at 1.05 MeV). To monitor the population of the states of interest and the integrity of the target in the three stages, a $LaBr_3$ detector was placed outside the chamber (≈0.5 m far from the target, see Figure 4.9).

Table 4.2: Detector configuration of the three-stage campaign and data collection information. The reduction of the disk space usage in Experiments I and II is due to the trigger condition used during the acquisition.

| **Experiment** | **Number of Clovers** | **Angles [∘]** | **Time [hrs]** | **Data Size [Gb]** |
|---|---|---|---|---|
| Commissioning | 2 | 30, 315 | 155 | 161 |
| Experiment I | 4 | 30, 165, 240, 315 | 236 | 117 |
| Experiment II | 4 | 30, 150, 240, 330 | 392 | 202 |

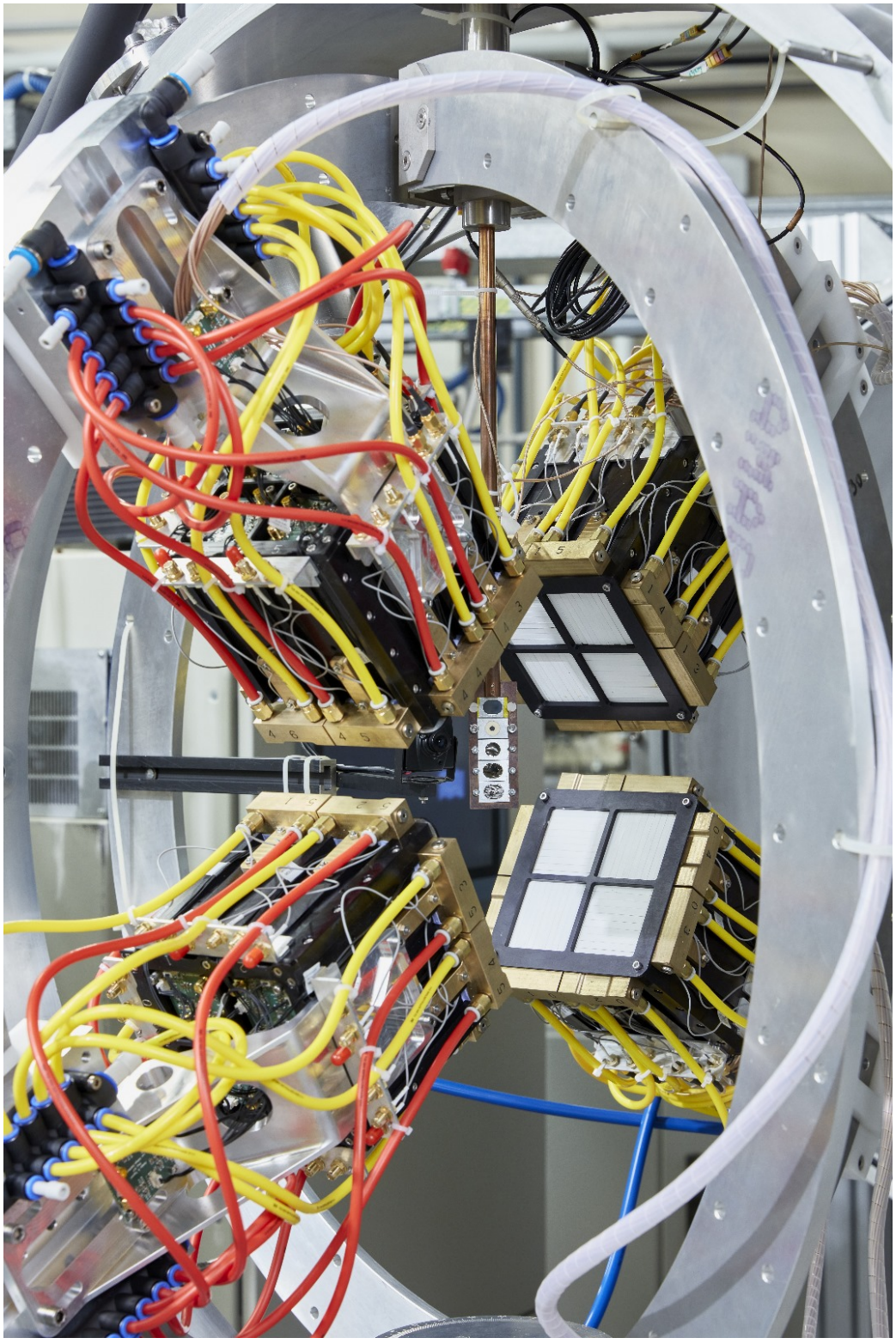

Figure 4.7: Status of the setup at the AN200 accelerator at the INFN-LNL. Four Clover detectors are placed in two half-ring structures.

(a) (b) (c)

Figure 4.8: Detector array configuration for the (a) commisioning, (b) first experiment, and (c) Second experiment.

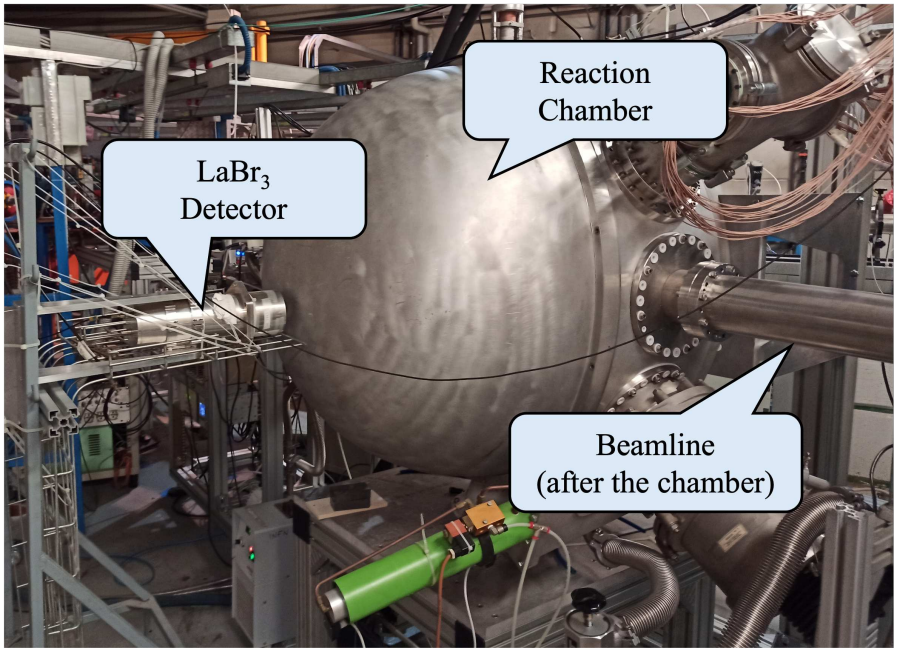


Figure 4.9: 3 inch diameter × 3 inch thickness $LaBr_3$ detector outside the chamber ( ~0.5 m from the target).

The first experiment was performed with four clovers at 30°, 165°, 240°, and 315° (see Figure 4.8 b)). The distance was the same as in the commissioning experiment. Geant4 simulation showed a maximum efficiency between 140° and 160° relative angle (see Figure 2.30 b)), the angle of the anomaly reported by A. Krasznahorkay [5]. The target was tilted 45° as well. The data recorded

was 236 hours of beam irradiation at 1.05 MeV. The lower data size than the commissioning is due to the trigger condition used in the acquisition (discussed in the next section). Unfortunately, two telescopes had issues with the position measurement, so the data involved 14 telescopes instead of 16.

Finally, the second experiment of the campaign was carried out with four clovers at 30°, 150°, 240°, and 330° (see Figure 4.8 c)). This time, two clovers were placed 0.5 cm further to accommodate clovers at 30° and 330°. Using this configuration, Geant4 simulation showed a slow increasing behavior in the efficiency in the range 120°-160° (see Figure 2.30 c)). To avoid shadowing some bars, the target and detectors were tilted 45° to the beam direction. The data collection lasted 93 hours at 441 keV and 299 hours at 1.05 MeV.

#### Electronics

As discussed in Chapter 3, every telescope contains two SiPMs in the front bars layer, two SiPMs in the back bars layers, and two SiPMs in the calorimeter. This means six readout channels are needed to convert analogic signals to digital ones. From inside the chamber through PCB connectors (see Figure 4.10a)), the preamplified signals were sent to the CAEN digitizer model V1730 (16 channels, 14-bit 500 MS/s) or model V1725 (16 channels, 14-bit, 250 MS/s). Those digitizers offer an appropriate sampling speed for the SiPM coupled to the scintillator material used in manufacturing the detectors (EJ-200, rise time 0.9 ns, decay time 2.1 ns). The signals were sent to a PC through an optical fiber chain, and the PC read out the signals using the CAEN A1838 interface. The data acquisition system (DAQ) has been configured to handle up to 112 channels (96 for the telescopes and 16 for ancillary detectors, see Figure 4.10b)).

Every pair of signals from the same part of the telescope (either front bars, back bars, or calorimeter) was connected to the same digitizer. In the commissioning run case, three digitizers were used (8 telescopes), and six for the subsequent experiments (16 telescopes). To reduce the noise signals, the acquisition was carried out considering the coincidence of the pair of signals (see Figure 4.11 a)). In the commissioning experiment, the coincidence measurement was achieved by changing the configuration of the registers of the digitizers. Meanwhile, a dedicated digital trigger processor firmware was developed and used for the experiments with four telescopes. The trigger signal was generated when a signal was registered either in the two pairs of SiPM of the front and back

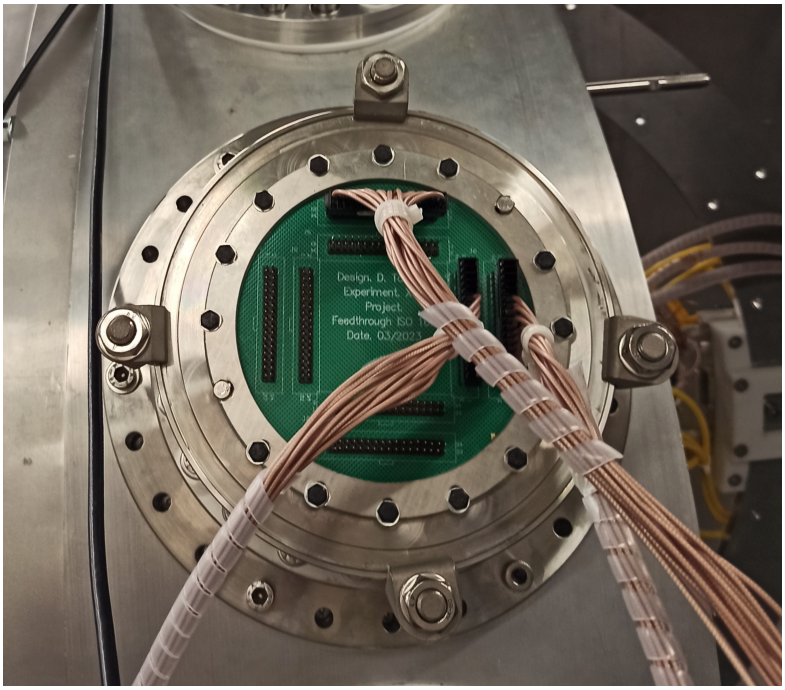

(a)

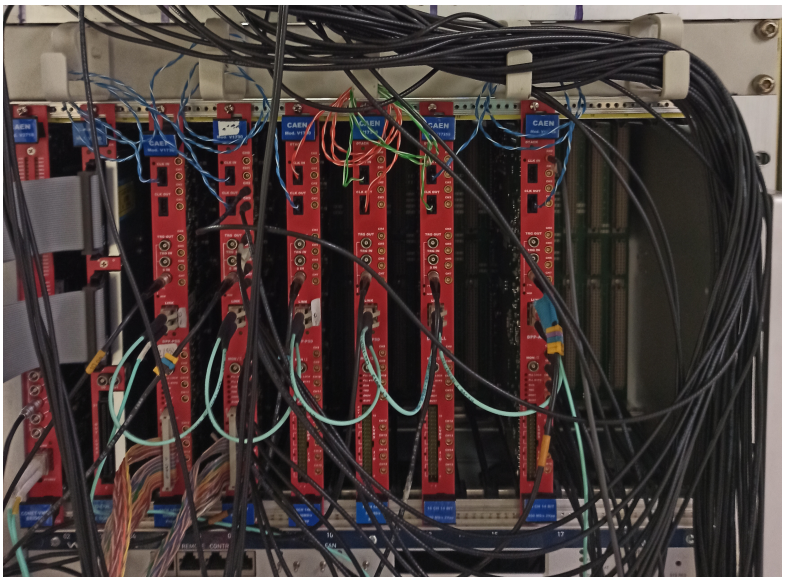

(b)

Figure 4.10: (a) PCB connector flange on the chamber, (b) Acquisition system used in the experiment.

bars of one telescope or the two SiPM of the calorimeter (see Figure 4.11 b)). A V1495 CAEN board was used to analyze the Low Voltage Differential Signaling (LVDS) output from the digitizers, and generate the validation signal when the logic shown in Figure 4.11 b) was true. The synchronization of the digitizers was

achieved propagating the clock of the first digitizer to all the others and using a common start signal generated by the VME Controller Board V2718 at the start of the run. Regarding the $LaBr_3$ ancillary detector, the data was acquired triggerless but in the same clock chain described above.

The Digital Pulse Processing for Charge Integration and Pulse Shape Discrimination (DPP-PSD) CAEN firmware was used to process the signals in the acquisition. Therefore, the integral value of the signals (energy value) in a 500 ns window was recorded, but no traces were acquired to limit the data-bandwidth. In addition, a second integral value was recorded with a shorter window length (250 ns).

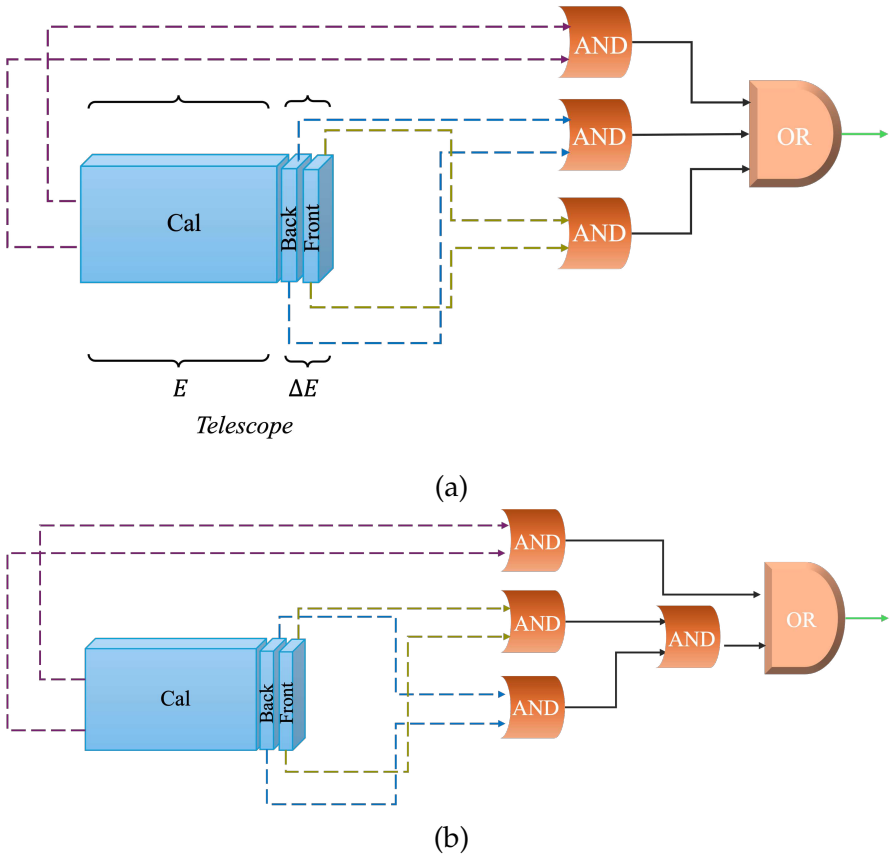


Figure 4.11: Logic of the acquisition trigger for one telescope in the (a) commissioning, where every pair of signals from the SiPMs either of the front bars, back bars, or calorimeter of one telescope were acquired in AND logic (b) first and second experiment, in addition to the logic used in the commissioning, the four signals coming from the two pairs of SiPM of the front and back bars triggered the acquisition when they were in coincidence. Every telescope was acquired in OR logic.

## 4.2 Data Processing

This section describes how the raw data provided by the acquisition system are processed. The ROOT-CERN package, a software based on C++, has been used as the main framework. This code provides the standard tools used in nuclear and particle physics experiments. A set of dedicated classes has been developed for the present data analysis.

### 4.2.1 Event Building

The structure of the output data from the DAQ is a ROOT TTree object called "Data_R", provided by the COMPASS software. The TTree contains the following branches (the type of variable is shown in parenthesis):

1. **Channel.** Channel of the digitizer that registers an entry (short integer).
2. **Timestamp.** Time when an entry was registered in picoseconds (long integer).
3. **Board.** Digitizer number that registers an entry (short integer).
4. **Energy.** Long integration gate (500 ns) of the signal (short integer).
5. **Short.** Short integration gate (250 ns) of the signal (short integer).
6. **Flag.** Identification number of the entry quality (integer).

The data processing is divided into two parts: event building and data replay. The first is performed using a modified C++ code by A. Goasduff at LNL-INFN, which aims to time order the data to sort them in time window packages, keeping the same structures of the vectors. The script takes a buffer of 10000 entries from the Data_R TTree and saves them in time window packages. The number of entries and the width of the coincidence window can be modified. The process starts sorting the entries of the buffer by time. The first element is taken as a reference, and its timestamp is assumed as the initial value of the event $TS_0$. Then, the code makes a loop in the other entries of the buffer to evaluate if the timestamp of the $i$-th ($TS_i$) differs from $TS_0$ by a specific value corresponding to the coincidence time window ($TW$) set. The entry values are saved into vectors, and the number of elements in the event is saved into a variable called "Fold." If the time of the following entry is not inside the time window, the loop ends and such entry is the first element for the next event. Figure 4.12 shows the

events inside a time window length of 300 ns, which has been selected to build the events. No significant changes were observed by reducing the length of this window to 100 ns, but the time spent in data sorting was longer than the one of 300 ns. The larger time window resulted in being the most time-efficient without losing events related to the $e^+e^-$ pairs.

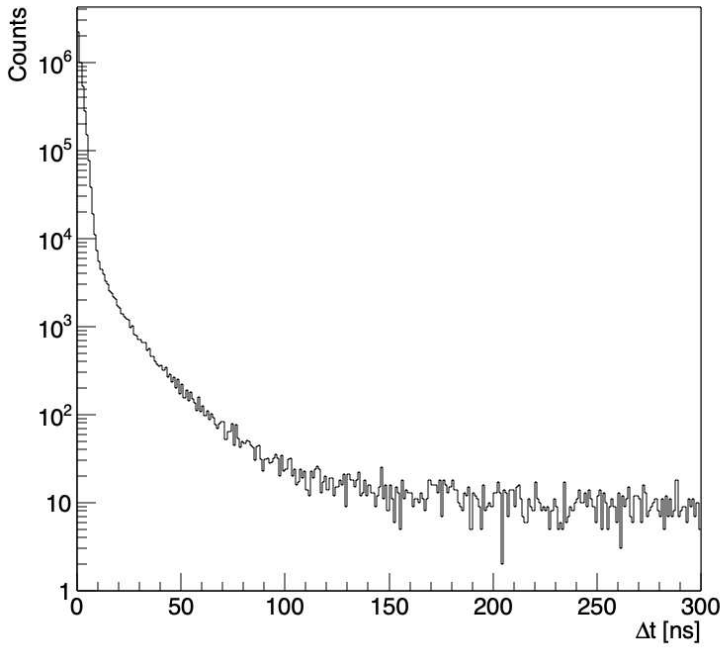


Figure 4.12: Time difference among the entries in events built using a time window of 300 ns

## 4.3 Data Replay

The second part of the data processing consists of creating the TTree object from the sorted TTree discussed in the previous paragraph. The reason for making a second TTree, MetztliTree, is that the previous structure is not feasible for a quick check or could be very complicated. The code was written for this specific experiment, but the classes implemented can be used for any experiment with a COMPASS ROOT output. The procedure aims to classify the data among the different types of detectors and create variables useful for calibration and analysis. To profit from the ROOT/C++ tools, all the analysis is implemented under the classes framework listed in the table 4.3.

Table 4.3: Mean class description used in the replay of the data.

| Class Name | Description |
|---|---|
| *MetztliConf* | Reads the configuration parameters. Able to read vectors, units, comments |
| *MetztliRawDetctor* | Saves the signal and timestamp of a specific detector (either a SiPM, a LaBr detector or could be any other ancillary) in a general way |
| *MetztliRawSiPM* | Contains six MeztliRawDetector objects for the six types of SiPM's |
| *MetztliRawBars* | Saves the position, energy and timestamp of the front or the back bar layers |
| *MetztliRawCalorimeter* | Saves the sum of the energy, and timestamp of the two SiPM in one telescope for the calorimeter |
| *MetztliRawTelescope* | Contains the position, energy and timestamp a telescope when the six signals are contained in the same events |

The methodology consisted of creating an object for every detector using the MetztliRawDetector Class, one object for every type of SiPM and LaBr. To avoid creating heavy files, the vector array of the detector information only contained values different from zero in the signal variable, and the vector size depended on it.

The replay process aims to create the telescope structure, which includes the deposited energy in every layer (front, back, and calorimeter), the timestamp (timestamp of one of the two SiPM of the calorimeter), the hit position reconstruction in the telescope. The main restriction is the time coincidence between the pairs of SiPMs in every layer. Figure 4.13 shows the timestamp difference between those pairs (violet: front; blue: back; green: calorimeter). A time window length of 10 ns is enough to avoid events far from the coincidence peak.

The second restriction is the time coincidence among the three parts of the telescope (front bars, back bars, and calorimeter). Three combinations can be considered to ensure the triple coincidence: front-back, back-calorimeter, and front-calorimeter. Figure 4.14 shows the coincidence peaks for every combination, where a time window length of 10 ns is enough to validate the coincidence.

To summarize, the telescope data structure will be filled only when the time coincidence condition of 10 ns in every pair of SiPM of the same part of the telescope (front bars, back bars, and calorimeter) is achieved, as well as the three

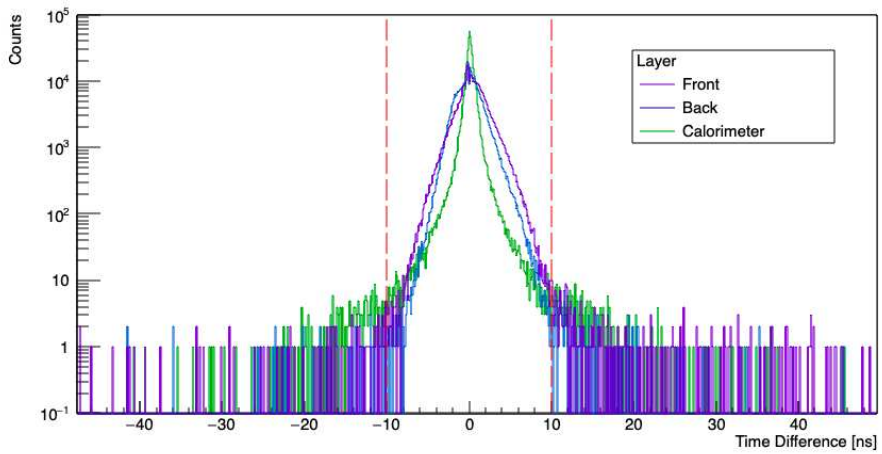


Figure 4.13: Time difference distribution of the pair of SiPM in every layer. The time difference between the front and back bars is broader than in the case of the calorimeter due to the treatment of the signals in the reduced channel 10×1 SiPM board to get the energy deposited, and the bar fired (described in [27]).

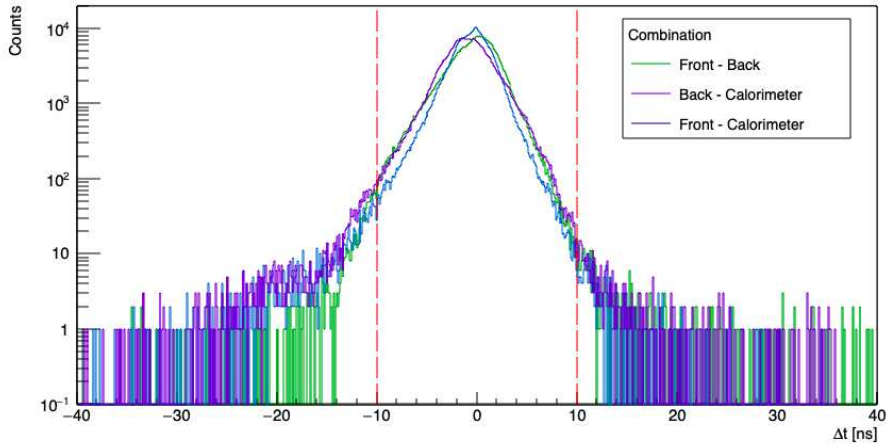


Figure 4.14: Time difference of the three different combinations of layers

combinations of them. This structure will be the base of the analysis described in the next chapter.

## 4.4 Calibration

The calibration of the detector array is divided into two parts: energy and position. Energy calibration is based on comparing the energy spectra with Geant4 simulations. Position calibration is achieved by considering the size of

the bars. The methodology employed is explained below.

### 4.4.1 Energy

#### Calorimeter

For the low energy calibration of the calorimeter block, the high emission of $\gamma$ rays from the $e^+e^-$ annihilation was considered. Since the detector material is not ideal for $\gamma$ ray detection, the Compton scattering is the most likely. Thus, the energy spectrum shows a peak corresponding to the Compton edge at 341 keV as in Figure 4.15 is observed. This spectrum does not include coincidence among the $\Delta$E and E parts of the telescope; otherwise, the $\gamma$ rays are reduced drastically (discussed in the next Chapter).

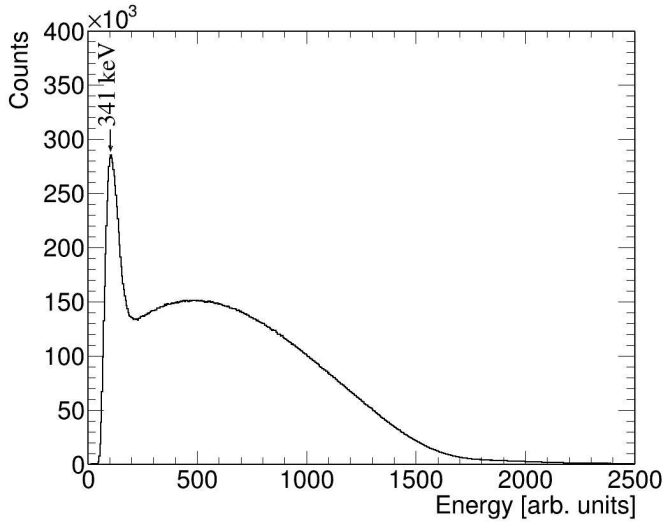


Figure 4.15: Energy spectrum (no calibrated) of the deposited energy in the calorimeter block, where the $\gamma$ ray, corresponding to the $e^+$-$e^-$ annihilation events, deposited its energy via the Compton effect.

The high energy (>1 MeV) calibration of the calorimeter is complicated because there are no monoenergetic $e^-$ (or $e^+$) radiation sources in the energy range of MeV. For this reason, a novel method was implemented considering the high cross-section at 1.03 MeV proton beam irradiation for the IPC process in the $0_2^+ \rightarrow 0_1^+$ transition in $^{16}$O. A pair of telescopes in the same clover is more likely to detect a $e^+e^-$ pair than two telescopes in different clovers. Considering a single pair of telescopes, the energy correlation matrix shows a region with a high concentration of counts corresponding to the transition previously mentioned

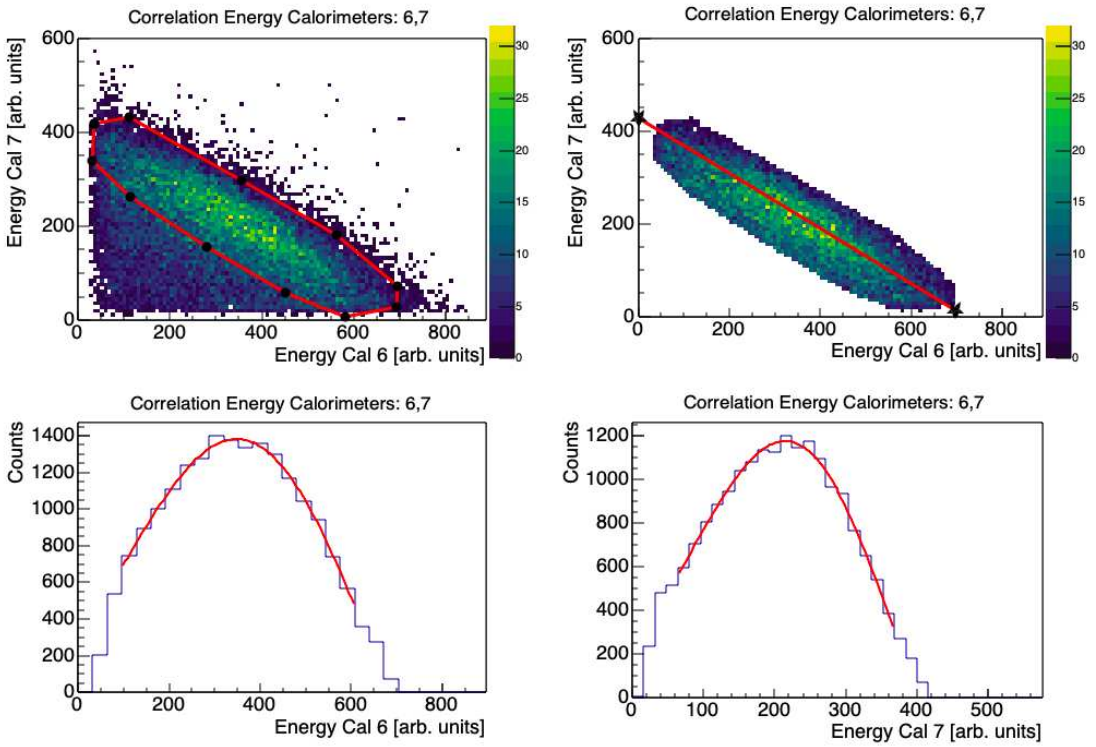


Figure 4.16: Energy deposited in the telescopes 6 and 7 by $e^+e^-$ pairs from the IPC process in the $0_2^+ \rightarrow 0_1^+$ transition in $^{16}$O. Correlation energy matrix (not calibrated) of two telescopes in the same clover in coincidence (Top-left). Selected events from the correlation matrix corresponding to events where the $e^+e^-$ pair deposited all of its energy in the telescopes (top-right). The red line shows the extrapolation of the *antidiagonal* region created by those events. Projection of the selected events in the energy axis of the telescope 6 (bottom-left) and 7 (bottom-right).

(see the top-left matrix in Figure 4.16). Making a gate on this region, the wall-effect events are neglected, and only the events where the $e^+e^-$ pair deposited practically all of this energy are considered (see the top-right matrix in Figure 4.16). Then, projecting those selected events on the axis of each of the telescopes (see the bottom histograms in Figure 4.16), the energy spectra help us identify the centroid, corresponding to the events where the $e^+$ and the $e^-$ were emitted with similar energies. The value of this energy point was extracted from the Geant4 simulation, obtaining an energy of 1.77 MeV. Another calibration point can be determined by extrapolating the intersection points of the *antidiagonal* with the axis of every telescope, as the red line of the top-right matrix of Figure 4.16 shows. This energy value is the maximum energy deposited by either a $e^+$ or a $e^-$ from the abovementioned electromagnetic transition. Geant4 simu-

lations showed that this value is 3.48 MeV. This last point completes the set of three calibration points for the calorimeter block.

### Bars

The energy calibration of the bars has been performed by one single point since there are no monoenergetic $e^-$ (or $e^+$) radiation sources, and a $\gamma$ rays source does not produce any structure in the energy spectrum of the bars useful for the calibration. The calibration point corresponds to the energy deposited by the $e^-$ (or $e^+$) when it passes through the whole thickness of the bars (see Figure 4.17). To be sure that the $e^-$ (or $e^+$) arrived at the calorimeter block, the coincidence between the $\Delta$E and the E parts of the telescoped was implemented, and the data corresponded to the pairs from the $0_2^+ \rightarrow 0_1^+$ transition in $^{16}$O. The energy estimation of this point was done via Geant4 simulations, obtaining a value of 0.32 MeV and 0.33 MeV for the front and back bars layers, respectively.

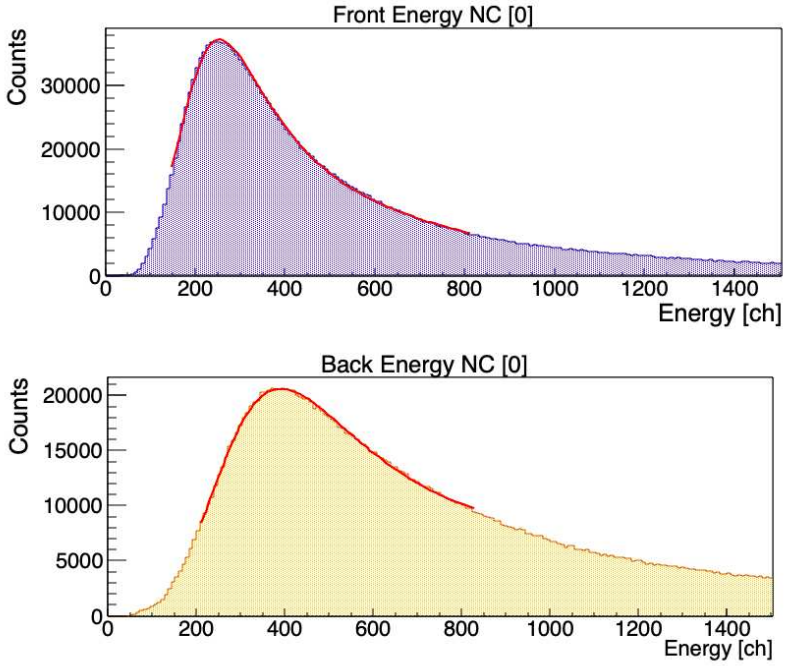


Figure 4.17: Deposited energy of $e^-$ (or $e^+$) passing through the whole thickness of the front bars layer (top) and back bars layer (bottom).

### 4.4.2 Position

The position calibration of the front and back bars layers was performed considering the histograms created by using Equation 2.3 in the experimental data (see Figure 4.18), where ten peaks were observed (corresponding to every bar in the layer). A sum of ten Lorentzian functions was fit to the data to calculate the centroid of each peak. As a note, the position resolution of the front bars layer is possibly affected by the light coming from the target.

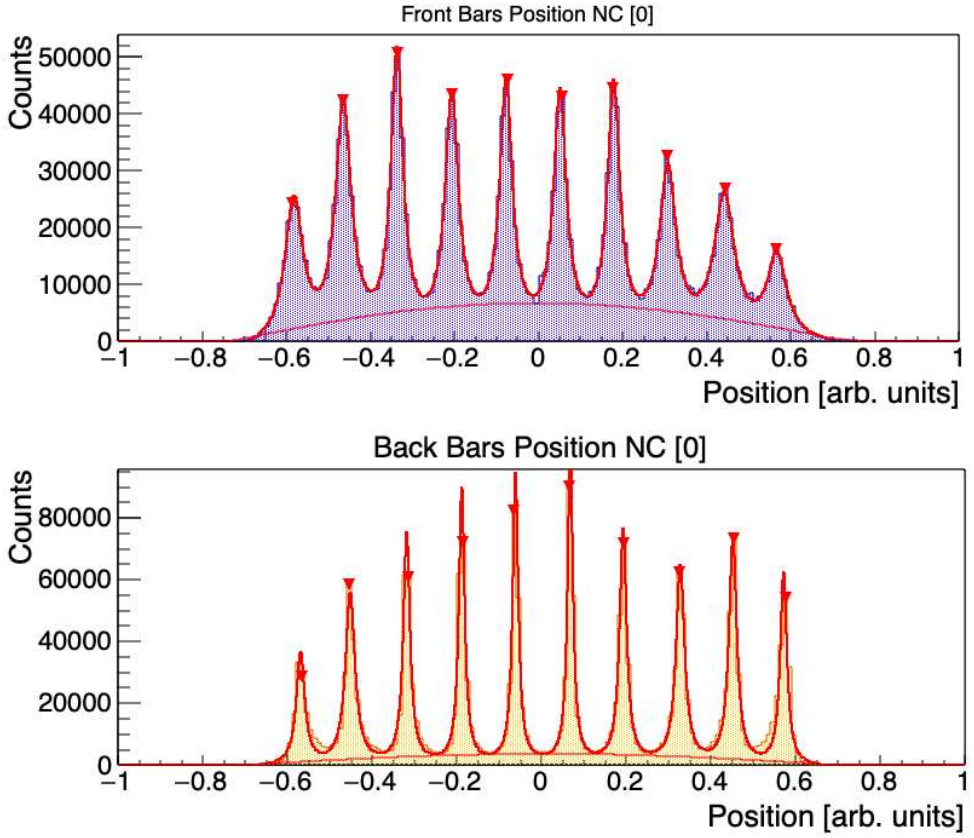


Figure 4.18: Posiiton histogram of the front (top) and back (bottom) bars layer. A fit of a sum of ten Lorentzian functions is shown in the red lines.

To assign a value to every peak in the position histograms, the local reference system chosen was the one where the origin ($x = 0$) was between the 5th and 6th bars, and the distance among the peaks corresponds to the width of the bar (5 mm). Figure 4.19 shows the fits performed for the front (top) and back (bottom) bars layers of the positions histograms of the histograms shown in Figure 4.18, where a linear behavior is observed.

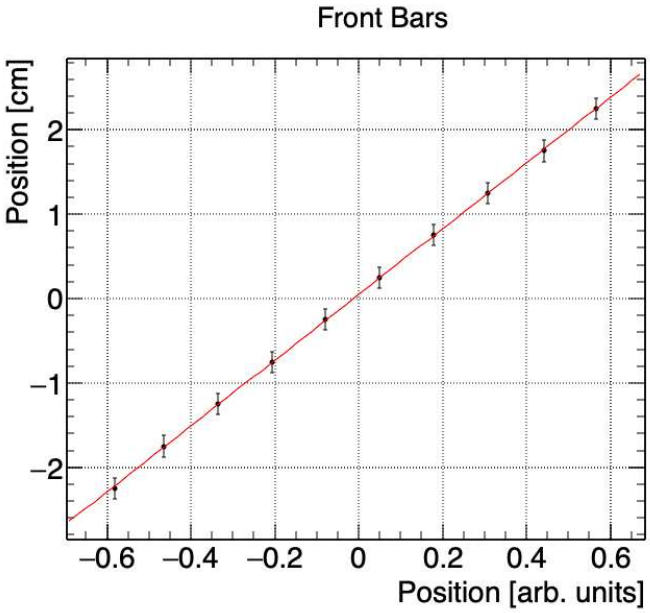


(a)

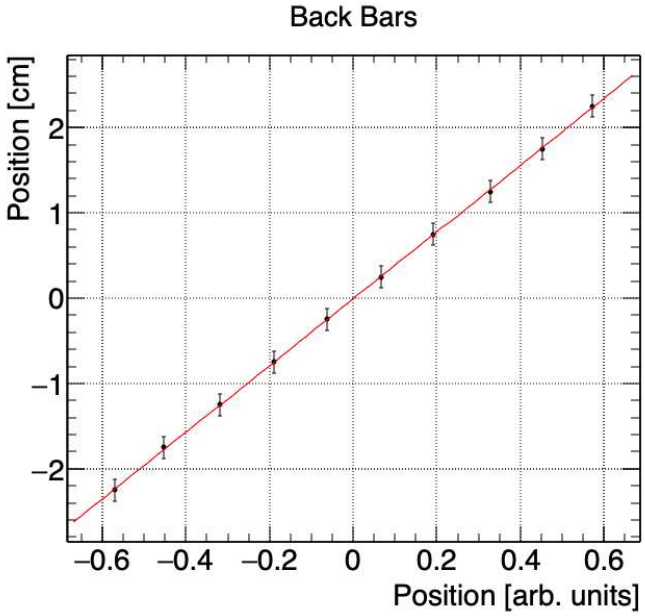


(b)

Figure 4.19: Linear fit (red line) of the position calibration for the a) front and b) back bars layers.

# 5

# Data Analysis and Results

*The present chapter describes the experimental data analysis process. The transition energy reconstruction from the coincidence of the detectors and the reconstruction of the angle between the $e^+$ and $e^-$ as a function of the total energy of the pair in the IPC process are discussed. Eventually, the $e^+e^-$ pair angular correlation distribution for the $0_2^+ \rightarrow 0_1^+$ transition in $^{16}O$ is derived and discussed.*

## 5.1 Data Analysis aim

The analysis of the experimental data aims at determining the $e^+e^-$ relative angle distribution for pairs corresponding to a specific electromagnetic transition. The pairs are selected, event by event, by reconstructing the total particle multiplicity, the total energy, and the energy asymmetry. The data have been prepared and calibrated as described in the previous chapter.

## 5.2 Telescope multiplicity

The first step of the analysis is to check if the data set contains events where more than one telescope registered a signal corresponding to an incoming particle. In the analysis, one telescope is considered hit by a lepton when the three detector layers (two bars of the tracking layer plus the calorimeter) simultaneously detected the radiation, which means that the 6 SiPMs of the telescope registered a signal in a 300 ns time coincidence window. This condition allows

the suppression of the single SiPM dark noise and is expected to strongly reduce the $\gamma$-ray background, as Figure 5.1 shows. The latter effect is particularly important because $\gamma$-ray emission is the main path for the depopulation of the $1^+$ state in $^8$Be and the $3^-$ state in $^{16}$O, and also that the $e^+ - e^-$ annihilation emits $\gamma$-rays, representing the main source of beam-induced background.

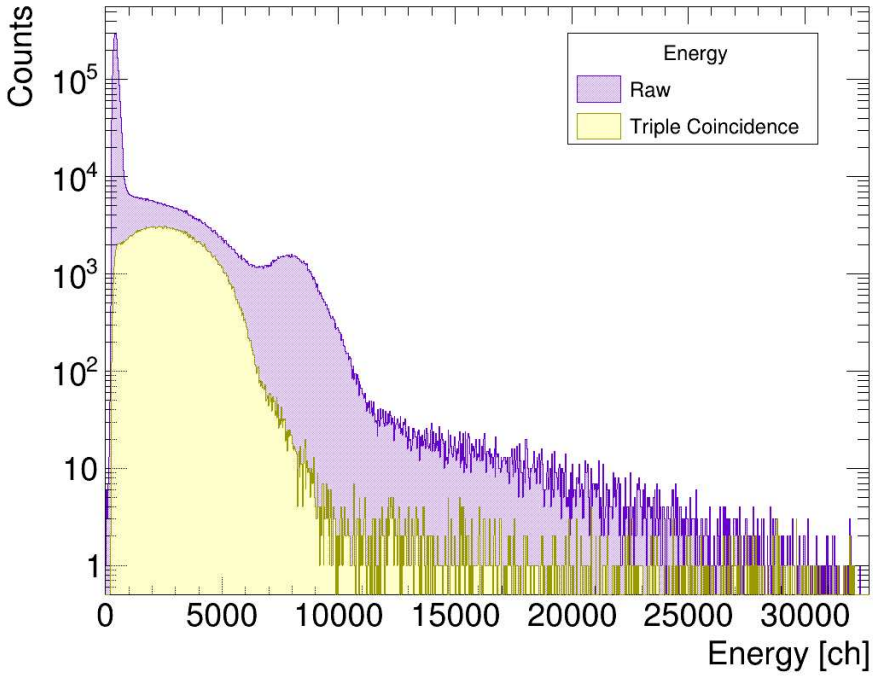


Figure 5.1: Deposited energy in the calorimeter block: a) raw, and b) in coincidence with the two pairs of SiPMs in the front and back layers. Data from the 1.03 MeV proton beam energy irradiation.

Under the triple coincidence condition, Figures 5.2 a), b), and c) show the experimental telescope multiplicity for the data set of the commissioning, experiment 1 and experiment 2, respectively. The obtained distribution can be reasonably explained as follows: events with multiplicity 1 represent the most probable cases where, given the limited angular coverage of the setup, only one lepton was detected. Multiplicity 2 is of interest for the following analysis as it identifies events where at least two leptons have been possibly detected. The multiplicity values higher than two can be due to actual $e^+e^-$ where one or more leptons were scattered in the materials inside the chamber (including the detectors), the cosmic muons passing through the detector array, or any combination with the background sources. For those reasons, the condition of multiplicity 2 is fundamental but not definitive because it does not allow us neither to select the

electromagnetic transition that generated $e^+/e^-$ pair, nor discriminate External Pair Creation (EPC), nor $\mu - e^+/e^-$ coincidences. At this stage, narrowing the time window of the coincidence can increase the quality of the pair selection, as discussed in the next paragraph.

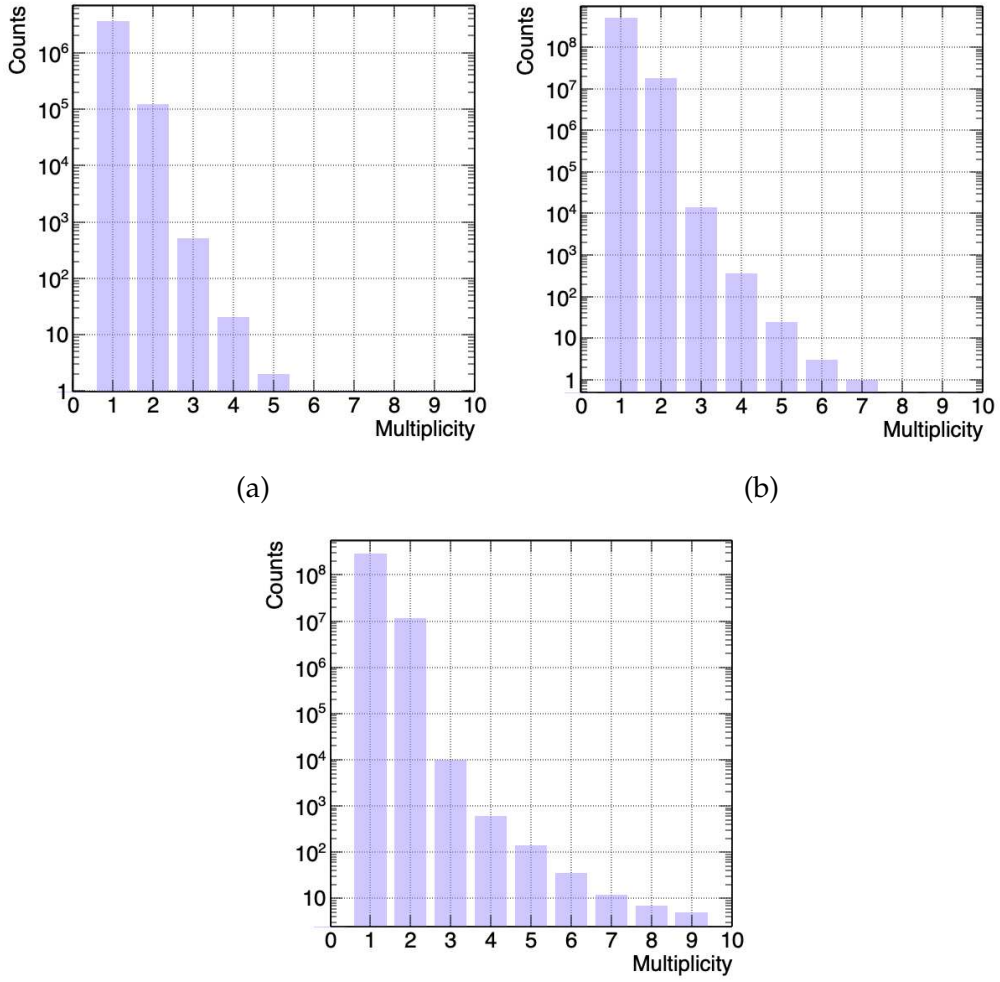


Figure 5.2: Telescope multiplicity of the a) Commisioning (Conf 1), b) first experiment (Conf 2) and c) second experiment (Conf 3).

## 5.3 Time Coincidence Window

The cornerstone of the $e^+e^-$ pair detection is a tight time coincidence window. The time difference ($\Delta$t) of the two telescopes in coincidence depends on the kinematics of the particles and the response of the detector. Considering

that the rise time of the plastic scintillator EJ-200 is 0.9 ns, the decay time is 2.1 ns, and for a 0.5 MeV kinetic energy (≈ minimum energy of the $e^+e^-$ to pass through the two bars layers of the telescope), the time spent by $e^+/e^-$ in traveling from the target to the detector is ≈ 0.5 ns, a time window $|\Delta t|$ of 5 ns (see Figure 5.3) is enough to select the pairs coming for the IPC process. Figure 5.4 shows

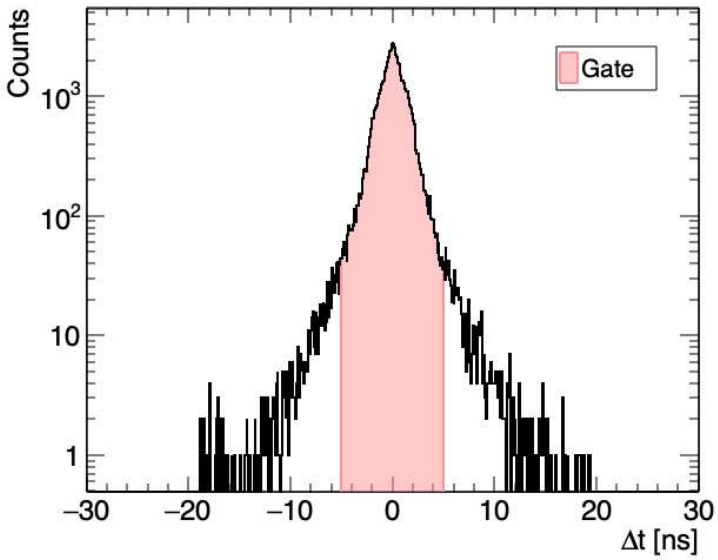


Figure 5.3: Telescopes time coincidence with a gate of $|\Delta t|$ of 5 ns.

the correlation among the telescopes in a 10 ns time window for (a) the commissioning experiment (and (b)), (c) for the first and (d) second experiments. Figures 5.4 a) and b) show the time coincidence of every possible combination of the eight telescopes used in the in-beam commissioning of the setup. In Figure 5.4 a), two prominent groups of bars appear, representing coincidences inside the same clover (clover 0: telescope ID 0-3; clover 1: telescope ID: 4-7). On the other hand, Figure 5.4 b) shows the projection of the telescope correlation, and the low probability of coincidence between two telescopes of a different clover is more evident. For example, the correlation between telescope IDs 1 and 2 (in the same clover) is much higher than between telescope IDs 1 and 6 (in different clover). This behavior indicates that the emission of the detected particles has a higher probability for small angles (same clover) than for large ones (different clovers). Indeed, the angular correlation distribution of the $e^+e^-$ emission in the IPC process for $M1$, $E0$, and $E1$ transitions decreases with the separation angle [4, 2, 3]. Thus, the telescope correlation matrix is globally consistent with the

expected pair distribution. The next step is reconstructing the transition energy that created the $e^+e^-$ pair.

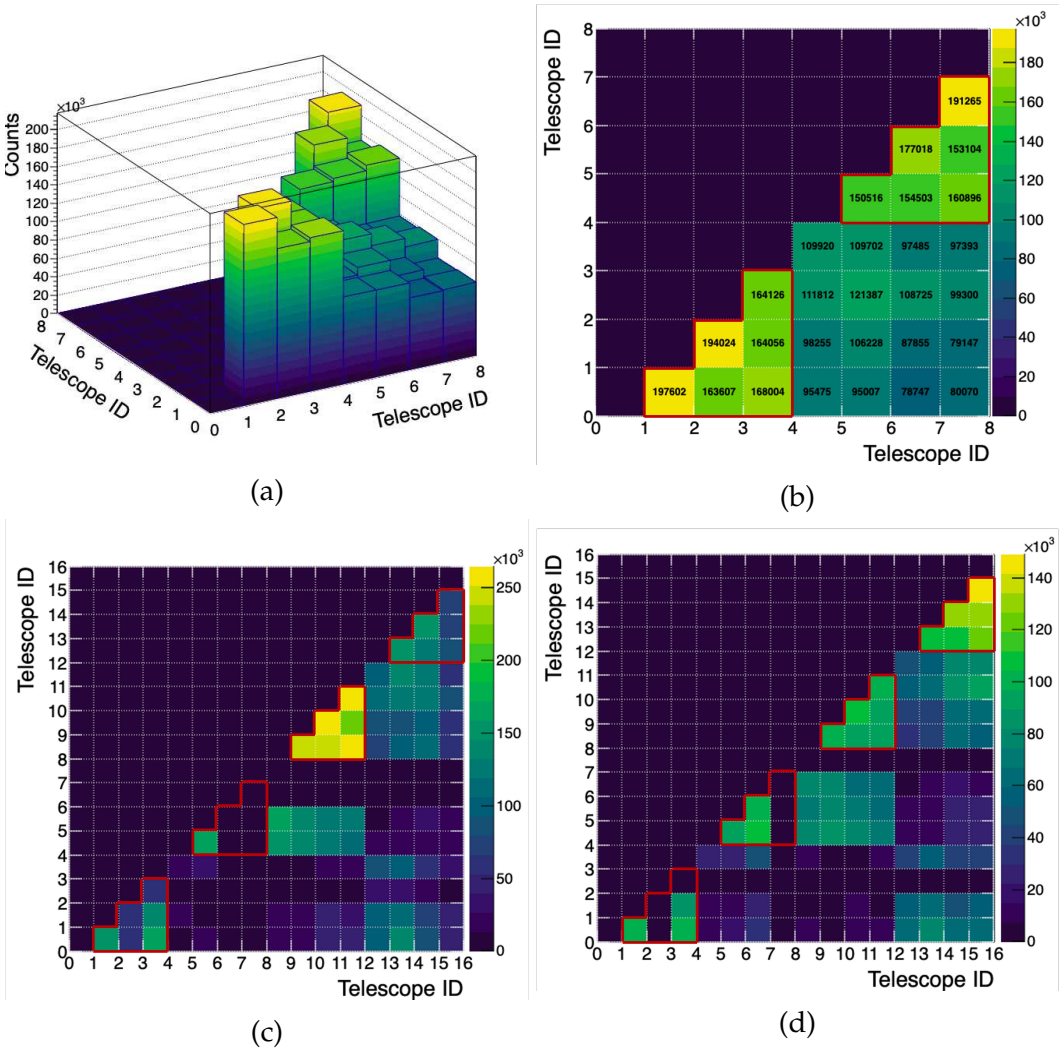


Figure 5.4: (a) Correlation among the eight telescopes used in the in-beam commissioning experiment and its (b) projection over the Telescopes IDs plane. (c) and (d) are the telescope correlations for the latest experiment; the empty columns (or rows) correspond to the telescopes with issues in the acquisition (not possible to determine the position), and they were excluded from the analysis. The telescope correlations in the same clover are enclosed in red. The topology of the setup configuration can be found in Figure 2.14.

## 5.4 Energy Transition Reconstruction

### 5.4.1 $\gamma$-ray Spectrum

As Chapter 4 describes, a $LaBr_3$ scintillator detector was placed outside the chamber to monitor the integrity of the target, but also to track the population of the states of interest in $^{8}$Be and $^{16}$O. This population can be observed indirectly by the depopulation of those states decaying by $\gamma$ ray emission. Figure 5.5 shows the $\gamma$ ray spectrum measured during the irradiation of the LiF target by a proton beam at 441 keV energy. Two photo-peaks (orange lines) can be observed at 6.128 MeV ($^{16}$O: $3^- \rightarrow 0^+$) and 17.62 MeV ($^{8}$Be: $1^+ \rightarrow 0^+$). The $LaBr_3$ detector (3" $\times$ 3") presents limited efficiency for high energy $\gamma$ rays. The probability of escaping of one (or the two) $\gamma$ ray(s) after the annihilation of the $e^+$ from the EPC (External Pair Creation) process in the $LaBr_3$ detector can be seen in the $\gamma$ ray spectrum in the appearance of two escape peaks (blue lines) at the left of the photo-peaks. The $2^+_1$ state in $^{8}$Be is broad ($\Gamma$ = 1.5 MeV). Therefore, the $\gamma$-ray of the $2^+_1 \rightarrow 0^+_1$ transition is not a well-defined peak but rather distributed. The purple region in Figure 5.5 represents the area between the center of this energy distribution and its second escape peak. Finally, a not-very intense photo-peak can be observed at 7.115 MeV ($^{16}$O: $1^- \rightarrow 0^+$) together with the first escape peak. In the case of $^{16}$O, there is no single $\gamma$-ray emission (the double $\gamma$-ray emission can be neglected due to the low probability) in the $0^+_2 \rightarrow 0^+_1$ transition. Still, the observation of the population of the $3^-_1$ state at 6.129 MeV indicates that the $0^+_2$ state at 6.049 MeV was also populated. This information confirmed the population of the electromagnetic transitions presented in Table 1.1) for the 441 keV proton irradiation.

### 5.4.2 Telescopes Energy Correlation

The previous paragraph showed the presence of electromagnetic transitions that will also emit $e^+e^-$ pairs via the IPC process from a LiF target by the proton-induced reactions at 441 keV beam energy (from the $\gamma$ ray spectrum). Correlating the deposited energy in two telescopes in coincidence (in the calorimeters) can give us more information about the $e^+e^-$ pairs. As a first approximation, the expectation of the correlation of such energies is a series of bands for the transitions shown in Table 1.1, excluding the $1^+_1 \rightarrow 2^+_1$ transition in $^{8}$Be because of the

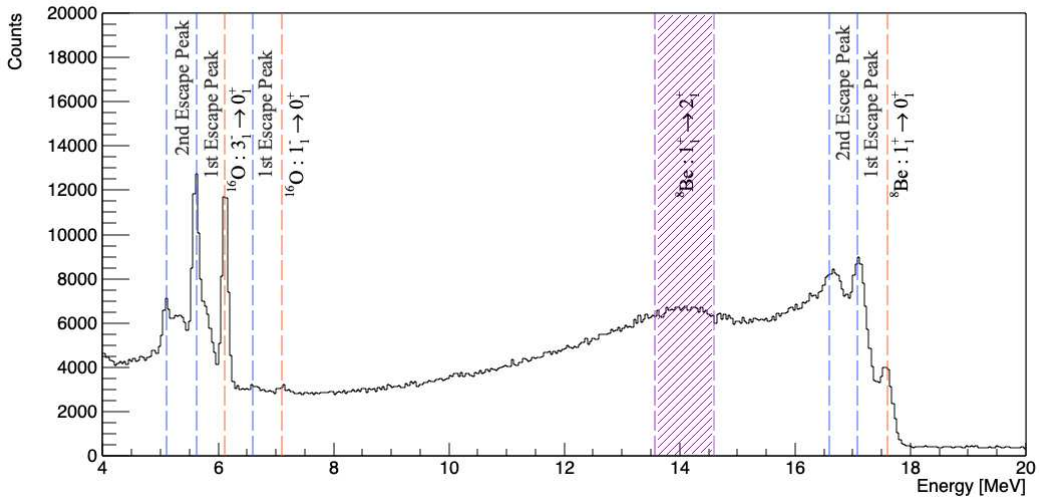


Figure 5.5: $\gamma$ ray spectrum for a $LaBr_3$ detector emitted by a LiF target irradiated by a proton beam at 441 keV energy.

broader $2_1^+$ state. Of course, creating the pair means a 1.022 MeV spent energy before sharing it, but this value is constant and only shifts the structures. When those particles arrive in the calorimeter of a telescope, they lose an energy of ≈1.23 MeV (according to Geant4 simulations) in the bars layers of the telescopes before reaching the calorimeter. Still, this value is almost constant and again only shifts the structures. In other words, the sum of the energy deposited in the calorimeters is constant for an specific electromagnetic transition (this value changes depending on the transition), which means that the deposited energy in the calorimeter of the telescope $i$-th by a $e^+e^-$ ($E_{Tel_i}$) can be expressed in terms of the deposited energy in the calorimeter of the telescopes $j$-th by an $e^+e^-$ ($E_{Tel_j}$):

$$E_{Tel_i} = -E_{Tel_j} + (E_{trans} - 2E_{bars} - 2m_{e^-}) \tag{5.1}$$

where $E_{trans}$ is the energy of the electromagnetic transition, $E_{bars}$ is the energy loss in the bars layer. Equation 5.1 is a line with slope equals -1 and offset equals $(E_{trans} - 2E_{bars})$. Thus, the searched structures are graphically antidiagonal. Returning to the experimental data, Figure 5.6 shows the correlation of the deposited energy in the calorimeter of the telescopes in coincidence for the commissioning experiment for the irradiation at 441 keV. The $0_2^+ \rightarrow 0_1^+$ transition in $^{16}O$ and the $1_1^+ \rightarrow 0_1^+$ transition in $^8Be$ can be observed as the antidiagonal expected form. The width of the antidiagonal is due to the geometry and energy

resolution of the detectors. The $1_1^+ \rightarrow 2_1^+$ transition in $^8$Be does not create a well-defined antidiagonal, but the region of the transition is visible in Figure 5.6. The regions below the antidiagonals are filled by the wall effect discussed in Chapter 2. As discussed in Chapter 3, the hit position in every telescope is determined by the coincidence between the front and back bars. Then, the hit position in one clover is constructed by assembling the four telescopes. A gate in this hit position has been applied to reject the borders to decrease the wall effect, as Figure 5.7 shows (condition applied to every clover). The antidiagonal at the top ($^8$Be : $1_1^+ \rightarrow 0_1^+$) affects all the others below, but that one is not affected by any of them. In addition, cosmic muons also contribute to the background. So, the next level of the analysis will be dedicated to better identifying the $e^+e^-$ pairs.

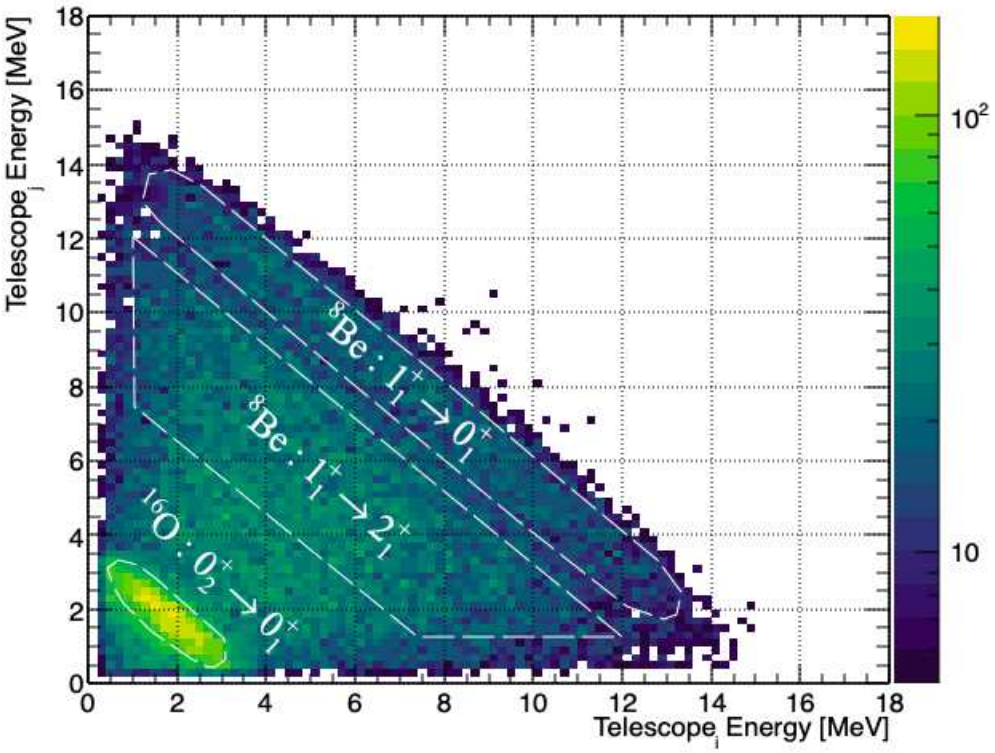


Figure 5.6: Correlation of the energy deposited in the calorimeter of the telescopes in coincidence in the irradiation of the LiF target by a proton beam at 441 MeV proton beam. $e^+e^-$ pairs created in three transitions are observed: $0_2^+ \rightarrow 0_1^+$ transition in $^{16}$O, $1_1^+ \rightarrow 2_1^+$ transition in $^8$Be (not well defined because the $2_1^+$ in $^8$Be is a broad state and because the wall effect. The trapezoid has been drawn as a visual help), and $1_1^+ \rightarrow 0_1^+$ transition in $^8$Be. Data from the commissioning experiment.

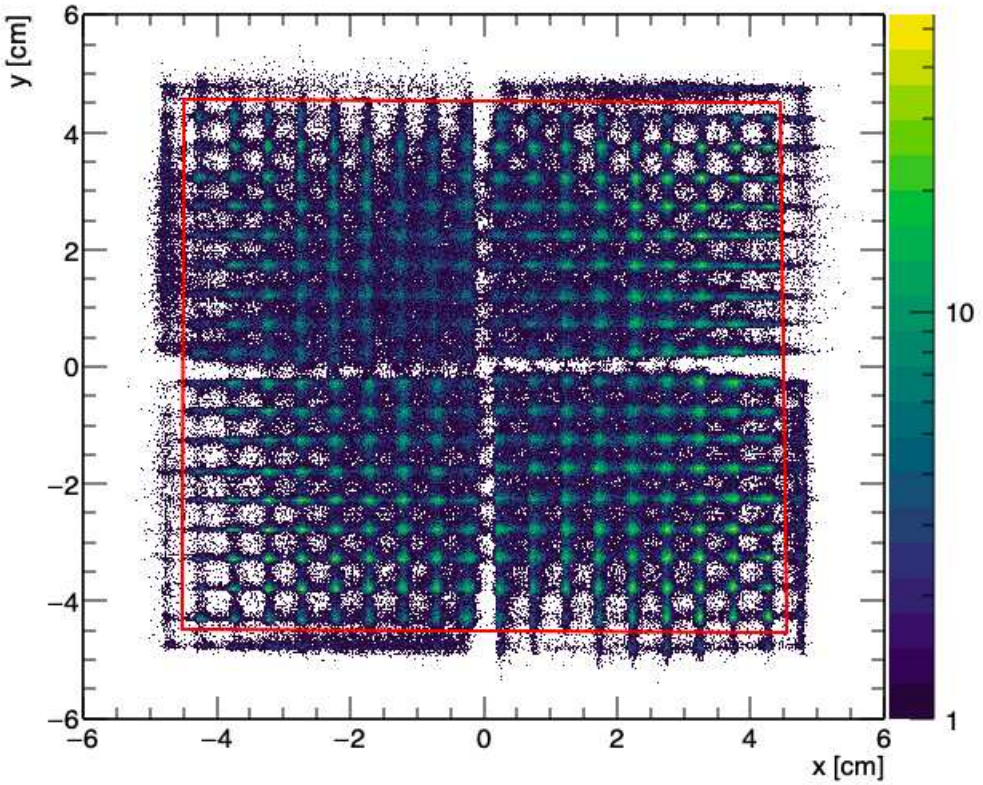


Figure 5.7: Hit position measured by a clover. In red, the gate used to avoid the borders where the particles can escape easily.

### 5.4.3 Energy Assymetry

As reported by A. Krasznahorkay and collaborators [5, 4], $e^+e^-$ pairs with similar kinetic energy are more probable in the IPC process than the ones with high energy asymmetry (defined in Equation 2.4). Therefore, this quantity can be used to get a better performance in the transition energy reconstruction. Figure 5.8 a) shows the Sum of the energy deposited in the calorimeter of two telescopes in coincidence with respect to the energy asymmetry. The central part of the distribution has a higher accumulation of counts (see Figure 5.8 b)), indicating the region where one can consider to be safely achieving a full energy reconstruction. The gate applied in literature is generally placed at $|y| \leq 0.5$, while for the present data set it seems appropriate to extend it to $|y| \leq 0.75$.

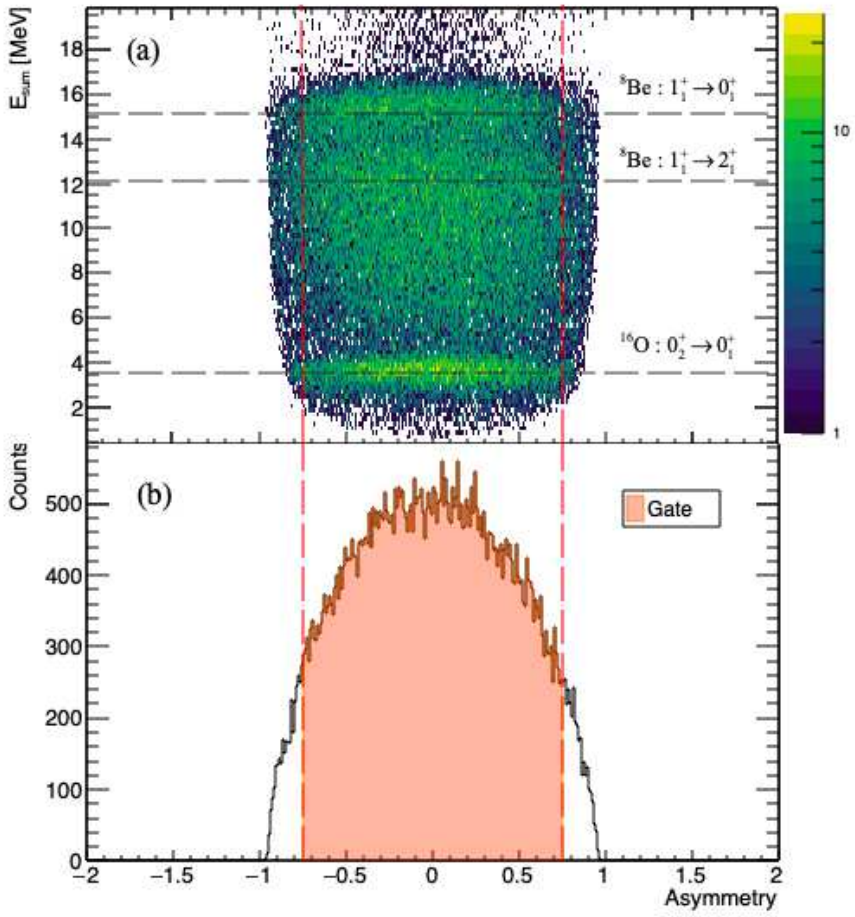


Figure 5.8: (a) Sum of the deposited energy in the calorimeters of the telescopes in coincidence versus the energy asymmetry, (b) energy asymmetry and gate $|y| \leq 0.75$.

### 5.4.4 Energy Offset

An offset factor was applied to the sum energy of the calorimeters to add the loss energy in the bars and the energy of the $e^+e^-$ pair creation. This factor can be calculated directly from the Geant4 simulation and applied to every pair of telescopes separately to get better performance (the energy loss in the bars has a slight dependence on the incidence angle of the $e^+e^-$ in the detector, as Figure 2.21 a) shows). Figure 5.9 shows the process result as a function of all possible combinations for eight telescopes. On the vertical axis is the sum of the deposited energy in the calorimeters plus the offset factor. Meanwhile, on the

horizontal axis is the telescope pair combination Tel_ID, calculated as:

$$Tel\_ID = NB\_TELS \times Telescope\_ID_i + Telescope\_ID_j \tag{5.2}$$

where $NB\_TELS$ is the total number of telescopes and:

$$Telescope\_ID_i < Telescope\_ID_j$$

For example, in the commissioning experiment ($NB\_TELS = 8$ telescopes), the ID number ($Tel\_ID$) for the correlation between telescopes 3 ($Telescope\_ID_i$) and 7 ($Telescope\_ID_i$) is $8 \times 3 + 7 = 31$. This procedure allows us to recover the correct energy values of the electromagnetic transitions shown in Table 1.1 (see the alignment of $E_{sum}$ to the dashed line at 6.05 MeV in Figure 5.9).

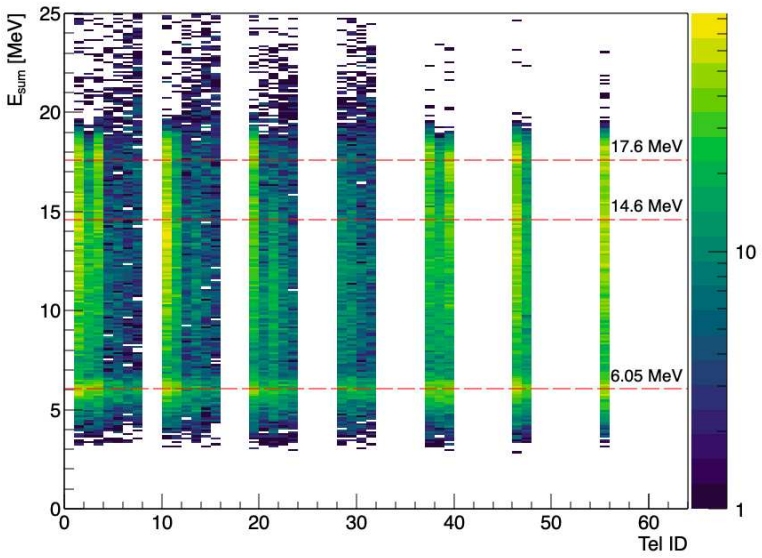


Figure 5.9: Sum of the deposited energy of the calorimeters of the telescopes in coincidence. The identification number (see Equation 5.2) is shown on the X-axis.

### 5.4.5 $\Delta E - E$ Analysis

Figure 5.10 shows the $\Delta E - E$ matrix obtained for a typical case of irradiation at 441 keV. The distribution corresponding to $e^+e^-$ as expected from the Geant4 simulations (Figure 2.22) cannot be identified in the experimental data. This is mostly due to dominating background signals that prevent the use of this

correlation for further data selection. Therefore, the use of an alternative matrix is proposed. This consists of the correlation of the sum of the deposited energy

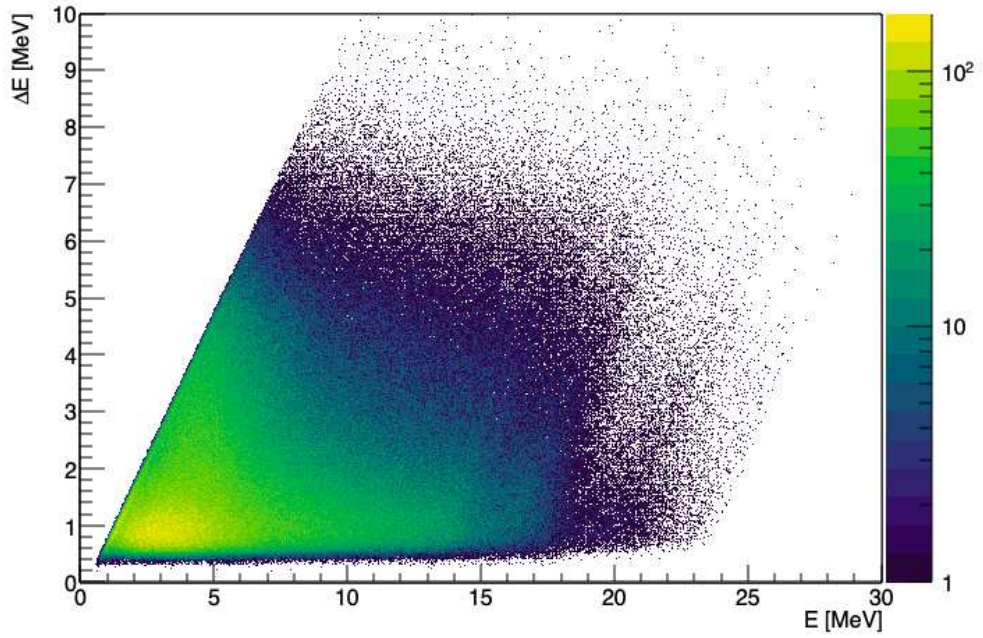


Figure 5.10: $\Delta E - E$ matrix measured by the scintillator telescope detectors.

in the bars layers in the two telescopes in coincidence ($dE_{sum}$) with the sum of the deposited energy in the calorimeters ($E_{pairs}$, including the energy offset) allows us to see the electromagnetic transition as areas with accumulation of counts (see Figure 5.11 and 5.12). These matrices also show us where to set a gate in the $dE_{sum}$ and get the best performance for the transition reconstruction energy. Even for a case with much fewer statistics, the matrix can be built to see the effect of the deposited energy in the bars layers. Table 1.2 shows the main states that decay via the IPC process in the LiF target irradiation at 1.03 MeV. As Figure 5.12 shows, the $dE_{sum} - E_{pair}$ matrix contains the two structures corresponding to the $^{8}$Be transitions. Since the target frame was made of aluminum, a third structure corresponding to the $e^+e^-$ pairs of the $^{27}$Al($p$,$e^+e^-$)$^{28}$Si appears. The $^{16}$O transition was cut on purpose because the cross-section of the IPC increased dramatically with the beam energy (see Figure 4.4 a)). Another helpful tool implemented is the add-back technique (described in Chapter 2). Since the $e^+/e^-$ can go to another calorimeter in the same clover (or bremsstrahlung radiation, or annihilation $\gamma$ rays), the sum of the deposited

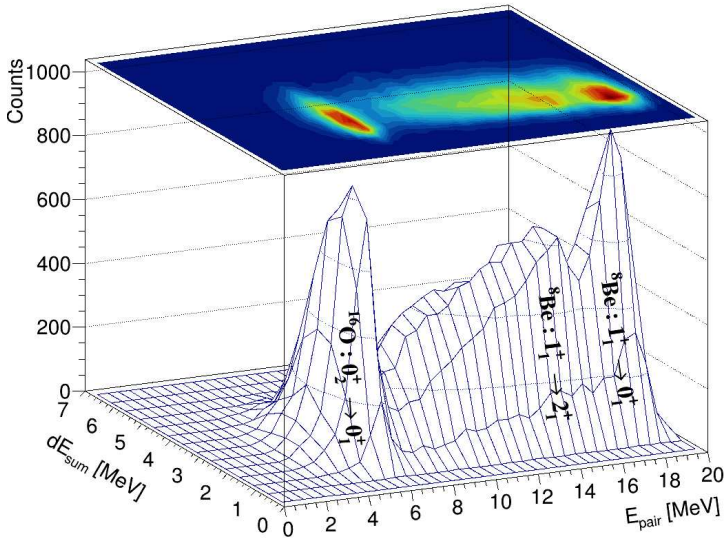


Figure 5.11: $dE_{sum} - E_{pair}$ matrix of the $e^+e^-$ pairs measured during the proton irradiation at 441 keV.

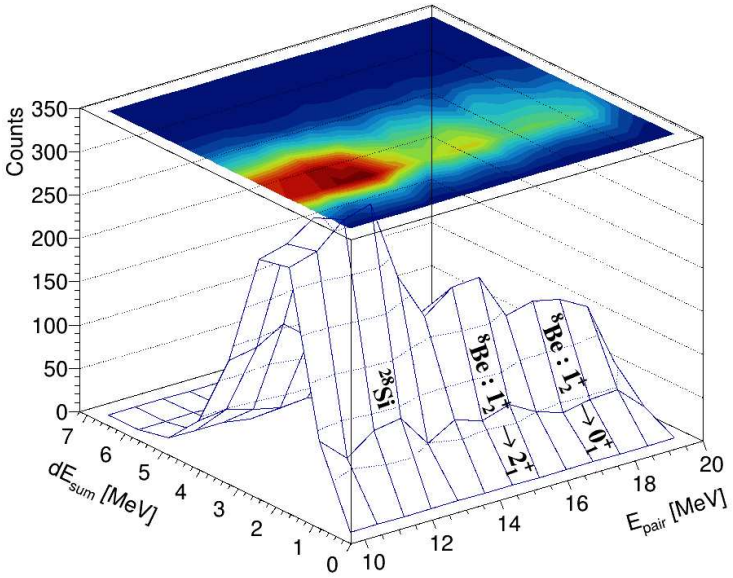


Figure 5.12: $dE_{sum} - E_{pair}$ matrix of the $e^+e^-$ pairs measured during the proton irradiation at 1.05 MeV.

energy in the four telescopes of a clover was performed. In Figure 5.13, the add-back histogram has a better energy resolution than the sum energy of the telescopes. Moreover, the high-energy peak recovers events previously in a lower-energy section. Thus, a time coincidence window of $|\Delta t| \leq 5$ ns, an

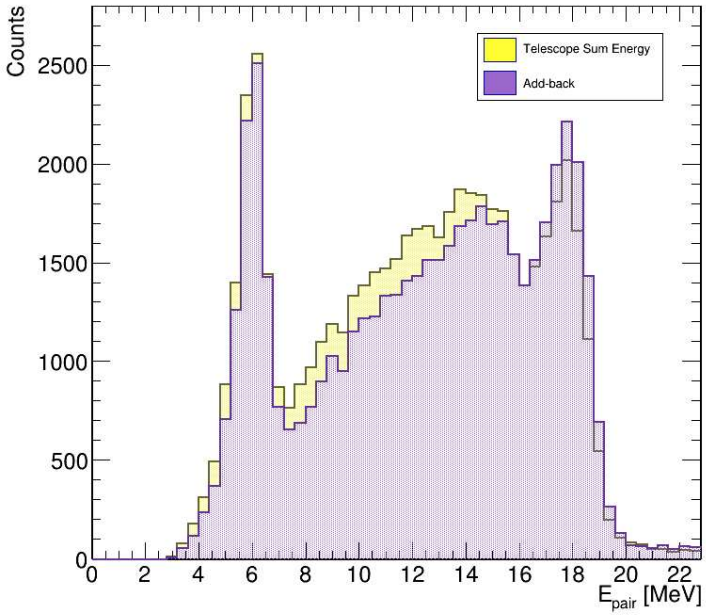


Figure 5.13: Comparison between the sum of the deposited energy in the telescopes in coincidence (yellow) and applying the add-back technique in the clover fired (violet) for the 441 MeV proton beam irradiation.

energy asymmetry of $|y| \leq 0.75$, the add-back technique, and a gate in the $dE_{sum}$ from 1.2 to 2.2 MeV are implemented in the reconstruction transition energy of the two target irradiation energies. In Figures 5.14 a) and b), corresponding to the commissioning and the second experiment of an irradiation energy of 441 keV, respectively, two well-defined peaks (with an average $\sigma$ of 0.42±0.02 and 0.88±0.06, respectively) can be observed for the $0_2^+ \rightarrow 0_1^+$ transition in $^{16}$O (used as a reference and calibration point) and for the $1_1^+ \rightarrow 0_1^+$ transition in $^{8}$Be. The structure between the two peaks corresponds to the $1_1^+ \rightarrow 2_1^+$ in $^{8}$Be. Due to the width of the $2_1^+$ state and the wall effect, this intermediate zone is less clear, as discussed before.

Regarding the irradiation at 1.03 MeV, the high emission of $e^+e^-$ pairs from the $^{16}$O transition and the low probability of pairs from the $^{8}$Be complicated the visualization of those pairs. In Figure 5.15 a) and b), corresponding to the

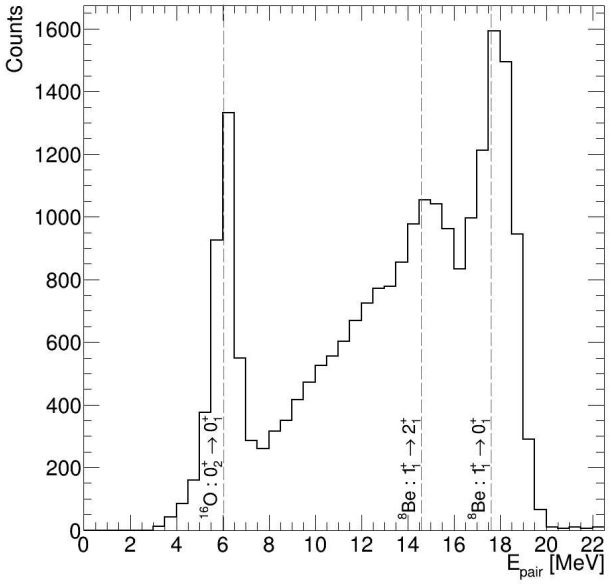


(a)

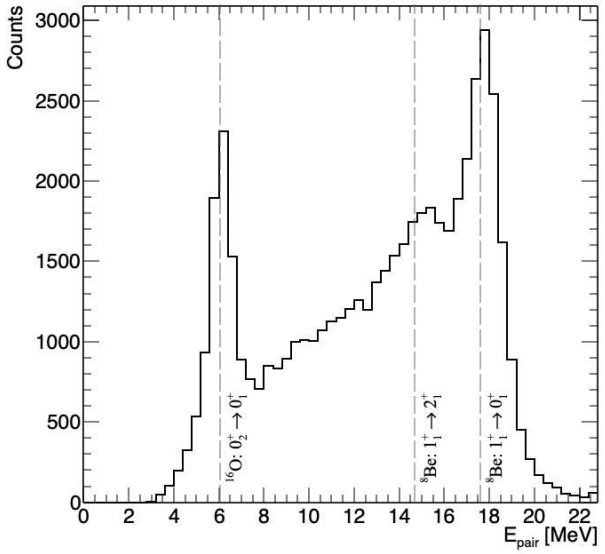


(b)

Figure 5.14: Transition Energy Reconstruction of the proton irradiation at 441 keV gated on $dE_{sum}$ from 1.2 to 2.2 MeV for the a) Commisioining and b) Second experiment. For the first experiment, there was no proton irradiation at 441 keV.

first and second experiment, respectively, the most intense peak is due to the $e^+e^-$ pairs from $^{16}$O, but it is over the vertical axis range. Meanwhile, the ones from $^8$Be are orders of magnitudes smaller (see Figures 4.4). In the sum energy spectrum of Figure 5.15, two structures are distinguishable and correspond to the $1_2^+ \rightarrow 0_1^+$ and the $1_1^+ \rightarrow 0_1^+$ transitions in $^8$Be. Thus, the spectrometer can measure $e^+e^-$ pairs with a small cross-section (fractions of mb).

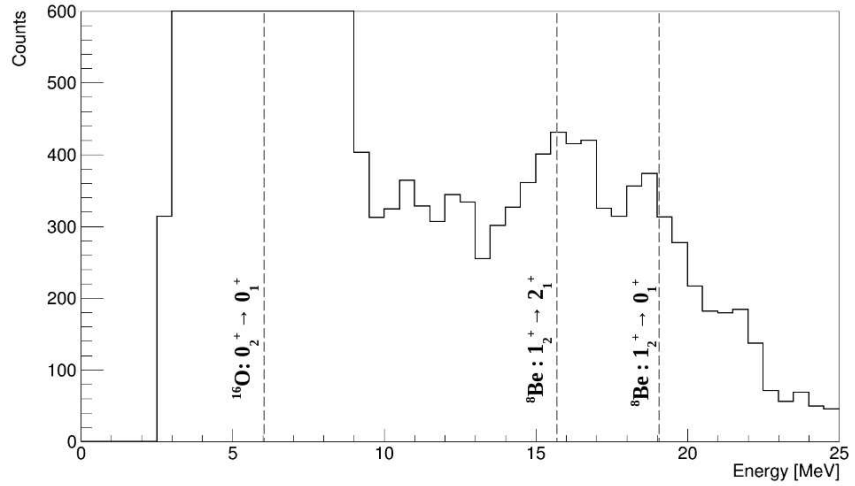


(a)

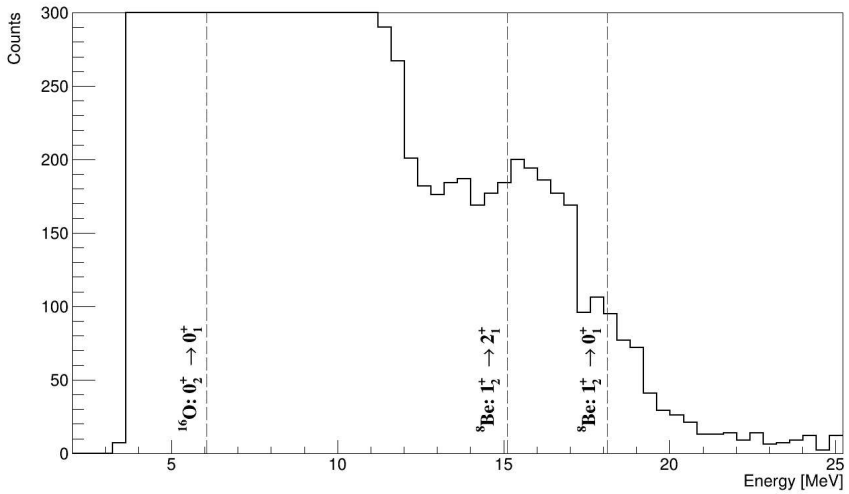


(b)

Figure 5.15: Transition Energy Reconstruction of the proton irradiation at 1.03 MeV gated on $dE_{sum}$ from 1.2 to 2.2 MeV for the a) first experiment and b) second experiment.

## 5.5 $e^+e^-$ Relative Angle Reconstruction

After reconstructing the transition energy, the angle between the $e+$ and $e-$ can be calculated by constructing two vectors from the center of the target to the measured hit position of the telescopes in coincidence. Such reconstruction is carried out event by event. Then, a correlation matrix of the energy of the pair versus the relative angle can be built. First, the correlation is made by non-using the add-back mode, as Figure 5.16 shows for the commissioning experiment. Three diagonal structures appear (see the region delimited by $50 < \text{Angle} < 100$ and $8 < E_{sum} < 20$), and their origin is unclear at this point.

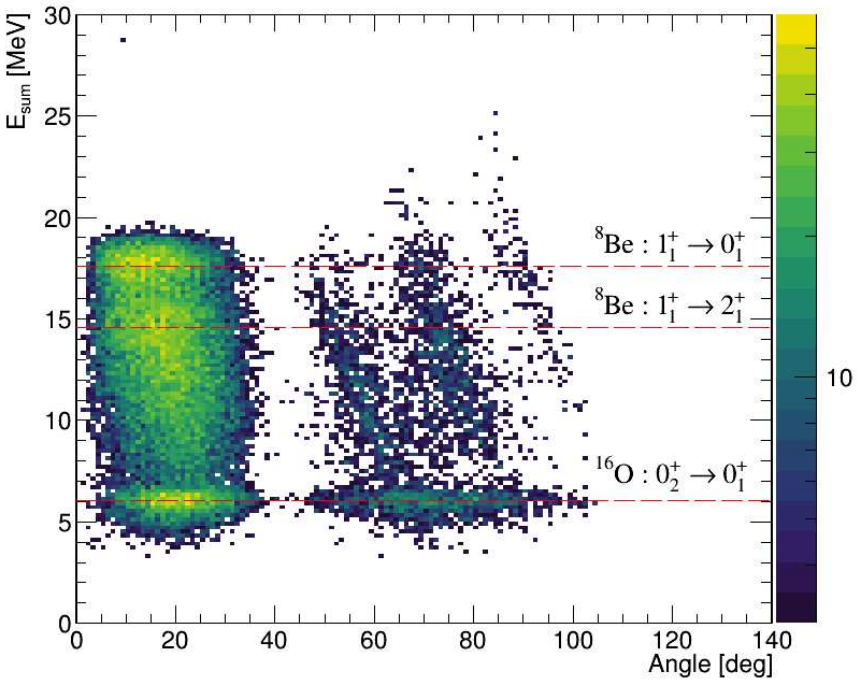


Figure 5.16: Sum of the deposited energy in the telescopes in terms of the relative angle of the $e^+e^-$ pair. Data from the commissioning experiment at 441 keV proton beam irradiation.

When the add-back mode is implemented (see Figure 5.17), those three diagonals become a single one and go to energies higher than 30 MeV. The most reliable explanation concerns the presence of cosmic muons in the events, as the nuclear reaction studied cannot emit ions at that energy. The matrix shows the different electromagnetic transitions for the irradiation at 441 MeV, and the angular distribution of the $e^+e^-$ pair emission can be performed by

gating on the energy of the pair. That distribution depends on the detector array geometry, the energy of the transition that originated the $e^+e^-$, and the type of electromagnetic transition. Thus, a correction by efficiency is needed to obtain the angular correlation distribution of the $e^+e^-$ pair. The correlation between

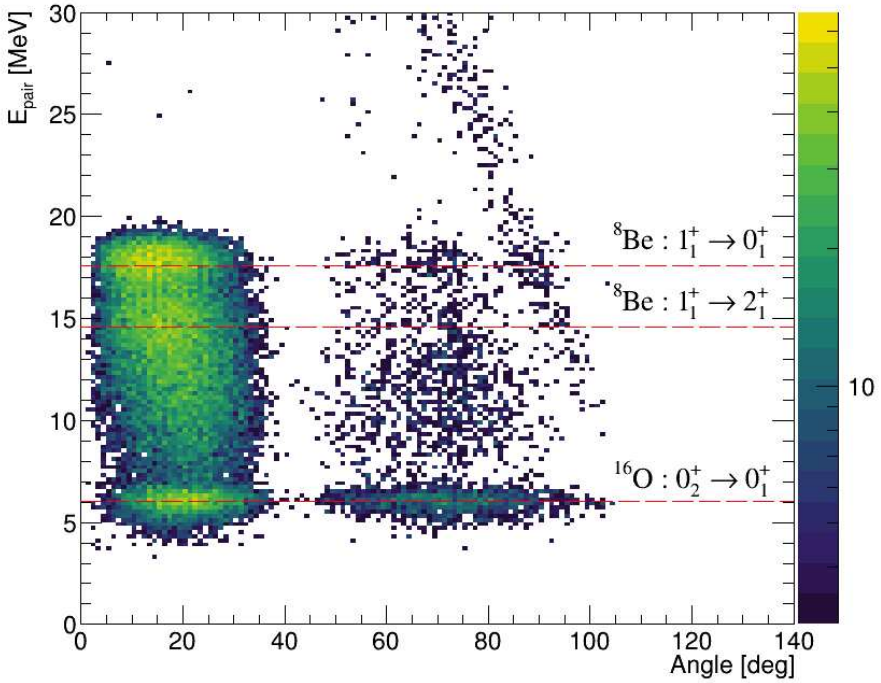


Figure 5.17: Sum of the deposited energy in the clovers (add-back) in terms of the relative angle of the $e^+e^-$ pair. Data from the commissioning experiment at 441 keV proton beam irradiation.

the energy of the $e^+e^-$ pair versus its relative angle is shown for the second experiment in Figure 5.18 at 441 keV proton beam irradiation, for the first and second experiments at 1.03 MeV proton beam irradiation in Figures 5.19 and 5.20, respectively. A larger angular coverage than in the commissioning was obtained for those experiments. Figure 5.19 shows that in the angular regions 30°-50° and 80°-120°, the statistics collected are extremely low, as expected from the efficiency calculations (see Figure 2.30 b)). This fact makes it difficult to determine a full angular distribution. Thus, the data from the first experiment can be used but just in a limited range, as the following paragraph will explain. On the other hand, the second experiment was optimized to get more statistics in the region of interest (80°-160°). The increase in the background is due to the increase of the number of clovers.

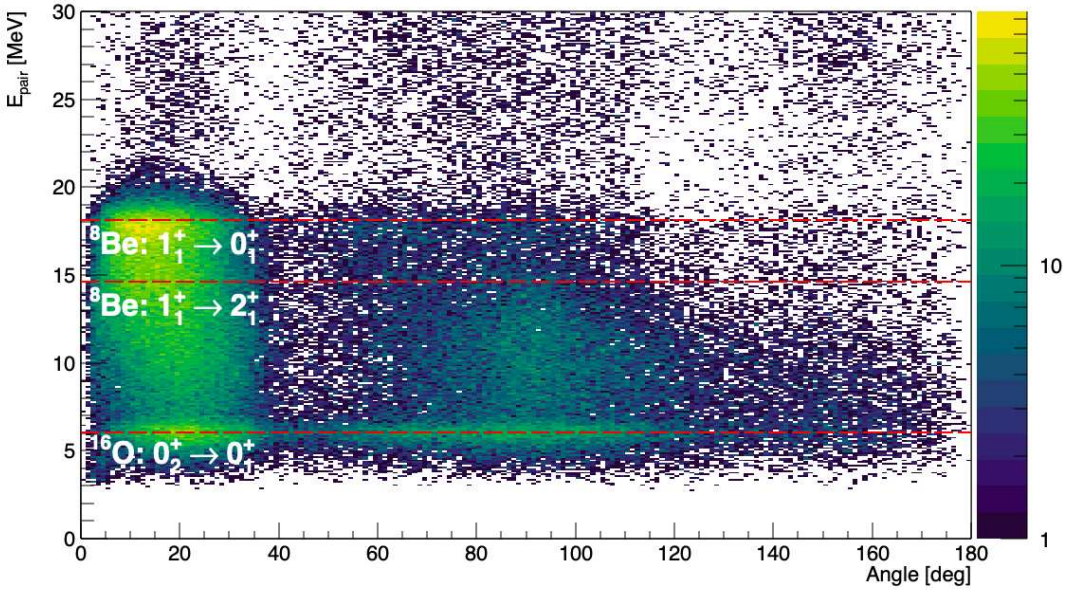


Figure 5.18: Sum of the deposited energy in the clovers (add-back) in terms of the relative angle of the $e^+e^-$ pair. Data from the second experiment at 441 keV proton beam irradiation.

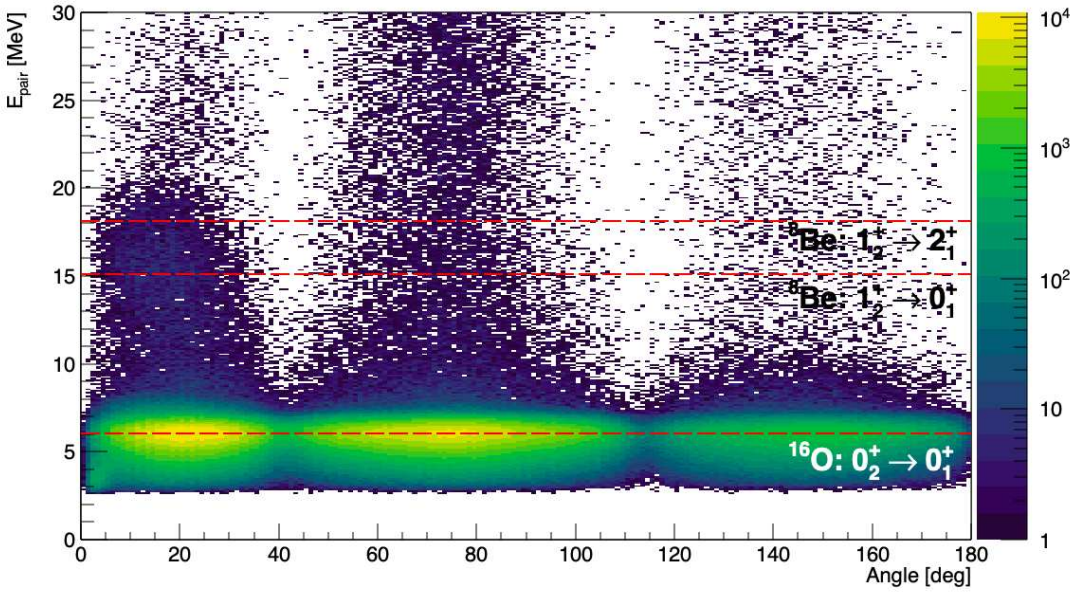


Figure 5.19: Sum of the deposited energy in the clovers (add-back) in terms of the relative angle of the $e^+e^-$ pair. Data from the first experiment at 1030 keV proton beam irradiation.

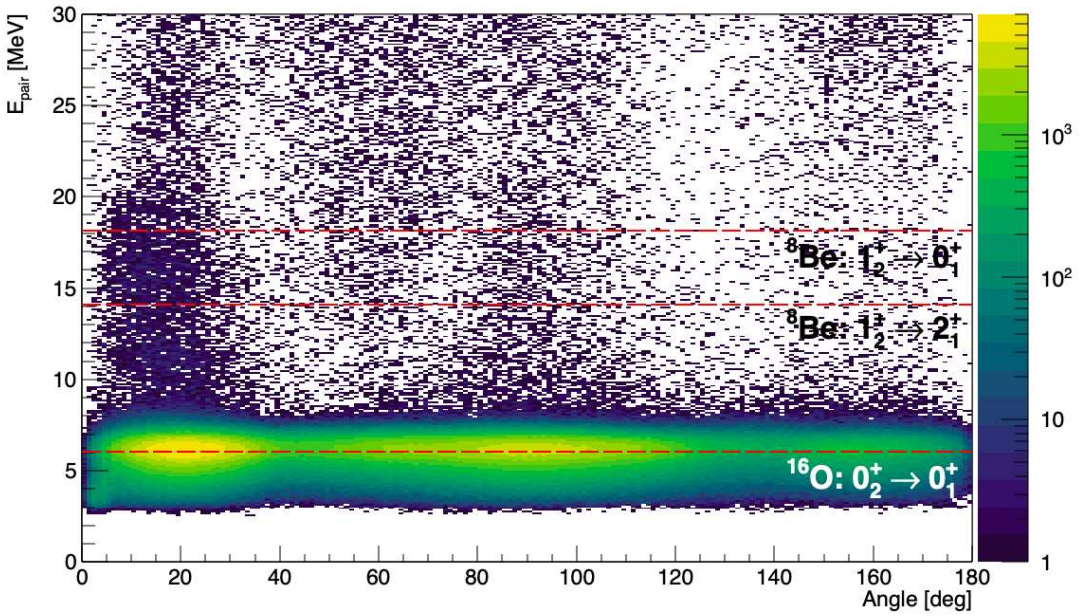


Figure 5.20: Sum of the deposited energy in the clovers (add-back) in terms of the relative angle of the $e^+e^-$ pair. Data from the second experiment at 1030 keV proton beam irradiation.

## 5.6 Efficiency

The $e^+e^-$ angular correlation efficiency has been computed in Chapter 2 from Geant4 simulations for the three detector configurations described above (see Figure 2.14). Those results can be taken as a reference to evaluate the performance of the real setup. The main difference between the experimental data and the simulation is the relative angle emission of the $e^+e^-$ pairs. While in the simulation, the $e^+e^-$ pairs were shot uncorrelated, in the actual experiments, this distribution depends on the multipole order and type of the transition, as the model of Rose explains. So, the methodology implemented is based on constructing a data set that includes uncorrelated events from the data collected in the experiments. This can be achieved by merging two events where only one telescope fired; in other words, merge two events with multiplicity one to create an uncorrelated $e^+e^-$ pair. If the $e^+e^-$ are not correlated, then the structures corresponding to the transition energies (for example, the ones of Figure 5.14) will disappear, and a continuous distribution is expected, as Figure 5.21 shows for the data set acquired at 441 keV proton beam energy.

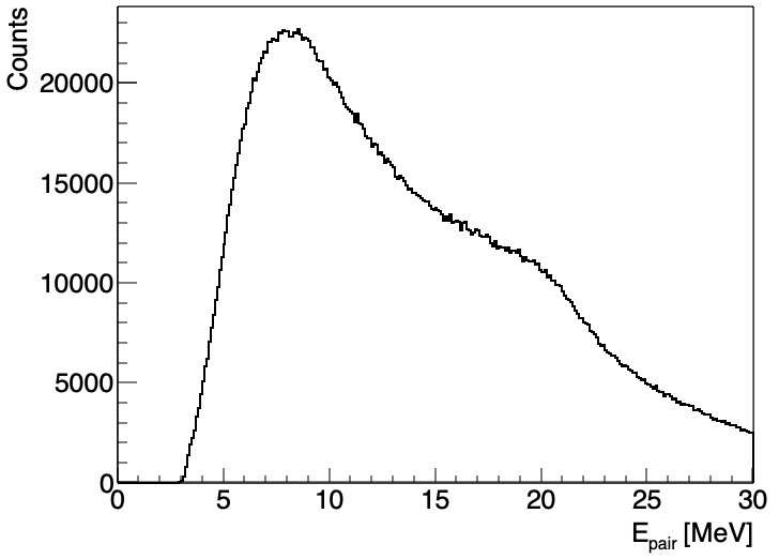


Figure 5.21: Sum of the deposited energy in two telescopes with $e^+e^-$ pairs uncorrelated from the data set acquired at 441 keV beam energy.

Figures 5.22 a) and b) compare the simulated and experimental efficiency for transitions at 6.05 ($^8$Be: $1^+_1 \rightarrow 0^+_1$) and 17.6 MeV $^{16}$O: $0^+_2 \rightarrow 0^+_1$, respectively. A good agreement with the simulation was observed at 6.05 MeV, around a 5% difference on average. In the case of the 17.6 MeV simulation, a certain level of discrepancy appears at small angles (<50°) because the EPC contribution is significant, as de Boer reported [1]. On the other hand, in the 80°-120° region, the discrepancy observed is due to the cosmic muon contribution, as the previous section explained. Regarding the configuration of the two experiments performed with four clovers, shown in Figures 5.23 a) for the first experiment and b) for the second, the efficiency is more complex since the detector array had more extensive angular coverage. Again, the discrepancy at lower angles (<50°) is due to the EPC, and from 80° to 120° is because of the cosmic muon detection. Moreover, the cosmic muon contribution is also expected at high angles (close to 180°) because the muons can pass through two detectors in straight lines. Under those considerations, the most accurate regions are from 50° to 80° and from 120° to 160°, where a good agreement is observed (6% difference on average).

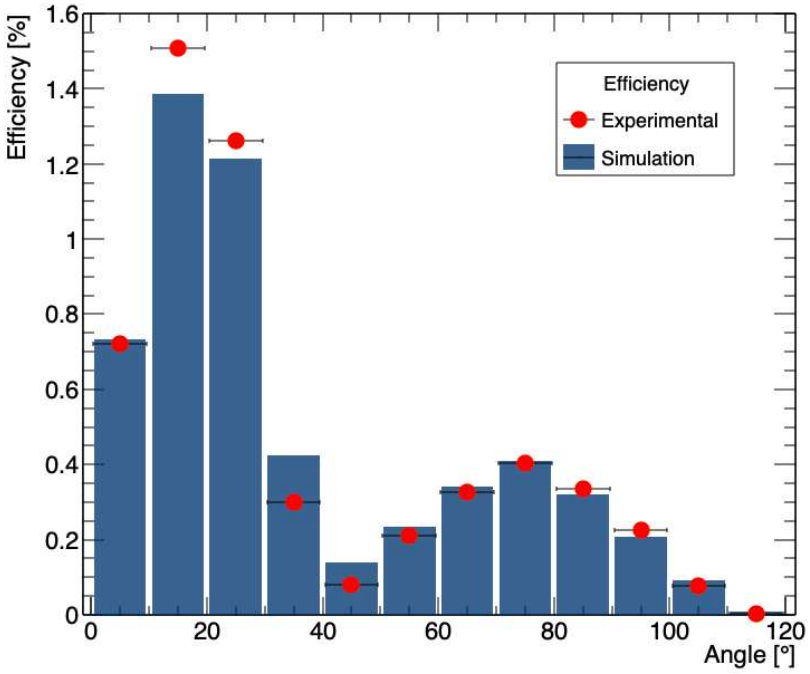


(a)

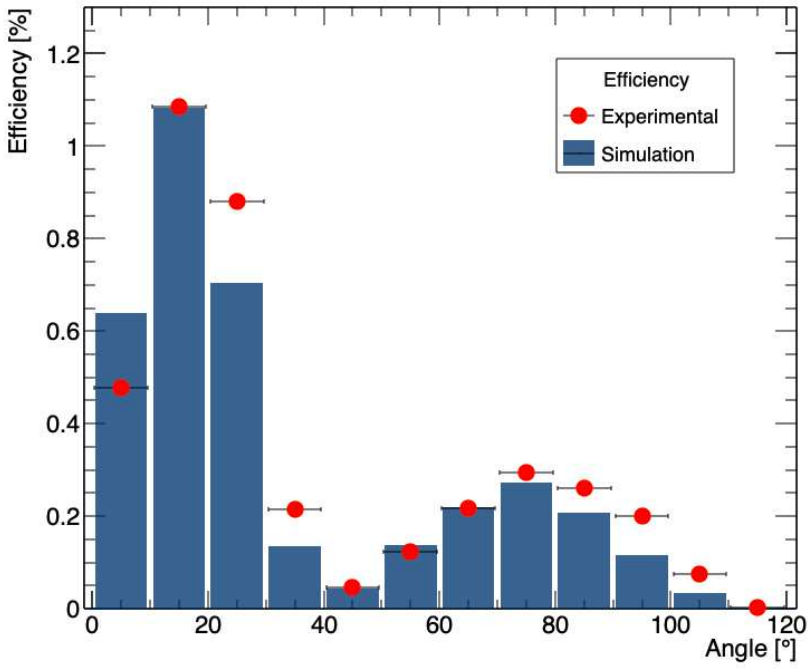


(b)

Figure 5.22: Comparison between the efficiency of the simulation and the commissioning experiment for uncorrelated $e^-e^+$ pairs from transitions at (a) 6 MeV and (b) 17.6 MeV.

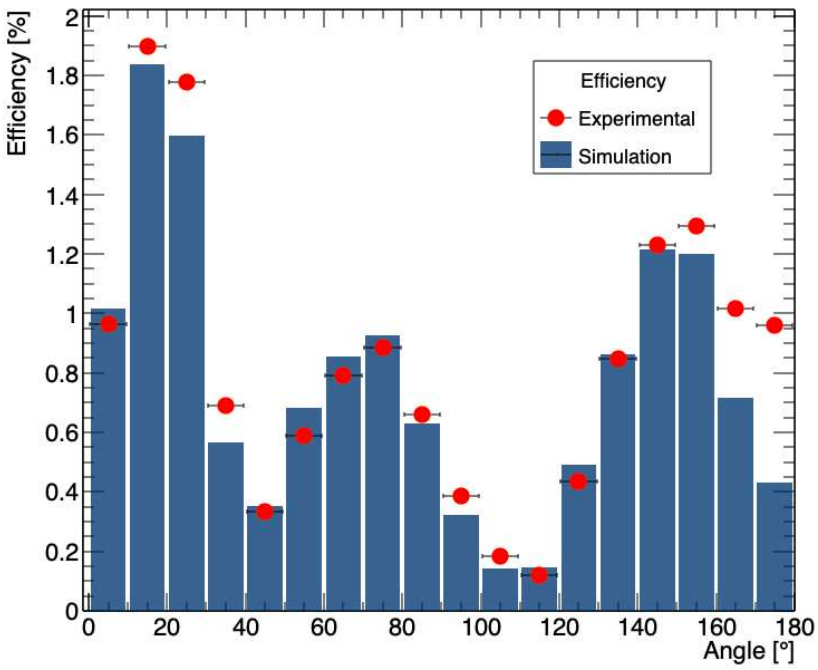


(a)

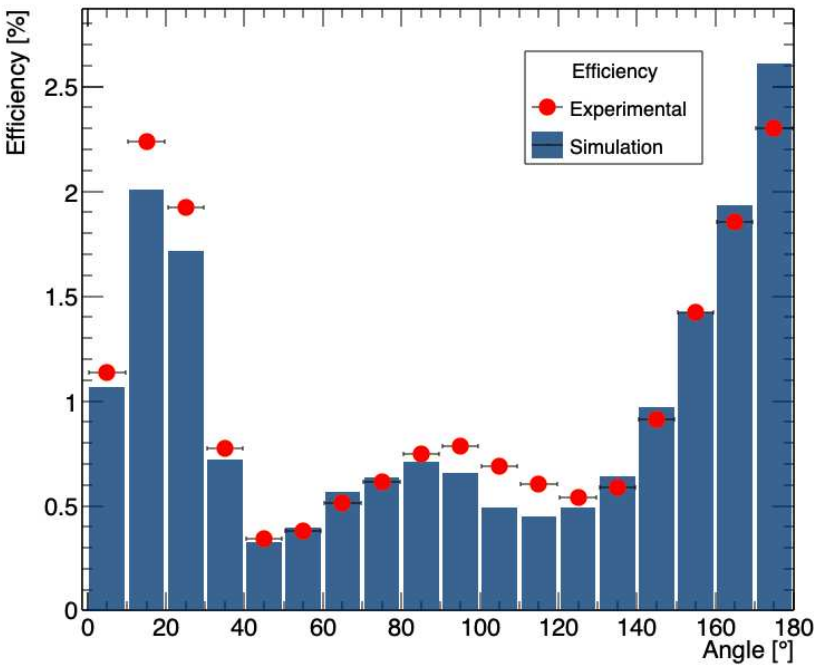


(b)

Figure 5.23: Comparison between the efficiency of the simulation and the a) first and the b) second experiment for uncorrelated $e^-e^+$ pairs from transitions at 6 MeV.

## 5.7 Angular Correlation Distribution $^{16}$O: $0_2^+ \rightarrow 0_1^+$

The experimental detection efficiency described above was used to correct the angular distributions measured for the $e^+e^-$ pairs from the IPC process in $^{16}$O. The Model of Rose can determine the theoretical curve for a $E0$ transition at 6 MeV, and this result can be compared with the angular distributions experimentally obtained by scaling the theoretical one. Since the cross-section of the population of the $0_2^+$ in $^{16}$O is much higher at 1.03 MeV than at 441 keV, this data set was selected for the evaluation. The correction efficiency for the angular distribution was performed from angles larger than 80° to decrease the EPC contamination, which corresponds to the region where the highest discrepancies with the simulation were observed. In the case of the first experiment, the angular correlation distribution was determined with better precision between 120° and 160° (see Figure 5.24), where the discrepancies are in average 5%. The pronounced drop in the efficiency between 80° and 120° affected the determination of the angular distribution, as can be seen in Figure 5.24. Moreover, the high deviation in the efficiency at angles larger than 160° also affected this distribution. In contrast, the second experiment offers a more uniform efficiency in the 80°-150° region. Figure 5.25 shows the angular correlation distribution for the transition studied in $^{16}$O, where a good agreement of the theoretical and experimental distribution was observed, with an average difference of 6%, as expected by the efficiency analysis. The energy spectra shown in an inset in Figures 5.24 and 5.25 correspond to the energy gates of the $e^+e^-$ pairs, where no contamination from other states is appreciable. Hence, the main source of uncertainty is the efficiency correction. These results confirmed that the $e^+e^-$ pair spectrometer can be used to determine the angular correlation distribution for the IPC process in the interval ranging from 80° to 150° for the detector configuration used in the second experiment, with robust discrimination for different transition energies. This angular range is of particular interest because the signal for the anomaly reported by A. Krasznahorkay and collaborators [5, 4] was found there, opening the possibility of using our detector array to investigate this phenomenon in $^8$Be independently.

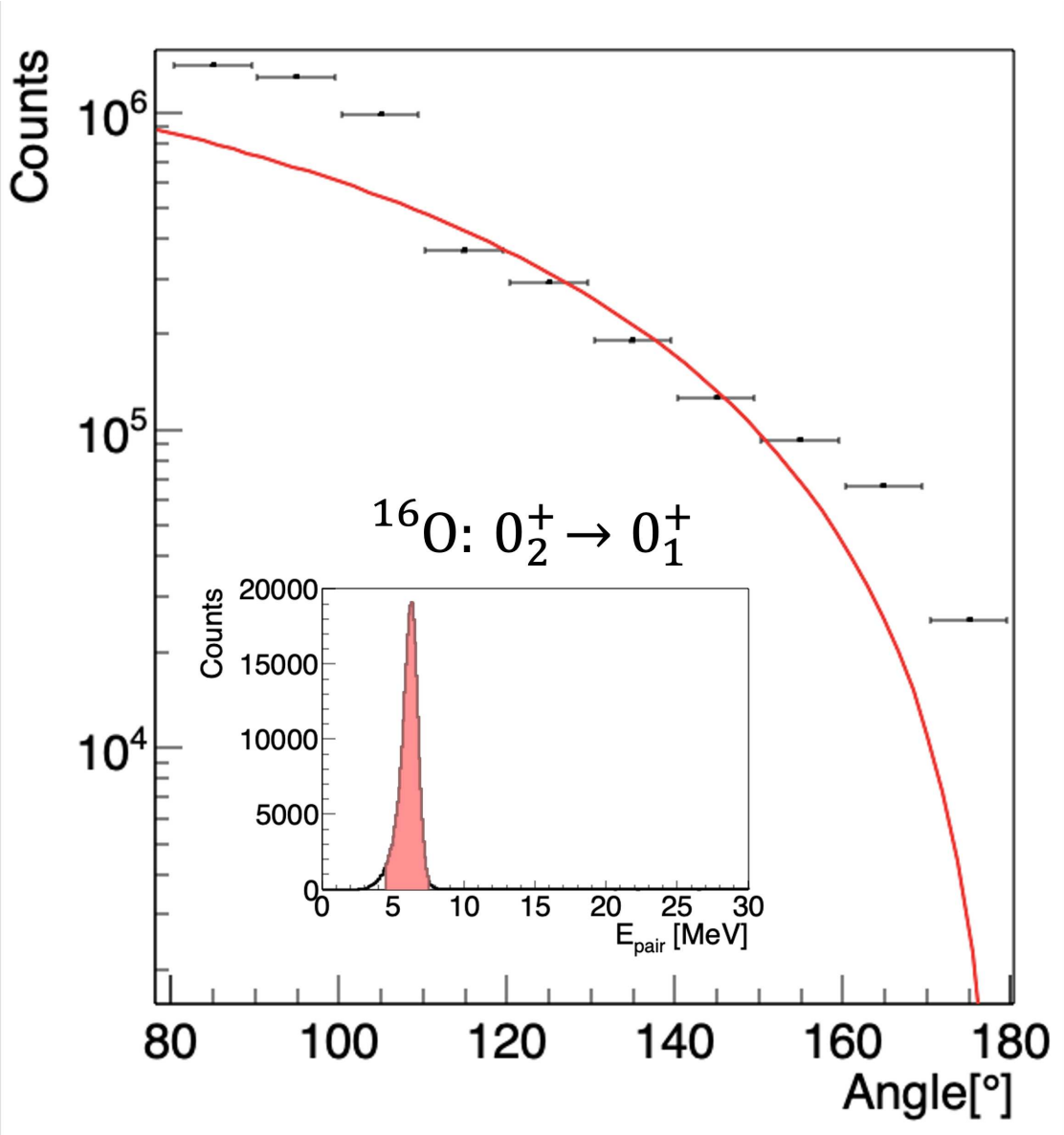


Figure 5.24: Angular correlation distribution of the $e^+e^-$ pair from the $E0$ transition ($0_2^+ \rightarrow 0_1^+$) in $^{16}$O obtained in the first experiment (Conf 2).

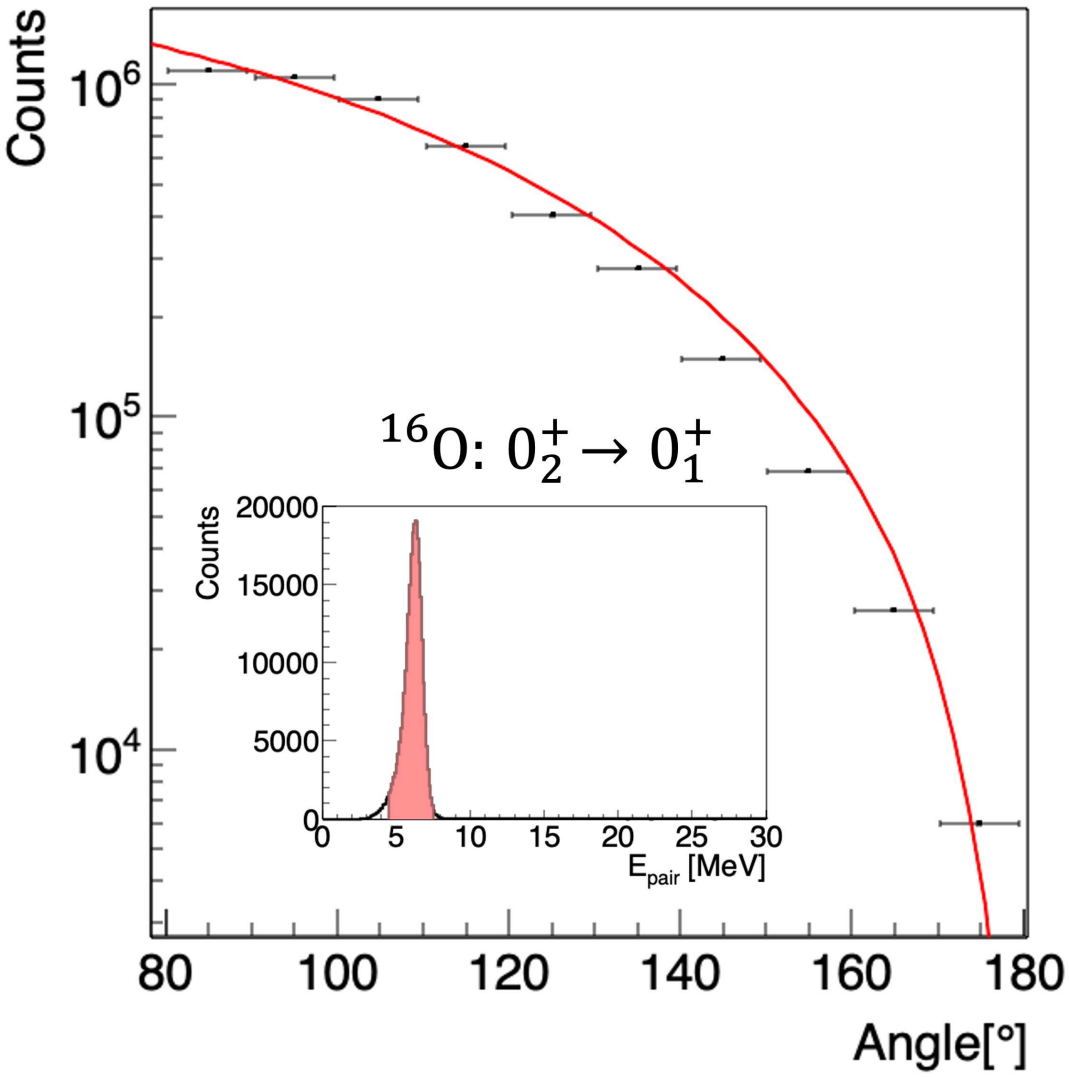


Figure 5.25: Angular correlation distribution of the $e^+e^-$ pair from the $E0$ transition ($0_2^+ \rightarrow 0_1^+$) in $^{16}$O obtained in the second experiment (Conf 3).

# Conclusions and Future Work

A new $e^+e^-$ pair spectrometer has been built, characterized, commissioned, and used for studying Internal Pair Conversion (IPC) processes. The project aimed to study IPC in $^8$Be since anomalies have been reported in the $e^+e^-$ angular correlation distribution for the isovector ($1^+_1 \rightarrow 0^+_1$) [1] and isoscalar ($1^+_2 \rightarrow 0^+_1$) magnetic dipole transitions [5]. These anomalies have been interpreted as the creation and subsequent decay of a new neutral boson with a mass of 16.7±0.35(stat) MeV/c$^2$, named X17 [5].

The $e^+e^-$ pair spectrometer described in this thesis consists of triple stage $\Delta E - \Delta E - E$ telescope detectors clustered in a $2 \times 2$ configuration (called clover). The ΔE part of the detector was designed to measure the position interaction of the $e^+e^-$ pairs accurately, and it consists of a system of 20 bars ($0.2 \times 0.5 \times 5.0$ cm$^3$ each) of scintillator material divided into two layers of 10 bars each, in a relative perpendicular configuration (as Figure 2.4). The $E$ part of the telescope (calorimeter) is a scintillator detector cuboid shape ($10.0 \times 5.0 \times 5.0$ cm$^3$ each) designed to measure leptons with energies in the $1 - 20$ MeV range.

A position reconstruction method was developed to perform tracking with the ΔE stage of the detector. Firstly, no significant cross-talk was observed in neighboring bars when an $\alpha$ source was used (see Figure 3.4). Secondly, an experiment with an $e^-$ source, where the $e^-$ reached the back bars of the telescope, showed similar results in the two bars layers (see Figure 3.5). A resolution of 5×5 mm$^2$ is observed due to the size of the bars fired. In addition, the experiments performed with cosmic muons (shown in Figure 3.1) corroborated that the calorimeter can measure leptons up to ≈ 18.5 MeV. This value was obtained by comparing the experiment with Geant4 simulations.

The detectors have been designed to operate inside the vacuum chamber in order to minimize the multiple scattering of the emitted particles due to dead layers of the setup. The $e^+e^-$ pair spectrometer has proven to be stable

under vacuum conditions since no changes were observed in the performance during the in-beam experiments. This allows us to fully exploit the geometrical angular resolution of 2.5° at a 12.5 cm target-detector distance without significant perturbations.

The experimental campaign focused on the study of the $^{19}$F($p$,$\alpha e^+e^-$)$^{16}$O and $^7$Li($p$,$e^+e^-$)$^8$Be, via the irradiation of LiF targets with a thickness that ranged from 34 to 935 $\mu$g/cm2 (C/Cu backing from 10-60 $\mu$g/cm$^2$) and with proton beam intensities of around 800 nA. Two proton energies 441 keV and 1030 keV were used to populate the $1_1^+$ and $1_2^+$ in $^8$Be, as well as the $0_2^+$ in $^{16}$O. The campaign was divided into three stages: a commissioning and two experiments.

The commissioning experiment was dedicated to testing the performance of the detector array under beam conditions. Two clovers were placed inside the reaction chamber to evaluate the reconstruction of the electromagnetic transitions via the sum of the energy deposited by the $e^+e^-$ pairs from the IPC process. For the irradiation at 441 keV, the $0_2^+ \rightarrow 0_1^+$ in $^{16}$O and the $1_1^+ \rightarrow 0_1^+$ in $^8$Be transition were observed in the sum energy spectrum as two well-defined peak structures (shown in Figure 5.14) with a $\sigma$ of 0.42±0.02 MeV and 0.88±0.06 MeV, respectively. For the irradiation at 1030 keV, the same transition in $^{16}$O was observed, as well as the $1_2^+ \rightarrow 0_1^+$ but much less intense as it is shown in Figure 5.15.

The first and second experiments were dedicated to finding an optimal detector configuration to measure the $e^+e^-$ angular correlation distribution. In those experiments, four clovers were placed inside the chamber with different angular coverage (as Table 4.2 shows). The IPC in $^{16}$O was chosen as the object of study since, in the irradiation at 1030 keV, a high amount of statistics was collected. The efficiency of the setup was used as a reference to evaluate their performances. In the first experiment, the abrupt drop of the efficiency between 80° and 120° and the discrepancies with the simulation at higher angles than 160° pointed out the region to be considered for the efficiency correction (shown in Figure 5.23 a)). The corrected angular distribution in the 120° and 160° (shown in Figure 5.24) was consistent with the model of Rose, with an average discrepancy of 5%. In contrast, the configuration used in the second experiment showed a more uniform efficiency (shown in Figure 5.23 b)) on a broader range from 80° to 150°, showing a good agreement between the corrected angular distribution (shown in Figure 5.25) and the model of Rose, with an average discrepancy of 6%.

In conclusion, the $e^+e^-$ pair spectrometer has demonstrated the capabilities to measure $e^+e^-$ pairs in coincidence from the IPC process in $^8$Be and $^{16}$O, with

robust discrimination of the states of interest via the deposited energy of the pair, and also the capabilities of measuring its position interaction. Thus, this apparatus is an optimal option to continue the study of the deviations reported in the correlation angular distribution found in the IPC in $^{8}$Be, completely independent from other experimental groups.

The plans for the near future involve the analysis of the anomaly in $^{8}$Be, which presents much smaller statistics, in order to get a first angular distribution of the $e^{+}e^{-}$ in the $1_{2}^{+} \rightarrow 0_{1}^{+}$ electromagnetic transition of $^{8}$Be. However, a higher data collection for studying the isovector transition and adding one or two more clovers to arrays are desirable. Later on, a model to characterize the background that includes the contribution of the cosmic muons and the External Pair Creation (EPC) will be needed. The contribution of mixing different types of electromagnetic transitions, such as $E1$ and $M1$, will be estimated.

# References

[1]F.W.N. de Boer et al. "A deviation in internal pair conversion". In: *Physics Letters B* 388.2 (1996), pp. 235–240. ISSN: 0370-2693. DOI: https://doi.org/10.1016/S0370-2693(96)01311-1. URL: https://www.sciencedirect.com/science/article/pii/S0370269396013111.

[2]M. E. Rose. "Internal Pair Formation". In: *Phys. Rev.* 76 (5 Sept. 1949), pp. 678–681. DOI: 10.1103/PhysRev.76.678. URL: https://link.aps.org/doi/10.1103/PhysRev.76.678.

[3]M. E. Rose. "Erratum: Internal Pair Formation". In: *Phys. Rev.* 78 (2 Apr. 1950), pp. 184–184. DOI: 10.1103/PhysRev.78.184. URL: https://link.aps.org/doi/10.1103/PhysRev.78.184.

[4]J. Gulyás et al. "A pair spectrometer for measuring multipolarities of energetic nuclear transitions". In: *Nuclear Instruments and Methods in Physics Research Section A: Accelerators, Spectrometers, Detectors and Associated Equipment* 808 (2016), pp. 21–28. ISSN: 0168-9002. DOI: https://doi.org/10.1016/j.nima.2015.11.009. URL: https://www.sciencedirect.com/science/article/pii/S0168900215013716.

[5]A. J. Krasznahorkay et al. "Observation of Anomalous Internal Pair Creation in $^{8}$Be: A Possible Indication of a Light, Neutral Boson". In: *Phys. Rev. Lett.* 116 (4 Jan. 2016), p. 042501. DOI: 10.1103/PhysRevLett.116.042501. URL: https://link.aps.org/doi/10.1103/PhysRevLett.116.042501.

[6]S Devons, G Goldring, and G R Lindsey. "Emission of Electron-Positron Pairs from Light Nuclei I: Monopole Transition in $^{16}$O". In: *Proceedings of the Physical Society. Section A* 67.2 (Feb. 1954), p. 134. DOI: 10.1088/0370-1298/67/2/305. URL: https://dx.doi.org/10.1088/0370-1298/67/2/305.

[7]Richard Henry Dalitz and Rudolf Ernst Peierls. "On radiative corrections to the angular correlation in internal pair creation". In: *R. Soc. Lond. A* 206.1087 (1951), pp. 521–538. DOI: http://doi.org/10.1098/rspa.1951.0086.

[8]J. R. Oppenheimer and Julian Schwinger. "On the Interaction of Mesotrons and Nuclei". In: *Phys. Rev.* 60 (2 July 1941), pp. 150–152. DOI: 10.1103/PhysRev.60.150. URL: https://link.aps.org/doi/10.1103/PhysRev.60.150.

[9]S Devons and G Goldring. "Emission of Electron-Positron Pairs from Light Nuclei II: $\gamma$-Transitions in $^{8}$Be, $^{10}$B and $^{16}$O". In: *Proceedings of the Physical*

*Society. Section A* 67.5 (May 1954), p. 413. DOI: 10.1088/0370-1298/67/5/302. URL: https://dx.doi.org/10.1088/0370-1298/67/5/302.

[10]W. F. Hornyak et al. "Energy Levels of Light Nuclei. III". In: *Rev. Mod. Phys.* 22 (4 Oct. 1950), pp. 291–372. DOI: 10.1103/RevModPhys.22.291. URL: https://link.aps.org/doi/10.1103/RevModPhys.22.291.

[11]S. Devons and M. G. N. Hine. "The angular distribution of $\gamma$-radiation from light nuclei I. Experimental". In: *R. Soc. Lond. A* 199.1056 (1949), pp. 56–73. DOI: http://doi.org/10.1098/rspa.1949.0125.

[12]S. et al Devons. "Life-time for pair emission by spherically symmetrical excited state of the $O^{16}$ nucleus". In: *Nature* 164.11 (1949), pp. 586–587. DOI: https://doi.org/10.1038/164586b0.

[13]S. Devons and G. R. Lindsey. "$\gamma$-Radiation from the Resonant Capture of Protons by $^{7}$Li Nuclei". In: *Proceedings of the Physical Society. Section A* 63.11 (1950), p. 1202.

[14]Steven Weinberg. "Physical Processes in a Convergent Theory of the Weak and Electromagnetic Interactions". In: *Phys. Rev. Lett.* 27 (24 Dec. 1971), pp. 1688–1691. DOI: 10.1103/PhysRevLett.27.1688. URL: https://link.aps.org/doi/10.1103/PhysRevLett.27.1688.

[15]L. Resnick, M. K. Sundaresan, and P. J. S. Watson. "Is There a Light Scalar Boson?" In: *Phys. Rev. D* 8 (1 July 1973), pp. 172–178. DOI: 10.1103/PhysRevD.8.172. URL: https://link.aps.org/doi/10.1103/PhysRevD.8.172.

[16]A.J. Krasznahorkay et al. "Observation of Anomalous Internal Pair Creation in $^{8}$Be". In: *Acta Phys. Pol. B Proc. Suppl.* Vol. 8. 2015, pp. 597–604.

[17]Tran The Anh et al. "Checking the $^{8}$Be Anomaly with a Two-Arm Electron Positron Pair Spectrometer". In: *Universe* 10.4 (2024). ISSN: 2218-1997. DOI: 10.3390/universe10040168. URL: https://www.mdpi.com/2218-1997/10/4/168.

[18]Jonathan L. Feng et al. "Protophobic Fifth-Force Interpretation of the Observed Anomaly in $^{8}$Be Nuclear Transitions". In: *Phys. Rev. Lett.* 117 (7 Aug. 2016), p. 071803. DOI: 10.1103/PhysRevLett.117.071803. URL: https://link.aps.org/doi/10.1103/PhysRevLett.117.071803.

[19]Maxim Pospelov. "Secluded U(1) below the weak scale". In: *Phys. Rev. D* 80 (9 Nov. 2009), p. 095002. DOI: 10.1103/PhysRevD.80.095002. URL: https://link.aps.org/doi/10.1103/PhysRevD.80.095002.

[20]The MEG II collaboration et al. *Search for the X17 particle in* $^{7}$Li(p, e$^{+}$e$^{-}$)$^{8}$Be *processes with the MEG II detector*. 2024. arXiv: 2411.07994 [nucl-ex]. URL: https://arxiv.org/abs/2411.07994.

[21]Eljen Technology. *EJ-200, EJ-204, EJ-208, EJ-212*. https://eljentechnology.com/products/plastic-scintillators/ej-200-ej-204-ej-208-ej-212[Accessed:June2024]. 2021.

[22]Hamamatsu. *SIPM S13360-6075CS*. https://www.hamamatsu.com/eu/en/product/optical-sensors/mppc/mppc_mppc-array/S13360-6075CS.html[Accessed:June2024]. 2024.

[23]Aim and Thurlby Thandar Instruments (Aim-TTi). *PLH Series*. https://www.aimtti.com/product-category/dc-power-supplies/aim-plhseries[Accessed:June2024]. 2024.

[24]Batronix. *Rigol DP832*. https://www.batronix.com/shop/power-supplies/DP832.html[Accessed:June2024]. 2024.

[25]Eljen Technology. *EJ-510*. https://eljentechnology.com/products/accessories/ej-510[Accessed:June2024]. 2021.

[26]Fondazione Bruno Kessler. *FBK*. https://www.fbk.eu/en/[Accessed:June2024]. 2024.

[27]Fabio Acerbi et al. "Reduced-Channels Position-Sensitive 10×1 SiPM Tile for Scintillator-Bars Readout". In: *IEEE Transactions on Nuclear Science* 71.12 (2024), pp. 2588–2596. DOI: 10.1109/TNS.2024.3489713.

[28]Geant4 Collaboration. *Book For Application Developers*. Geant4, 2023.

[29]R. Bolzonella. "An experimental setup for the detection of $e^{+}e^{-}$ pairs in the decay of $^{8}$Be*". MA thesis. University of Padova, 2021.

[30]CAEN. *V1730 Digitizer*. https://www.caen.it/products/v1730/[Accessed:June2024]. 2024.

[31]CAEN. *CAEN Multi-PArameter Spectroscopy Software (CoMPASS)*. https://www.caen.it/products/compass/[Accessed:June2024]. 2024.

[32]LNL-INFN. *AN2000*. https://www.lnl.infn.it/an2000/ [Accessed: November 2024]. 2024.

[33]D. et al. Zahnow. "The S(E) factor of $^{7}$Li(p, $\gamma$)$^{8}$Be and consequences for S(E) extrapolation in $^{7}$Be(p, $\gamma_0$)$^{8}$B". In: *Zeitschrift für Physik A Hadrons and Nuclei* 351 (1995), pp. 229–236.

[34]Ivano Lombardo et al. "New analysis of $p$ +$^{19}$ F reactions at low energies and the spectroscopy of natural-parity states in $^{20}$Ne". In: *Phys. Rev. C* 100

(4 Oct. 2019), p. 044307. DOI: 10.1103/PhysRevC.100.044307. URL: https://link.aps.org/doi/10.1103/PhysRevC.100.044307.